UNIVERSITY OF COPENHAGEN

MASTER'S THESIS

A panchromatic and structural study of high redshift star forming galaxies

Author:
Simon POCHINDA
(RQC515)

Supervisors:
Georgios MAGDIS
Gabriel BRAMMER

UNIVERSITY OF COPENHAGEN

A thesis submitted in fulfillment of the requirements for the degree of Master of Physics

at the

The Cosmic Dawn Center (DAWN)
Niels Bohr Institute

September 30, 2020

Abstract

For a long time, the existence of a unique type of dusty star forming galaxy (DSFG) has been well-established in extragalactic astrophysics. With a great amount of interstellar dust attenuating stellar light, these DSFGs are often extremely faint, or even invisible, to sophisticated UV-optical facilities such as the Hubble Space Telescope (HST). Typically hosting star formation rates orders of magnitude larger than that of local galaxies, these DSFGs could make up a substantial fraction of the cosmic star formation history (SFH) and energy budget of the Universe. Failing to account for these galaxies could potentially be catastrophic to our models of structure formation, and our understanding of the cosmic SFH. The existence of these DSFGs was first revealed from their strong infrared (IR) signature originating from interstellar dust grains heated by the absorption of stellar light. Using the Atacama Large Millimeter Array (ALMA), astronomers are, for the first time, able to resolve the spatial details of this IR signature and thereby characterize the interplay between galactic dust, gas, and stellar light within these DSFGs.

The aim of this project is to test the robustness of the energy balance principle coupling the absorbed stellar and reemitted IR radiation. This is achieved by utilizing UV-optical data for a sample of DSFGs detected within the recent 69arcmin^2 GOODS-ALMA survey. Characterizing the energy balance within DSFGs would allow astronomers to determine the IR spectral energy distribution (SED) and infer the IR properties of galaxies without using scarce and time-costly IR observations. This investigation is carried out by modeling galaxy SEDs using a set of stellar population synthesis (SPS) models carefully optimized following considerations regarding IR luminosity and energy absorbed. Upon optimizing the SPS models the resulting SED fits were able to reproduce the FIR DSFG SEDs when fitting UV-optical and IR data. When excluding IR constraints, it was found that the modeling was only able to predict the FIR SED of 1.1mm ALMA sources with a compact and co-located HST H-band counterpart, while the remaining SED fits saw a systematic underestimation of the FIR. Thus, we argue that energy balance between absorbed stellar light and reemitted IR radiation is a good assumption when the FIR emission and the UV-optical counterpart is compact and co-located. Following this exercise, the method was generalized and adapted to predict the 1.1mm Universe within the GOODS-ALMA field. This proved reasonably successful as this technique was able to generate a synthetic map in agreement with the observed field, implying that the energy balance principle applies to regular galaxies with robust UV-optical data, but is challenged by extreme DSFGs.

We conclude this study by emphasizing the promising applications of this methodology to large cosmological surveys as future improvements may allow us to determine DSFG properties in bulk, bringing us one step closer to understanding the cosmic SFH and the Universe a whole.

Acknowledgements

I would like to thank my supervisors Georgios Magdis and Gabriel Brammer for helping me and guiding me through this exciting project, and introducing me to new fascinating topics within the field of astrophysics.

Another heartfelt gratitude goes out my friends and my close family, Lisa, mom, and dad who have supported me throughout my studies at the university, and encouraged me to pursue my interests in science from a young age and helped me accomplish my goals.

This work is based on observations taken by the 3D-HST Treasury Program (GO 12177 and 12328) with the NASA/ESA HST, which is operated by the Association of Universities for Research in Astronomy, Inc., under NASA contract NAS5-26555.

Contents

Chapter 1

Introduction

Since its first light operation in 2011 the ground-based Atacama Large Millimeter Array (ALMA) has enabled astronomers to observe the Universe with unprecedented detail at long millimeter and submillimeter infrared wavelengths. With its ability to resolve the cold dust within galaxies billions of light years away, the revolutionary technology of ALMA has helped set the stage for a variety of new discoveries. Among these breakthroughs is the characterization by spatially resolving a new class of extremely dust-obscured galaxy even invisible to the Hubble Space Telescope (HST). The exceptional data produced by ALMA allows astronomers to build extended multiwavelength catalogues with data from observatories spanning the entire electromagnetic spectrum in legacy fields like the Great Observatories Origins Deep Survey (GOODS), and from this data properties of these new elusive dust-obscured galaxies can be derived. The derivation and characterization of dust-obscured galaxies is a crucial piece in the bigger puzzle of determining the evolution of galaxies with cosmic time. Determining the assembly of galaxies in the early Universe remains one of the top scientific objectives of several upcoming observing facilities.

Motivation

The objective of this study is to build a panchromatic cosmological catalogue of dusty star forming galaxies (DSFGs) recently surveyed in deep 1.1mm ALMA imaging, to investigate whether the principle of energy balance can be used to model the far infrared SED by only utilizing UV-optical data. The DSFGs in question are situated within the GOODS–S legacy field which benefits from exquisite multiwavelength photometry covering the electromagnetic spectrum from X-ray to radio wavelengths.

To conduct this predictive test, the photometric redshift code EAZY is used to model spectral energy distributions (SEDs) by fitting sets of stellar population synthesis models to the sample of DSFGs. In contrast to other redshift tools, the advantage of EAZY is its efficiency at providing accurate photometric redshifts and SEDs extremely fast. If successful in our predition of the FIR SED, this method will enable astronomers to deduce galaxy properties without exposure time costly infrared observations. This would be extraordinarily beneficial to upcoming cosmological surveys such as the Euclid space mission, which will provide a wealth of visible to near-infrared data from its 15000deg^2 wide survey, impossible to follow-up with infrared facilities.

1.1 The origin of structure formation

In astronomy the most widely accepted theory for the composition and nature of the Universe is the Standard Model of Cosmology. Also known as the Λ-CDM model, this framework roughly divides the contents of the Universe into respectively dark energy ($\Lambda \sim 70\%$), cold dark matter (CDM$\sim 25\%$), and ordinary matter ($\sim 5\%$).

Backwards extrapolation in time tells us that that the Universe emerged from a singular state in an event commonly known as the Big Bang. In this extremely hot and dense state, the unified fundamental forces separated in a phase-transition-like process and the Universe went through a phase of rapid expansion (inflation), which smoothened out the curvature of space-time making it overwhelmingly flat. As a consequence of inflation, microscopic volumes of quantum fluctuations were blown up to macroscopic scales creating the density fluctuations that would provide the basis for the galaxy and large-scale cluster structure formation. Gradually, the Universe cooled and the energy density decreased to levels replicable by modern-day particle accelerators, which now sets the limits of our probes of the early Universe. The following millions of years, the Universe was relatively uneventful as photons decoupled and gravity, slowly but steadily, accumulated matter in the halos of the dark matter overdensities. Eventually, the collapsing overdensities reached the threshold Jeans mass igniting what became the very first stars, which would reionize the neutral intergalactic medium. The angular momentum of the collapsing overdensities would eventually form stars and galaxies, and many efforts in today's astronomy go into determining the assembly of galaxies over cosmic time, which is among the scientific goals of new facilities like the James Webb Space Telescope (Schneider 2015 [1]).

In this first chapter galaxies are discussed with respect to their mode of star formation, and the basics of star formation and stellar populations are discussed. Additionally, the detection of high redshift galaxies is discussed, and a new type of dusty star forming galaxy is reviewed.

1.2 The two types of star formation: Quiescent and star forming galaxies

There are numerous ways to categorize and describe galaxies. A standard classification scheme is the morphology-based Hubble tuning fork diagram, Figure 1.1a. But galaxies can also be classified by their inherent star formation rate (SFR). Noeske et al. 2007 [2] developed the methodology for assessing the SFR of galaxies relative to a main sequence of star formation, Figure 1.1b. In our local Universe at $z \sim 0$ the galaxy population seems to be dominated by rather low SFRs compared to high redshift galaxies with similar masses but much higher SFRs on the main sequence.

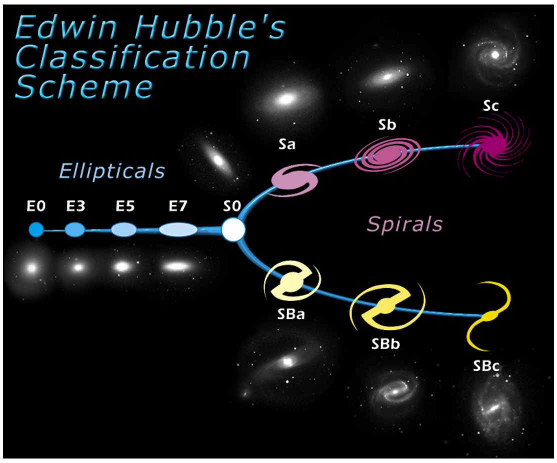

(A)

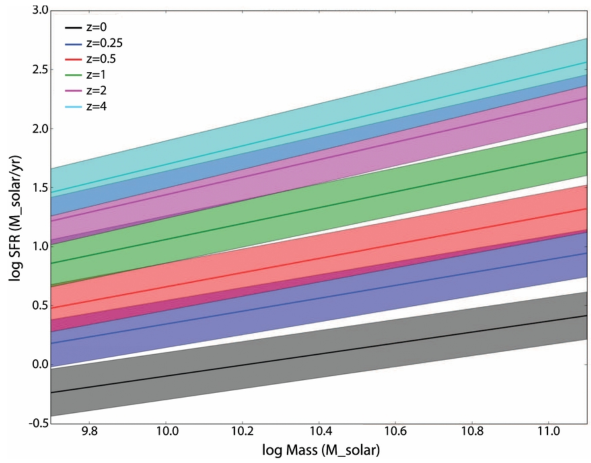

(B)

FIGURE 1.1: 1.1a) The Hubble tuning fork diagram. Credit: NASA & ESA. 1.1b) The galactic main sequence (Speagle et al. 2014 [3])

This puzzle as to why the local Universe is overwhelmingly dead in terms of star formation is yet another much debated mystery of the cosmic star formation history of the Universe central to extragalactic astrophysics. Thus the SFR is often a much desired parameter to try to characterize and determine in astrophysics. Typically, the SFR can be determined from the infrared dust emission, which is regulated by the emission from stars, making the SFR very sensitive to the properties of the underlying stellar population such as mass and age etc.

1.2.1 Stellar populations and star formation rates

The age of the stellar population can vary much in-between galaxy types. For instance, local quiescent ellliptical galaxies have notoriously old stellar populations while high-z DSFGs contain young newly formed stars. These stars are formed during the collapse of dense giant molecular clouds in the interstellar medium. As the cloud starts to contract, the gravitational force exceeds the internal cloud pressure causing subregions to collapse in local filaments in a so-called fragmentation process. For the cloud to collapse a general flow of baryons is required in the interstellar medium, which depends on the gas accretion from the intergalactic medium. A galaxy is so to speak in a gradually shifting inflow-outflow equilibrium driven by feedback processes which regulate SFR, gas fraction, and metallicity etc. (Davé, Finlator, and Oppenheimer 2012[4]). Early studies of high-z DSFGs, Greve et al. 2005[5], found a lower limit on the typical depletion timescale $\tau_{depl} = M(\mathrm{H}_2)/\mathrm{SFR} >\sim$ 40Myr by using molecular CO line emission. This was done using the rotational CO line emission which can trace the warm and dense molecular gas ($J \geq 2$) and the cool and diffuse gas in quiescent regions ($J < 2$). Thus CO line emission can be directly related to the molecular gas mass e.g. $M(\mathrm{H}_2) = X_{\mathrm{CO}} L'_{\mathrm{CO}(1-0)'}$ where X_{CO} is a conversion factor and $L'_{\mathrm{CO}(1-0)'}$ is the luminosity of the CO(1-0) line. This derived short depletion timescale at high-z tells us the story of a highly active Universe where dark matter overdensities were less evolved and the Universe as a whole was less equilibrated. Studies of low-z depletion timescales have shown depletion timescales 2.5 times higher than that of the rapidly star forming early Universe (Scoville et al. 2016[6]).

The star formation rate used to determine parameters such as depletion timescales can likewise be determined from data. A common method assumes an approximate linear relationship with the observed UV radiation corrected for dust attenuation.

$$SFR_{FUV} = \kappa_{FUV} L_{FUV} \tag{1.1}$$

Where L_{FUV} is the far UV luminosity and the constant of proportionality, κ_{FUV}, is a conversion factor. The total SFR is also often determined from the SFR_{FUV} inferred from uncorrected UV emission, in addition to the SFR_{IR} inferred from the infrared emission, which is sometimes more representative of the total SFR in galaxies with significant dust attenuation and uncertainties regarding the underlying dust model.

$$SFR_{tot} = \kappa_{FUV} L_{FUV} + \kappa_{IR} L_{IR} \tag{1.2}$$

Thus the SFR is quite dependent on a correct prediction of the underlying UV emitting stellar population. For a given galaxy the stellar population can be described by the initial mass function (IMF). The IMF describes the number distribution of stars with mass. Among popular IMFs is the Salpeter model (Salpeter 1955[7])

$$\phi(m) \propto m^{-\alpha} \tag{1.3}$$

which predicts a power law ($\alpha \sim 2.35$) distribution. Under the Salpeter model the prediction of massive stars is somewhat reliable, while the simple power law tends to overestimate the population of low mass stars, causing an overestimation of the mass to light ratio. Other truncated models have been proposed, e.g. the multi-part power-law Kroupa model (Kroupa 2001 [8])

$$\phi(m) \propto m^{-\alpha} \begin{cases} \alpha = 0.3 \pm 0.7, & 0.01 < m/M_\odot < 0.08 \\ \alpha = 1.3 \pm 0.5, & 0.08 < m/M_\odot < 0.5 \\ \alpha = 2.3 \pm 0.3, & 0.5 < m/M_\odot < 1.0 \\ \alpha = 2.3 \pm 0.7, & 0.5 < m/M_\odot < 1.0 \end{cases} \tag{1.4}$$

This truncation deals with the overestimation of low mass stars $m < 0.5M_\odot$, e.g. red dwarfs, and the lightest stars such as brown dwarfs $m < 0.08M_\odot$ that do not ignite, whereas the IMF is otherwise almost identical to the Salpeter IMF.

1.2.2 Star formation history and constraints

However, defining the IMF for the stellar population is not always straightforward as star forming galaxies with young stellar populations can outshine the old population. The dominance of the UV brighter young stars creates a bias towards younger massive stars in estimations of the galactic stellar mass, neglecting the old population which may contribute significantly to the stellar mass (Papovich, Dickinson, and Ferguson 2001 [9]). The significance of the old stellar populations is e.g. large for older elliptical galaxies, which tend to have less dust. To avoid such problems it may be necessary to constrain the star formation history (SFH) more accurately to make unbiased and higher quality predictions about the IMF. However, often many SFHs are possible for any individual galaxy, and the SFH does not necessarily have to be smooth, if the galaxy has seen e.g. starbursts due to past galactic mergers throughout cosmic time. Therefore constraining the number of SFHs, especially for high redshift subjects significantly above the main sequence, remains one of the biggest challenges in astrophysics. Attempts to constrain SFHs of DSFGs through cosmological simulations, have similarly hinted towards a lognormal SFH which should be calibrated to the mass of the dark galactic halo of the individual galaxy (Davé, Finlator, and Oppenheimer 2012 [10]). Determining the mass of the dark galactic halo of a high-z DSFG has been attempted for galaxies in so-called protocluster configurations. This can be done by measuring the correlation length in the protocluster to then compare it with correlation length predictions from cosmological simulations to infer the halo mass. Apart from constraining the SFH, the derived mass provides an estimate at which scales DSFGs and starbursts can be found (Casey, Narayanan, and Cooray 2014 [11]).

However, on a cosmic scale these stochasticities tend to statistically smoothen in the global SFH as illustrated on Figure 1.2.

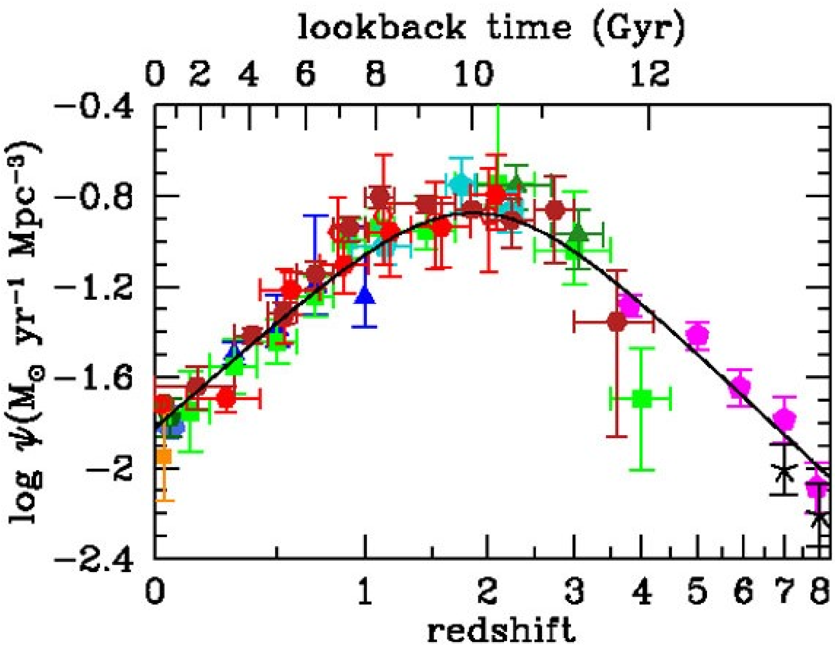

FIGURE 1.2: Lilly-Madau cosmic SFH, star formation rate density (SFRD) versus look-back time (Madau and Dickinson 2014 [12])

Typically this cosmic SFH can be approximated by a simple delayed τ-model, SFR $\sim t \exp\left(-t/\tau\right)$, which peaks around $z \sim 2$ and allows for linear star formation at low-z and an exponential decay at high-z. More detailed studies of the cosmic SFH by Behroozi, Wechsler, and Conroy 2013 [13] and Madau and Dickinson 2014 [12] have found double power laws or lognormal fits to represent the data even better.

1.3 Detection of high redshift galaxies

Finding star forming and starbursting galaxies can be a difficult task, and in general discovering new galaxies, particularly at high redshift, can be done in countless ways. Oftentimes high redshift galaxies are subjected to a distinct absorption of energetic photons from their young stellar populations due to the large ionization cross-section of photons with wavelengths below the lyman limit, $\lambda < 912$Å ($> 13.6eV$ lyman continuum photons, LyC). The vast majority of these photons photoionize the neutral hydrogen in the intergalactic or the interstellar medium. However, absorption does not require photoionizing energies, as this absorption feature also extends to longer wavelengths as well. Namely, the $10.2eV$ Lyα (wavelength $\lambda = 1216$Å), which corresponds to the excitation energy from the neutral hydrogen ground state to its first excited state.

For high redshift objects, we would therefore expect a break at 912Å. However, we still see a Lyα forest for $\lambda < 1216$Å. This is a feature consisting of continuum emission with many superimposed absorption lines, which are due to small fragments of neutral hydrogen filaments within the reionized intergalaxtic medium (IGM) between us, the observers, and the emitting object. At even higher redshifts the IGM has not yet been entirely reionized and is therefore overwhelmingly neutral. In this case the break shifts to 1216Å with no Lyα forest emitters, but just a Gunn-Peterson trough for $\lambda < 1216$Å.

This break can be utilized to detect high redshift galaxies by doing observations with a set of non-overlapping filters. While the rest frame signal from a high redshift subject will be visible in the filters with $\lambda > 1216$Å, the galaxy will be invisible and dropout in filters with $\lambda < 1216$Å as seen on Figure 1.3. Since the discovery of the Lyman-break method in the 90s (Steidel and Hamilton 1992 [14]) this technique has found numerous high redshift galaxies. However, due to the selection criteria that galaxies have to dropout at wavelengths below the 1216Å break and provide a signal above the break, a weakness of the LBG method is its bias towards unobscured star-forming galaxies. Thus to characterize the galaxy population at a particular redshift, one has to employ several different selection methods, due to the inherent bias of individual tests (Schneider 2015 [1]).

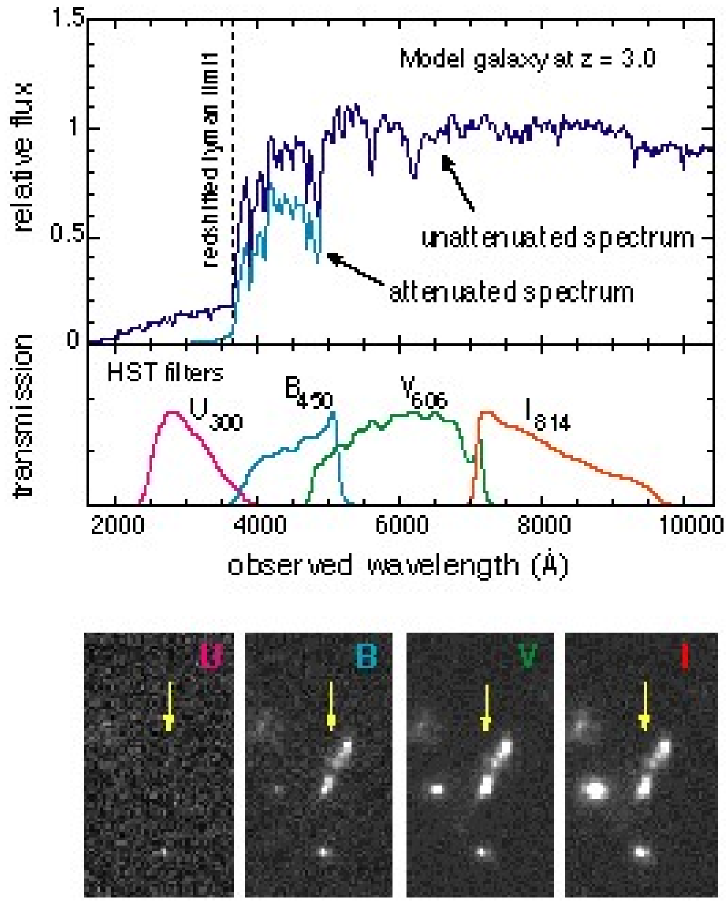

FIGURE 1.3: U-filter dropout of a Lyman Break Galaxy as demonstrated by Dickinson 1998 [15]

In many ways photometric redshift codes apply the same principles as the LBG mehod using the lyman break to detect high redshift galaxies, as these codes also heavily rely on spectral features to give accurate photometric redshift estimates. Many SED fitting codes fit galaxy colors across many filter bands to estimate photometric redshifts, thus these methods are particularly vulnerable to color degeneracies. These degeneracies may arise in featureless blue SEDs where the 912Å restframe Lyman break may be mistaken for the 3646Å Balmer break (Brammer, van Dokkum, and Coppi 2008 [16]). A degeneracy in the redshift estimate then arises as the code can fit the data equally well with a $z \approx 0$ or $z \approx 3$ SED. Therefore SED fitting codes are typically sensitive to spectral features such as the Lyman or Balmer breaks, or even certain PAH signatures (Negrello et al. 2009 [17], Walcher et al. 2011 [18]).

1.4 A new type of galaxy: The dusty star-forming galaxy

The star-forming regions of galaxies are often significantly dust obscured and hence optically thick to UV radiation. This significant extinction of optical UV light makes them unavailable to the LBG dropout test. At high redshift these dust obscured galaxies are very faint in the optical and some completely invisible even to the Hubble Space Telescope (also known as HST-dark galaxies). This elusive new type of galaxy in question is, the already briefly mentioned, dusty star forming galaxies (DSFGs). DSFGs are very luminous in the infrared regime as dust grains absorb optical radiation from young stars and re-emit it as thermal blackbody radiation at long submillimeter infrared wavelengths. Thus the origin of the initial name Submillimeter Galaxies (SMGs), Blain et al. 2002 [19]. First discovered by Smail, Ivison, and Blain 1997 [20], Hughes et al. 1998 [21] and more following the commencement of the JCMT SCUBA camera (Holland et al. 1999 [22]), which saw first light in July 1996, the DSFG is one of the most recent discoveries in modern astronomy. With this discovery, a revision of galaxy formation and evolution theory was eminent as a large portion of star formation had been completely overlooked by UV and optical surveys as Equation 1.2 indicate.

With their characteristic high emission at infrared wavelengths, classifying DSFGs by their infrared luminosity has become the standard approach to separate galaxies. E.g. galaxies with $L_{IR} = 10^{11} L_{\odot}$ go under the term LIRGs (Luminous Infrared Galaxies) and $L_{IR} = 10^{12} L_{\odot}$ are called ULIRGs (Ultra-LIRGs). These ULIRGs are often associated with starbursts, and SFRs as high as $2000 M_{\odot} \mathrm{yr}^{-1}$ have been observed for dusty sources at $z = 2.3$ (Fu et al. 2013 [23]). However, inferring galactic properties such as SFR by directly relating UV-optical observations to infrared observations of the same galaxy may not be as straightforward as previously believed. Careful studies of HST detected UV-optical emission and ALMA detected IR emission of high redshift DSFGs have shown a distinct spatial offset between the two components. Hodge et al. 2016 [24] found that HST H-band imaging tracing the stellar emission appeared rather extended and largely uncorrelated with the dusty regions containing the bulk of star formation. Likewise Gómez-Guijarro et al. 2018 [25] found irregular and extended UV emission compared to compact rest-frame FIR emission and emphasized its effect on elevating the infrared excess (IRX-β) of DSFGs, which sometimes matches the excess inferred by the Calzetti et al. 2000 [26] dust law but at other times is off by orders of magnitude (McLure et al. 2018 [27]). The uncertainty in the infrared excess carries on to the UV spectral slope, β, which has a problematic impact on energy balancing arguments for SED fitting codes that assume coincident UV-IR emission as da Cunha et al. 2015 [28] demonstrated using MAGPHYS. Inevitably this affects SED estimated parameters such as star formation rates. Elbaz et al. 2018 [29] conducted a study illustrating the underestimating effect on SFRs for starbursting galaxies where rest-frame UV and FIR emission occupied different distinct regions. Elbaz et al. determined the ratio of $\mathrm{SFR_{tot}} = \mathrm{SFR_{UV}} + \mathrm{SFR_{IR}}$ (with SFR_{UV} and SFR_{IR} determined according to Kennicutt 1998 [30], Daddi et al. 2004 [31]) to $\mathrm{SFR_{SED}}$ where EAZY was used to determine $\mathrm{SFR_{SED}}$ by fitting rest-frame UV-optical-NIR data. They found $\mathrm{SFR_{tot}}/\mathrm{SFR_{SED}} \sim 1$ for disks with no signs of disturbance and no offset between UV and IR light, while $\mathrm{SFR_{tot}}/\mathrm{SFR_{SED}} >> 1$ for increasingly starbursting galaxies with disconnected UV and IR regions. Thus it seems particularly problematic for SED-fitting to correctly estimate the total SFR, as part of the star forming population may be entirely missed. In a detailed 30 mas (200 pc) resolution ALMA study of 3 DSFGs, Rujopakarn et al. 2019 [32] showed that UV-emitting clumps of star formation offset from the bulk of star formation near the center of the galactic center only contributed with $1-7\%$ of the total star formation of the galaxies. If UV-optical HST data is used to infer the total SFR of a galaxy from such a UV bright region, the SFR will be severely underestimated.

Regarding their role in galaxy formation and evolution, DSFGs and their elevated SFRs are believed to evolve from mergers of molecular gas-rich disk galaxies. Upon collision, compression and cooling of gas sets off star formation activity. This elevated SFR initializes the production of dust particles, which enshrouds the merger causing significant attenuation of the stellar UV radiation from young massive stars. Over cosmic time DSFGs are believed to shed their dust exposing a luminous quasar and eventually evolving into the dead massive elliptical galaxies we see today, (Sanders et al. 1988 [33], Hopkins et al. 2008 [34], Toft et al. 2014 [35]). Dusty quasars have already been found (Blain et al. 2013 [36] etc.) and such AGN can be detected in numerous ways. Typically, AGN are detected by searching for an abundant X-ray signature as high energetic photons are produced in the violent accretion disks of the AGN. This direct approach for detecting AGN X-rays tends to fail in dense environments where the AGN is Compton-thick (Daddi et al. 2007 [37]). Probing for AGN is then best done through other signatures in multiwavelength data where they exhibit different features in the galaxy SED. The AGN can smoothen out the features in the MIR as the thermally emitting AGN-heated dust leaves a power law in the MIR. Dust heating is a particularly rich mechanism with many different contributors. Apart from young stars, AGN and (to an extent) the old stellar population, can heat the dust population, which can contaminate the conversion of infrared luminosity to SFR in Equation 1.2.

As demonstrated throughout this section, many considerations go into the characterization of DSFGs. In the following of this thesis we will make an attempt at determining properties such as photometric redshift and FIR fluxes for catalogued DSFGs to test the robustness of the energy balance principle for this galaxy type. The data in question comes from the 69arcmin^2 1.1mm GOODS-ALMA survey by Franco et al. 2018 [38], Franco et al. 2020 [39], and Franco et al. 2020 [40] where 39 sources are detected with sample redshifts at, or beyond, the peak of cosmic star formation. However, before digging into the practical analysis, we have to establish the necessary theoretical framework.

Chapter 2

Theory

2.1 Physics of the expanding Universe

Ever since the Big Bang the Universe has continued expanding. The first scientist to make this realization and to attempt quantifying this acceleration was Hubble 1929 [41]. Hubble obtained spectrographic data of distant galaxies to measure the shift of emission lines relative to the rest frame spectra. By doing so Hubble could determine Doppler shifts of these emission lines which he ascribed to their recession velocity relative to us. The remarkable revelation of Hubble was that most galaxies were moving away from us, and that this recession was increasing at a constant rate with proper distance.

$$\vec{v}_0 = H_0 \vec{r}_0 \tag{2.1}$$

Where the subscript denotes values at our current time, e.g. $t = 0$.

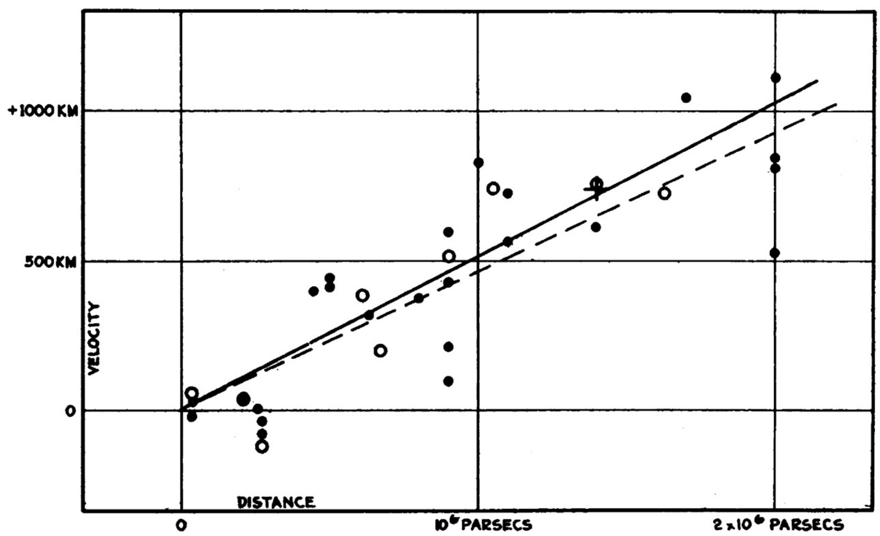

FIGURE 2.1: Hubble diagram illustrating the accelerating recession velocity of distant galaxies (Hubble 1929 [41])

From the slope of the Hubble diagram (Figure 2.1) Hubble estimated this constant increase in recession velocity by $H_0 = 500\text{km/s/Mpc}$. This parameter, H_0, now also known as the Hubble constant, has since this first study become a crucial parameter in astrophysics, and consequently it has been determined with much higher accuracy and precision. As alluded to in Equation 2.1 the Hubble constant turns out to be a time-dependent parameter. This can be deduced if we consider the proper coordinate $\vec{r}(t)$ dependent on time due to the expansion of the Universe, and a comoving coordinate system where the time-dependence of the corresponding vector, $\vec{\mathcal{R}}$, is contained in a scale factor accounting for the expansion of the Universe, e.g. $\vec{r}(t) = a(t)\vec{\mathcal{R}}$. The recession velocity, $\vec{v}\,(\vec{r}, t) = \dot{\vec{r}}$, is then given by.

$$\vec{v}\,(\vec{r}, t) = \frac{\dot{a}}{a}\vec{r}(t) = H(a)\vec{r} \tag{2.2}$$

With The Hubble law (Equation 2.2) Edwin Hubble argued that the Universe is continually expanding.

The pioneering discovery by Hubble was accompanied by a flood of new questions. If the Universe is expanding, will the expansion continue forever, or stop at some point? What did the expansion history of the Universe look like up to our current time? These were the early questions being addressed by independent cosmologists around the world. By considering a homogeneous and isotropic spacetime and a smooth spatial distribution of matter in the Universe, a decade-long collective effort by Friedmann, Lemaître, Robertson and Walker led to the FLRW metric.

$$ds^2 = c^2dt^2 - a(t)^2\left(d\chi^2 + f_K(\chi)^2\left(d\theta^2 + \sin(\theta)^2 d\phi^2\right)\right) \tag{2.3}$$

Where ds is an infinitesimal line element between two points in spacetime described by the comoving coordinates (t, χ, θ, ϕ) and the scale factor, $a(t)$. The function $f_K(\chi)$ depends on the radial coordinate χ and its expression also changes depending on the curvature parameter, K.

When applied to the Einstein field equations of General Relativity, the FLRW metric provided an expression for the expansion history of the Universe in one of the most fundamental equations of cosmology, also known as the Friedmann equation.

$$\left(\frac{\dot{a}}{a}\right)^2 = \frac{8\pi G}{3c^2}\epsilon(t) - Kc^2 a(t)^{-2} \tag{2.4}$$

Where $\epsilon(t)$ describes the energy density of the Universe, K is the curvature of spacetime, and we know $H(a) = \dot{a}/a$. A common version of the Friedman equation is often given in terms of the density parameters, $\Omega_{i,0} = \rho_{i,0}/\rho_{crit}$. Where ρ_{crit} is the density in todays flat Universe ($t = 0$, $K = 0$), $\rho_{crit} = 3H_0^2/8\pi G$ from Equation 2.4.

$$H(a)^2 = H_0^2\left(\frac{\Omega_{m,0}}{a^3} + \frac{\Omega_{r,0}}{a^4} + \Omega_\Lambda + \frac{\Omega_K}{a^2}\right) \tag{2.5}$$

This special equation enables us to make predictions about the future of the Universe, but it also tells an interesting story about its evolution up to our present day. The implications of the FLRW metric and the assumptions of a homogeneous and isotropic Universe are extensive. In this simplified Universe, we can also assume that emitted photons travel only radially such that $d\theta = d\phi = 0$, and as a result of General Relativity, photons travel along null geodesic paths where $ds^2 = 0$. Coupled with the assumption of a flat Universe, meaning $f_0(\chi) = \chi$, the FLRW metric (Equation 2.3) can be written as $c^2dt^2 = a^2d\chi^2$. The comoving distance, χ, can then be determined by substituting in the Friedmann equation (Equation 2.5), using the relationship between scale factor and redshift $a^{-1} = 1 + z$, followed by rearringing and integration.

$$\chi = c \int_0^z \frac{dz}{H(z)} \tag{2.6}$$

Determining redshifts and distances enables us to map the Universe around us. Typically the observables that astronomers measure are photometric fluxes or galaxy spectra from spectroscopy. With a photometric flux density and a measured distance we can determine the total electromagnetic power irradiated - the luminosity - of an astronomical object.

In the local Universe where the Hubble flow is negligible, an Euclidian static spacetime can be assumed. Under these assumptions the observed flux density is related to the luminosity distance, which is just a proper distance $D_L = D$, by the inverse square law, so we can express the rest frame luminosity:

$$L^{rest} = 4\pi D^2 f^{obs} \tag{2.7}$$

However, if we consider a non-Euclidian spacetime we see that as we go to higher redshift, the arrival rate of photons decreases by a factor of $(1 + z)$ and each photon has less energy as the photons frequency decreases by an additional $(1 + z)$. This means that the luminosity distance becomes $D_L = (1 + z)D$ (Weedman 1986 [42] p. 61).

$$L^{rest} = 4\pi D_L^2 f^{obs} \tag{2.8}$$

Oftentimes we do not have multiwavelength data to cover the entire electromagnetic spectrum to determine bolometric quantities. Therefore the luminosity and fluxes are typically spectral quantities per unit wavelength or frequency. Over a given bandpass the bolometric luminosity is then $L^{rest} = L_\lambda^{rest} d\lambda^{rest}$ and the flux density $f^{obs} = f_\lambda^{obs} d\lambda^{obs}$. But we have to remember that the observed wavelengths are lengthened, $d\lambda^{obs} = d\lambda^{rest}(1 + z)$.

$$L_{\lambda}^{rest} d\lambda^{rest} = 4\pi D_L^2 f_{\lambda}^{obs} d\lambda^{obs} \tag{2.9}$$

Rearranging we can get an expression for the rest frame luminosity per unit wavelength.

$$L_{\lambda}^{rest} = 4\pi D_L^2 f_{\lambda}^{obs} \frac{d\lambda^{obs}}{d\lambda^{rest}} = 4\pi D_L^2 f_{\lambda}^{obs} \frac{d\lambda^{rest}}{d\lambda^{rest}}(1+z) = 4\pi D_L^2 f_{\lambda}^{obs}(1+z) \tag{2.10}$$

This expression provides a practical method to derive characteristic properties of galaxies.

2.2 Galactic extinction and cosmic dust

Throughout this study we will use the spectral luminosity to derive characteristics such as the output infrared luminosity by integrating Equation 2.10 from $8\mu m$ to $1000\mu m$.

$$L_{IR} = \int_{8\mu m}^{1000\mu m} L_{\lambda}^{rest} d\lambda \tag{2.11}$$

This infrared emission is dominated by re-radiated electromagnetic radiation from stellar objects. UV-optical emission from the stars heat the dust grain population, and in turn these dust grains re-emit black body radiation according to their temperature.

The real mechanics of grain heating and infrared emission is complicated as the grain population may be separated into several populations by temperature. For instance, the cold fraction of the dust population may be heated by the constant radiation from the interstellar radiation field, while the hot population situated in photodissociation regions is additionally heated by much more intense radiation. Thus the infrared SED may be a combination of modified blackbodies with emissivity indices such as $\beta = 1$, $\beta = 1.5$ and $\beta = 2$ corresponding to hot, warm, and cold dust etc.

Nevertheless dust grains have an evident attenuation effect on incident starlight. The exact change in radiation intensity is contained in the equation of radiative transfer which describes the evolution of the intensity when propagating in matter that can alter the intensity through absorption, emission or scattering processes (Chandrasekhar 1950 [43] p. 8).

$$\frac{1}{c}\frac{\partial I_{\nu}}{\partial t} + \left(\hat{\Omega} \cdot \nabla\right) I_{\nu} = -\kappa\rho I_{\nu} + j_{\nu}\rho + \frac{\kappa_s \rho}{4\pi} \int I_{\nu}'(\Omega')\Phi(\Omega,\Omega')d\Omega' \tag{2.12}$$

Where Ω is the solid angle, $\kappa = \kappa_a + \kappa_s$ is the total extinction coefficient due to absorption κ_a, and scattering κ_s, j_{ν} is the emissivity, ρ is the density, and Φ is the scattering function.

The first term on the left hand side describes change in intensity with time, and the second term describes the spatial change in intensity along the $\hat{\Omega}$ line of sight direction. This is equal to the right hand side where the first term denotes the decrease in radiative intensity due to scattering and absorption. The second term on the right hand side describes the emissivity increasing the intensity in the $\hat{\Omega}$ line of sight direction. The last term describes how the scattering of photons in all directions change the intensity in the $\hat{\Omega}$ direction.

This equation, in its most general form, looks overwhelmingly complex, but with a wide range of assumptions we can simplify this expression significantly. If the galaxy emission is in a steady state $\partial I_\nu/\partial t = 0$, and in the plane parallel case $(\hat{\Omega} \cdot \nabla) I_\nu = -\cos(\theta) dI_\nu/dz = dI_\nu/ds$. Furthermore, if we consider only absorption $\kappa_s = 0$ ($\kappa = \kappa_a$) and an insignificant emissivity into the line of sight direction, $j_\nu = 0$.

$$\frac{dI_\nu}{ds} = -\kappa\rho I_\nu \tag{2.13}$$

Which has the general solution

$$\begin{aligned}
\frac{dI_\nu}{I_\nu} &= -\kappa\rho ds \\
\int_{I_\nu(s'=0)}^{I_\nu(s'=s)} \frac{dI_\nu}{I_\nu} &= -\int_{s'=0}^{s'=s} \kappa\rho ds' \\
\ln(I_\nu(s)) - \ln(I_\nu(0)) &= -\tau_\nu(s) \\
I_\nu(s) &= I_\nu(0)\exp(-\tau_\nu(s)) \qquad (2.14)
\end{aligned}$$

Where we have defined the optical depth

$$\tau_\nu(s) = \int_{s'=0}^{s'=s} \kappa\rho ds' \tag{2.15}$$

This reduction of the initial specific intensity by a factor $\exp(\tau)$ in Equation 2.14 translates directly to the flux density, as the flux density is just the specific intensity integrated over the solid angle.

$$f_\nu = f_\nu(0)\exp(-\tau_\nu) \tag{2.16}$$

The flux density is directly related to the magnitude of the source by

$$m = -2.5\log_{10}(f_\nu) + C \tag{2.17}$$

The constant C is the zeropoint value where $m = 0$, which is different in different astronomical magnitude systems (e.g. 48.60erg $s^{-1}cm^{-2}Hz^{-1}$ in the AB magnitude system) and may vary between instruments.

We can define the extinction as the difference in magnitude in the same band with and without extinction.

$$A_\nu = m - m_0 = -2.5\log(f_\nu) + 2.5\log(f_\nu(0)) = -2.5\log\left(\frac{f_\nu}{f_\nu(0)}\right) = -2.5\log(e)\tau_\nu \tag{2.18}$$

If we know the magnitude with and without dust in two different bands, we can compare the amount of extinction in these different bands with the ratio A_{ν_1}/A_{ν_2}. Comparisons are typically done with respect to the V-band extinction, and another band, e.g. A_λ/A_V.

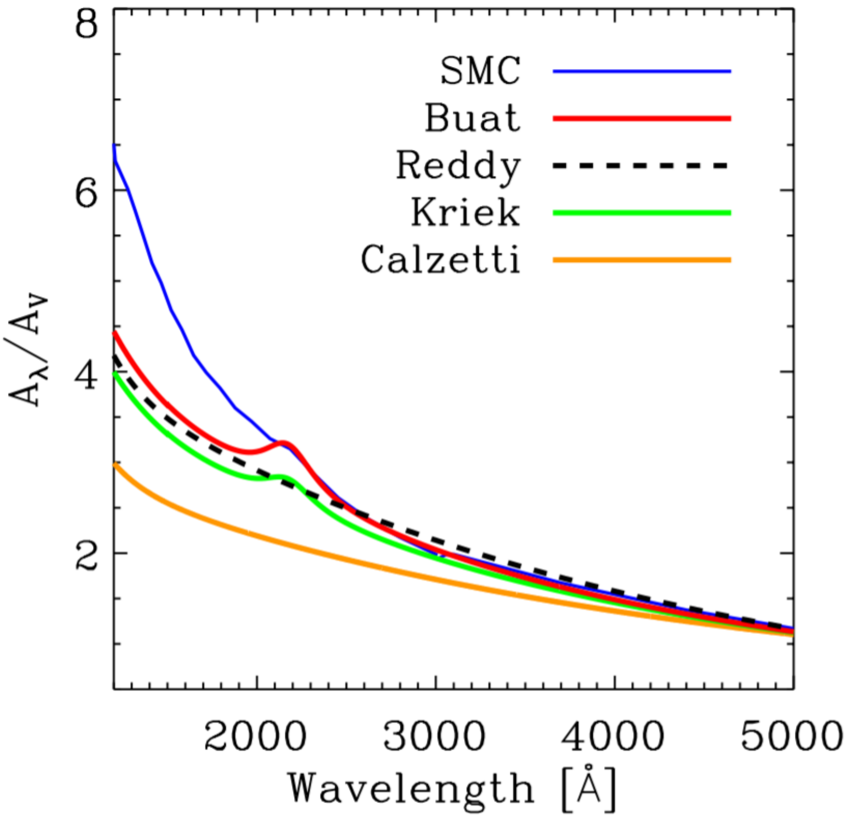

FIGURE 2.2: Attenuation curves at $z > 0.5$ (Salim and Narayanan 2020 [44])

As can be seen on Figure 2.2 the extinction is largest for short optical radiation and drops off at longer wavelengths, which is why long infrared wavelengths travel mostly unattenuated along their paths to our telescopes (apart from atmospheric interference). Very dusty galaxies with a large amount of infrared emission may therefore be completely undetected in the optical bands due to their significant dust extinction. A characteristic feature of the attenuation curve is the 2175Å bump or lack thereof. Since its discovery by Stecher 1965 [45] the 2175Å bump has remained one of the great unsolved mysteries of extragalactic astronomy. Over the decades various explanations have been offered to the origin of this feature, which seems to vary in both strength and width around its consistent central wavelength around 2175Å. Generally, astrophysicists agree that a feature this prominent in the attenuation of curve of galaxies must be associated with a fairly abundant component of the galactic ISM. While the ISM dust grain populations typically seem to be dominated by silicates and carbonaceous (graphite and PAHs) grains, the latter seems to be the most popular candidate for explaining the 2175Å bump. For some galaxies the 2175Å bump may be very weak or almost completely gone. Gordon, Calzetti, and Witt 1997 [46] and Witt and Gordon 2000 [47] showed that starburst galaxies with SMC-like dust (dominated by silicate grains) would produce a bump-free attenuation curve. While the features of the attenuation curve depends on the ISM dust grain population it also depends on the redshift of the galaxy at hand as high-z galaxies have had less time to equilibrate kinematically and also have lower metallicities which may limit grain production and e.g. depletion of exotic elements onto dust grains affecting the dust attenuation curve. For these high redshift galaxies numerous attempts have been made to characterize the attenuation curve by empirical methods from sampled galaxies (like starburst) or model based methods. Figure 2.2 shows attenuation curves for higher redshift galaxies at $z > 0.5$. Among the most popular dust models is the empirical Calzetti et al. 2000 [26], which is derived from a sample of local starburst galaxies. Reddy et al. 2015 [48] is another empirical study where MOSFIRE spectroscopic data of 224 star-forming galaxies is processed. Other approaches by e.g. Buat et al. 2012 [49] and Kriek and Conroy 2013 [50] are based on SED fitting models.

Regardless of the dust attenuation law assumed, the dust population has a significant attenuating effect on starlight from dusty galaxies observed. This effect can be quantified by measuring magnitudes in instrument filter bands to infer properties of galaxy samples.

2.3 UVJ color selection

A helpful diagnostic tool for distinguishing star-forming galaxies from quiescent galaxies is the UVJ color-color diagram. To get the UVJ colors the respective U-, V-, and J-fluxes are first calculated by convolving the SED through the filters. The color is then given by subtracting the magnitudes given by Equation 2.17

$$U - V = -2.5 \log_{10}(U_{\text{flux}}/V_{\text{flux}}) \tag{2.19}$$

Where $U = m_U$ is the U-band magnitude and $U_{\text{flux}} = f_{\text{U}}$ is the flux density in the U-band etc. Williams et al. 2009 [51] were among the first employ this color based selection method, and furthermore defined a set of selection criteria

$$
\begin{aligned}
(U - V) &> 0.88 \times (V - J) + 0.69 \qquad [0.0 < z < 0.5] \\
(U - V) &> 0.88 \times (V - J) + 0.59 \qquad [0.5 < z < 1.0] \\
(U - V) &> 0.88 \times (V - J) + 0.49 \qquad [1.0 < z < 2.0]
\end{aligned} \tag{2.20}
$$

Along with a criteria of $U - V > 1.3$ and $V - J < 1.6$ these criteria define a clear region within the UVJ diagram where we can distinguish quiescent galaxies from star-forming galaxies. Figure 2.3b demonstrates the color selection region where galaxies may be identified as quiescent for the given redshift intervals. In Williams et al. 2009 [51] the bimodal distribution of quiescent and star-forming galaxies seems to disappear at higher redshift, $z > 2$, partly due to larger photo-z errors and passive evolution. At higher redshift (around and beyond the peak of star formation, Figure 1.2) a larger portion of galaxies are still in their early evolutionary stages and thus the fraction of dusty star-forming galaxies is larger.

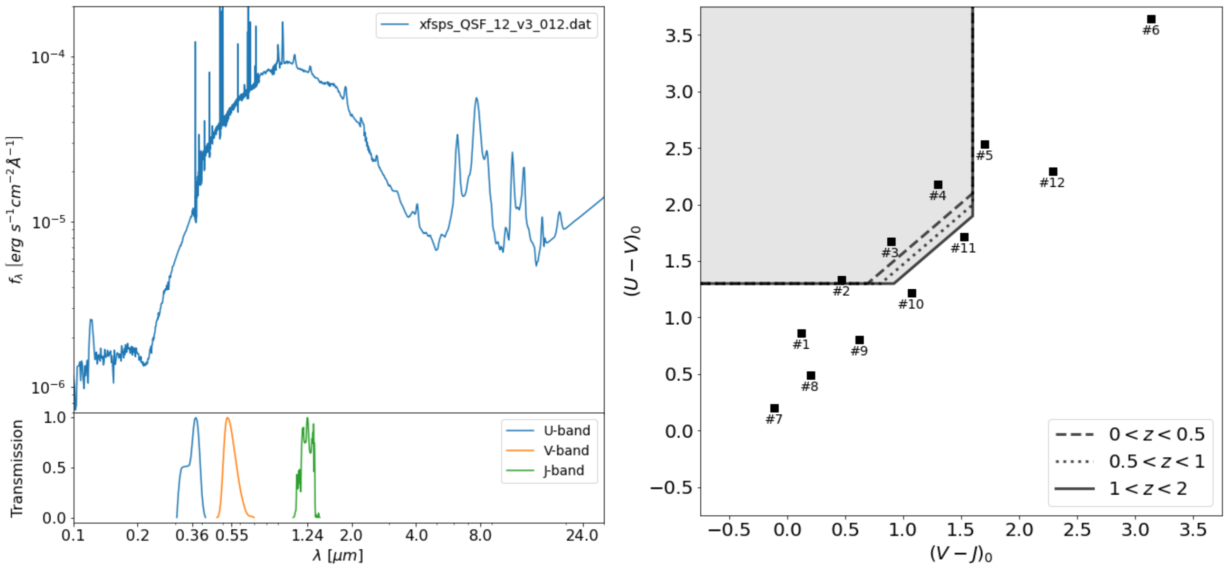

(A) (B)

FIGURE 2.3: 2.3a) UVJ filter transmission curves along with an example galaxy. 2.3b) UVJ-color diagram with a set of galaxies plotted (black squares) along with the region defined by Williams et al. 2009 [51] to distinguish quiescent galaxies from star forming galaxies

Having established the fundamentals of the alteration of light in the expanding Universe, along with dust attenuation effects and UVJ selection of galaxies, we are ready to apply these techniques and delve into the practical aspect of this study.

Chapter 3

Methods

In many astrophysical studies, authors use modeled SEDs to extrapolate fluxes as multiwavelength data across the entire electromagnetic spectrum is often unavailable. These fluxes are then used to derive parameters related to gas mass, galaxy star formation rates (SFRs) etc. at different epochs in the Universe. In the third chapter of this study, we use the EAZY photometric redshift tool (Brammer, van Dokkum, and Coppi 2008 [16]) to determine redshifts and spectral energy distributions (SEDs) for galaxies discovered in the 69arcmin^2 GOODS-ALMA survey conducted by Franco et al. 2018 [38], Franco et al. 2020 [39], and Franco et al. 2020 [40]. Furthermore, a detailed review and optimization of the underlying set of galaxy templates used to construct the model SED is carried out. The 1.1mm fluxes derived from the modelled SEDs are then compared with the ALMA fluxes reported by Franco et al. to test the robustness of the energy balance principle.

3.1 The GOODS-ALMA survey

Throughout this study a sample of DSFGs within the GOODS-S cosmological legacy field is utilized. These sources are detected in the 69arcmin^2 1.1mm GOODS-ALMA survey by Franco et al. 2018 [38], Franco et al. 2020 [39], and Franco et al. 2020 [40]. With a 0.6arcsec limiting resolution the authors detect galaxies down to a limit of 3.5σ_{RMS} by also using Spitzer/IRAC and VLA to detect the faintest galaxies below 4.8σ_{RMS}. The sample consists of DSFGs elevated above the main sequence of star formation, and with low gas fractions and short depletion timescales these galaxies will be depleted in a short time. Furthermore the galaxies are among the most massive galaxies at $z = 2 - 4$ with a median stellar mass of $M \approx 8.5 \cdot 10^{10} M_{\odot}$. Roughly $\sim$ 19/33 galaxies have a 7 Ms survey X-ray counterpart from the Luo et al. 2017 [52] survey of the Chandra Deep Field–South. However, Franco et al. emphasize that an X-ray signature does not necessarily mean the galaxy hosts an AGN, but rather they adopt a threshold of $L_{X,int} > 10^{43}$erg/s. About half of the $L_{X,int} > 10^{43}$erg/s galaxies exhibit low gas content and short depletion timescales possibly due to AGN feedback preventing infall of gas. Franco et al. argue that these may be the progenitors of compact elliptical galaxies. No exact amount of AGN hosting galaxies is provided but we assume this to be about ~ 10. This AGN fraction is worth noting as codes like EAZY use stellar population synthesis models roughly built from dust, gas, and stars, which will have difficulties fitting a strong AGN contribution.

To model these galaxies we start with the establishment of the fundamental principles of the Stellar Population Synthesis Models that are contained in the template sets used by EAZY to fit galaxy SEDs. Then an introduction of the EAZY SED fitting code is given before jumping into the more practical aspect of predicting the FIR SED.

3.2 Stellar Population Synthesis Models

The process of deriving galaxy SEDs starts with the templates used to represent any given sample. These galaxy templates contain the most interesting details vital to producing a good SED fit. In this study the sample representative template sets are derived from computational Stellar Population Synthesis (SPS) Models . The topic of SPS Models is broad and an extensive discussion of the encompassing details is not within the scope of this project. Instead we summarize the key aspects of SPS Models and refer to Conroy 2013 [53] for a detailed discussion. As galaxies are conceptually just a collection of stars, gas, dust, and possibly an AGN, a lot of effort go into determining the interplay between these components. Therefore a key aspect SPS models revolves around modelling the stellar population. Put in very rough terms, 3 ingredients are required to build a simple stellar population (SSP) and 2 additional ingredients to advance the SSP to a composite stellar population (CSP) as illustrated on Figure 3.1.

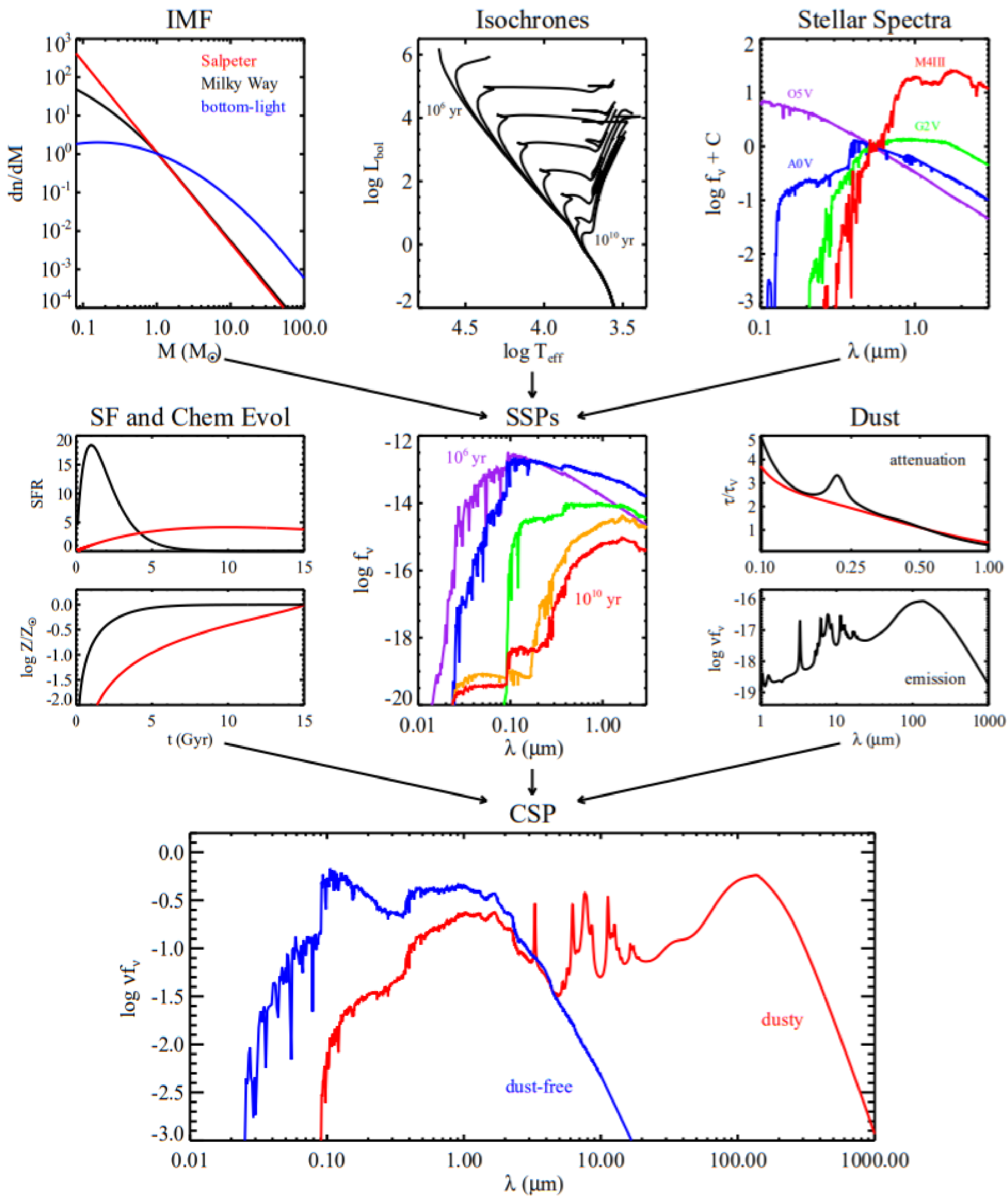

FIGURE 3.1: The basic ingredients that go into determining SSPs and CSPs. Credit: Conroy 2013 [53]

The components that go into developing an SSP can be summarized in three parts.

1. The IMF, as described in subsection 1.2.1, provides essential information for the SPS model including stellar mass-to-light ratio, and the passive evolution of the galactic luminosity. The IMF does however not change the galactic SED significantly as the

SED is dominated by more massive stars where IMFs like the Salpeter and Kroupa model are in agreement with eah other.

2. Isochrones specifying the stellar evolution of stars with the same age and metallicity. A table of isochrones spanning several evolutionary tracks in the Hertzsprung-Russell (HR) diagram is needed to produce a good SSP.

3. Stellar spectra are required to convert parameters from stellar evolution calculations into SEDs.

To advance the SSP to a CSP two additional elements are required, namely.

1. SFHs and information regarding chemical evolution. The SFH is used to define the age of the different stars of the stellar population, while the metallicities of these differently aged stars is contained within the time-dependent chemical evolution.

2. Dust models are required to characterize the attenuation of stellar light and subsequent infrared emission.

For SPS models we sometimes also want emission lines to be as realistic as possible, therefore it may be beneficial to include nebular line emission under certain circumstances. These emission lines are particularly important in low metallicity environments, as well as in high redshift galaxies where emission features with a rest-frame equivalent width, due to redshifting effects, will be broadened and thus occupy an increasingly larger fraction of the filter bandpass.

With the very basics of SPS models established detailed galaxy spectra can be generated using codes like Flexible Stellar Population Synthesis for Python (FSPS, Conroy, Gunn, and White 2009 [54], Conroy and Gunn 2010 [55]). These artificial templates can be used to model broadband photometry and derive SEDs and thus inherent properties of real observed galaxies. In the Franco et al. papers SED fitting codes like Code Investigating GALaxy Emission (CIGALE, Burgarella, Buat, and Iglesias-Páramo 2005 [56], Noll et al. 2009 [57], Boquien et al. 2019 [58]) were used to derive such galaxy properties. To fit the DSFGs Franco et al. split their sample into two separate cases; 1) Sources with a matching Herschel counterpart and 2) Sources without a matching Herschel counterpart.

1. Sources with a Herschel counterpart are fit with CIGALE. Similar to other SED fitting codes CIGALE uses CSP from SPS models to fit galaxy SEDs. Franco et al. uses the SPS models from Bruzual and Charlot 2003 [59] and the Calzetti et al. 2000 [26] dust attenuation law. The Draine et al. 2014 [60] dust models were used to fit the infrared regime of the SED while even longer radio wavelengths are added after

SED fitting using a FIR to radio luminosity ratio of 2.34 (Yun, Reddy, and Condon 2001 [61]). UV to 16μm are fit independently from 24μm to millimeter wavelengths.

2. For galaxies without a Herschel counterpart the SED fitting is done iteratively. The dust SED fit is done using the Schreiber et al. 2018 [62] models normalized to the 1.13mm ALMA flux density in the SED. The galaxy is also fit with a main sequence star forming galaxy whereafter T_{dust} and the IR8 $= \mathrm{L_{IR}/L_8}$ are then determined and constrained on the next iteration to generate a the new SED.

Galaxies believed to host an AGN (X-ray luminosity $L_{X,int} > 10^{43}$erg s^{-1} are treated using the Mullaney et al. 2011 [63] DECOMPIR code where the Kirkpatrick et al. 2015 [64] models are used to extrapolate to shorter wavelengths below 5μm. While Franco et al. use CIGALE which itself employs an energy balancing method assuming a one-to-one correspondence of the emitted UV and infrared luminosity, the SEDs are fit independently in the UV-optical and FIR region with seemingly no scaling imposed to ensure energy balance.

In this thesis we employ another SED fitting routine, EAZY, similarly using SPS models to fit galaxy SEDs. However, to conserve energy balance across the SED, we do the SED fitting across the entire data range (not independently fitting part of the data).

3.3 EAZY - A photometric redshift code

Photometric redshifts for highly obscured DSFGs pose a range of issues and are notoriously known for being unreliable (Casey et al. 2012 [65]). Difficulties involve reddening due to dust grains, which may translate to an overshooting of the redshift estimate. Another underestimating effect comes from star formation in the multiphase ISM of the galaxy. Lyα photons generated from star formation can bounce off ISM clouds and escape the galaxy at a higher rate than if the ISM is assumed to be uniform, which is often the case. This makes the Lyα line appear narrower in the UV, which might be misinterpreted as a lower redshift Neufeld 1991 [66].

Thus, many phenomena has to be taken into account when computing galaxy redshifts. The most reliable redshift determinations come from spectroscopic surveys. However, a basic limitation of spectroscopic surveys is the signal-to-noise ratio (SNR) which decreases with resolution inversely but increases with exposure time linearly SNR $\propto t/\sqrt{R}$. The difference in resolution between photometric and spectroscopic surveys are typically orders of magnitude. For a spectroscopic survey to obtain an SNR equivalent to its photometric counterpart, the exposure time typically has to be increased by 1-2 orders of magnitude. This demanding exposure time poses a limitation, which makes it hard to obtain deep spectroscopic data for very faint subjects.

EAZY was built to determine photometric redshifts where spectroscopic data is unavailable. Typically, the greatest source of error in photometric template fitting codes is the template mismatch between the fitted data and the template, however EAZY enables the user to use a linear combination of several templates (e.g. Rudnick et al. 2001 [67]), where the weighing coefficients of each template are then determined according to the Sha et al. 2007 [68] algorithm. As described extensively in Brammer, van Dokkum, and Coppi 2008 [16], EAZY determines photometric redshifts and SEDs by using a simple χ^2 minimization technique. EAZY iterates through a grid of redshifts defined by the user, and determines the χ^2 of the fit at each point. To treat redshift degeneracies EAZY constrains the best fitting redshift from the posterior redshift probability distribution, $p(z \mid m_{0,i}, C)$, which is the product of a Bayesian redshift-magnitude prior, $p(z \mid m_{0,i},$ and a conditional redshift probability, $p(z \mid C)$, given the χ^2 determined across the redshift grid.

$$
\begin{aligned}
p(z \mid m_{0,i}) &\propto z^{\gamma_i} \exp\left(-\left(\frac{z}{z_{0,i}}\right)^{\gamma_i}\right) \\
p(z \mid C) &= \exp\left(-\frac{\chi^2}{2}\right) \\
p(z \mid m_0, C) &\propto p(z \mid m_0) p(z \mid C)
\end{aligned}
\tag{3.1}
$$

Where γ_i and $z_{0,i}$ are free parameters fit for each magnitude bin. The error on the redshift is determined from percentile confidence limits (usually 16/84 e.g. 68%) where the posterior probability distribution is integrated from the edges in defined by the upper and lower bound of the redshift grid as shown on Figure 3.2.

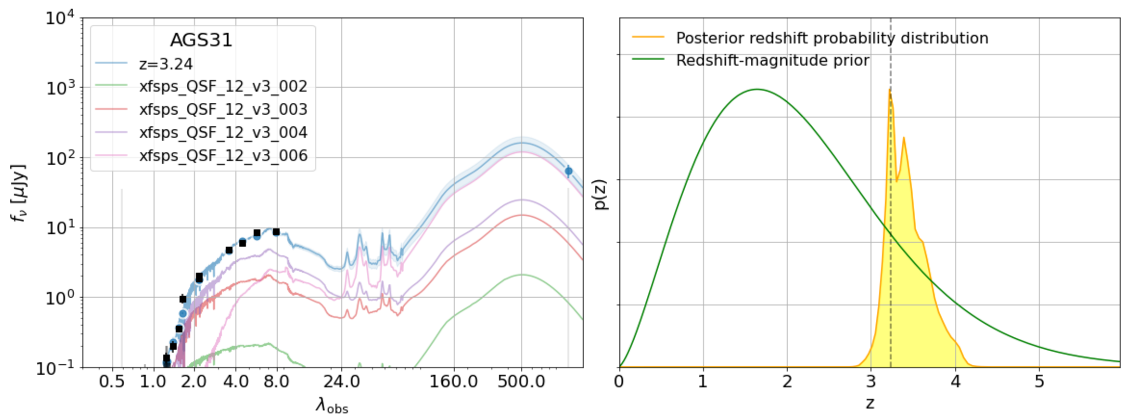

FIGURE 3.2: Demonstration of EAZY showing the SED fit, prior adopted, and posterior redshift probability distribution

EAZY also employs a variety of measures to minimize the template error, including the use of a template error function. Photometric redshifts are first computed with a a uniform template error function. Then residuals between SED model fit and catalogue observations are computed and de-redshifted into the restframe. The residuals are then binned and their median values are fitted with a smoothly varying function (e.g. a spline). The final template error function is then determined by subtracting the scaled photometric errors in quadrature from the smoothly varying function.

Given the complexity of the procedures of the code, EAZY is surprisingly cost efficient compared to other photometric redshift codes, and is able to fit thousands of galaxies with just seconds of computation time.

3.4 Predicting the 1.1mm flux and FIR of dusty galaxies

In this section we will go over the optimization of galaxy templates used by EAZY, and the resulting SEDs produced from fitting sample of galaxies from Franco et al. 2018 [38], Franco et al. 2020 [39], and Franco et al. 2020 [40].

A catalogue containing UV-optical data was obtained from the Space Telescope Science Institute (STScI) archive, henceforth referred to as the 3D-HST catalogue.

Bands	**Survey**	**Reference**
U, R	ESO GOODS	Nonino et al. 2009 [69]
U38, B, V, Rc, I	GaBoDs	Hildebrandt et al. 2006 [70], Erben et al. 2005 [71]
14 medium band filters	MUSYC	Cardamone et al. 2010 [72]
F435W, F606W, F775W, F850LP	GOODS	Giavalisco et al. 2004 [73]
F606W, F814W	CANDELS	Koekemoer et al. 2011 [74]
J, H, Ks	ESO/GOODS	Retzlaff et al. 2010 [75], Wuyts et al. 2008 [76]
J, Ks	TENIS	Hsieh et al. 2012 [77]
F140W	3D-HST	Brammer et al. 2012 [78]
F125W, F160W	CANDELS	Grogin et al. 2011 [79], Koekemoer et al. 2011 [74]
3.6μm, 4.5μm	SEDS	Ashby et al. 2013 [80]
5.8μm, 8.0μm	GOODS	Dickinson et al. 2003

TABLE 3.1: The photometric catalog for the GOODS-S field retrieved from the 3D-HST archive website and the datasets contained

Using TOPCAT (Taylor 2005 [81]) the right ascension and declination of the 3D-HST catalogue was cross-matched with the right ascension and declination of the Franco et al. catalogue within a 1 arcsecond radius. This was done in order to create a catalogue with 3D-HST data for the Franco et al. AGS sources.

The data has been fit with a variety of templates sets (as previously described in section 3.3) in a Jupyter Notebook running Python 3.6. A range of parameters remained the same regardless of the template set used for fitting. The same redshift-magnitude prior was used throughout all fits and a Milky Way reddening of $E_{B-V} = 0.007$ was determined from the Franco et al. center coordinate $\alpha = 3\text{h}\ 32\text{m}\ 30.0\text{s}$, $\delta = -27^\circ\ 48'\ 00''$[1]. The IGM absorption from intervening HI clouds was corrected according to Madau 1995 [82] and the cosmology was fixed to a flat geometry with $H_0 = 70.0\text{km/s/Mpc}$, $\Omega_M = 0.3$ and $\Omega_\Lambda = 0.7$.

Throughout this study we will refer to a range of template sets developed and utilized for the fitting of the dusty AGS sources. To avoid confusion we adopt simple abbreviations for each template set. Each template set and its purpose will be explained in due time. The template sets written in italics are only discussed in the Appendix A section A.3. Chronologically the template sets are.

XFSPS-12O:
First set of 12 original, 'O', FSPS generated templates.

XFSPS-12M:
A set identical to the XFSPS-12O, apart from the 12th template which has been replaced by an FSPS generated template with the maximum, 'M', L_{IR}/L_V.

XFSPS-1210R:
A set of 22 templates with 12 templates similar to XFSPS-12O but without dust emission, and an addition of 10 raw, 'R', infrared templates undefined below 1μm.

XFSPS-1210Z:
A set identical to XFSPS-1210R but where the 10 infrared additions have been extrapolated to shorter wavelengths below 1μm by direct truncation to zero.

XFSPS-1210P:
A set identical to XFSPS-1210R but where the 10 infrared additions have been polynomially, 'P', extrapolated below 1μm

XFSPS-1210PAH :
A set identical to XFSPS-1210R but where the 10 infrared additions have been smoothly extrapolated to lower wavelengths by using a PAH, 'PAH', component which drops off rapidly at shorter wavelengths.

XFSPS-12SB:
A set of 12 templates including 2 star bursting templates, 'SB'.

The first set of templates used to fit the AGS galaxies was the XFSPS-12O displayed on Figure 3.3 and with UVJ colors shown on Figure 2.3b. Non-negative matrix factorization

[1] https://irsa.ipac.caltech.edu/applications/DUST/

models were used to produce a minimal template set as described in Blanton and Roweis 2007 [83]. This XFSPS-12O set is thus a subsample of a much larger set of galaxy templates, selected to represent a broad diversity of galaxy types as also described in Brammer, van Dokkum, and Coppi 2008 [16].

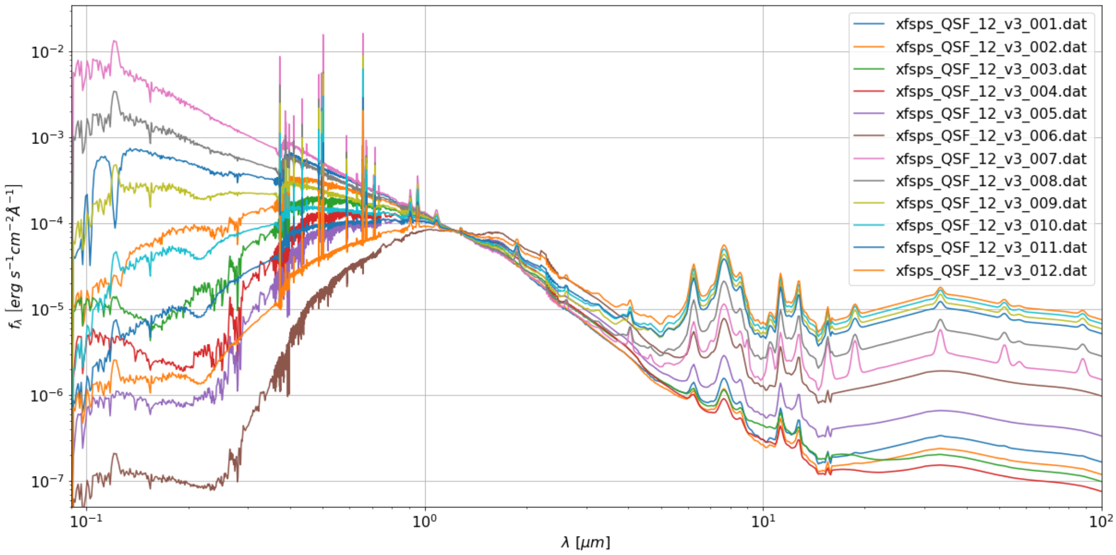

FIGURE 3.3: The 12 galaxy templates of the XFSPS-12O template set

In Franco et al. 2018 [38] and Franco et al. 2020 [39] AGS4, 11, 15, 17, 24, 25 has IRAC data. Among these galaxies only the crossmatch for AGS4, 17, 24 has IRAC data in the 3D-HST catalogue, while the crossmatch for AGS15 has other UV-optical data but no IRAC data, and AGS11 and 25 has no 3D-HST crossmatch and therefore no 3D-HST data.

A handful of other galaxies are lacking information (AGS14, 16, 19) as they are not detected at any other wavelength. Another, AGS22, is at the detection limit with a very weak detection in 1-2 HST-WFC3 bands and no significant detection at other wavelengths. These are most likely spurious sources.

With this in mind we exclude AGS11, 14, 16, 19, 22, 25 such that the final catalogue of galaxies consists of 33 targets from the Franco et al. GOODS-ALMA survey - all with an optical 3D-HST counterpart. The SEDs from fitting the XFSPS-12O set are displayed on Figure 3.4.

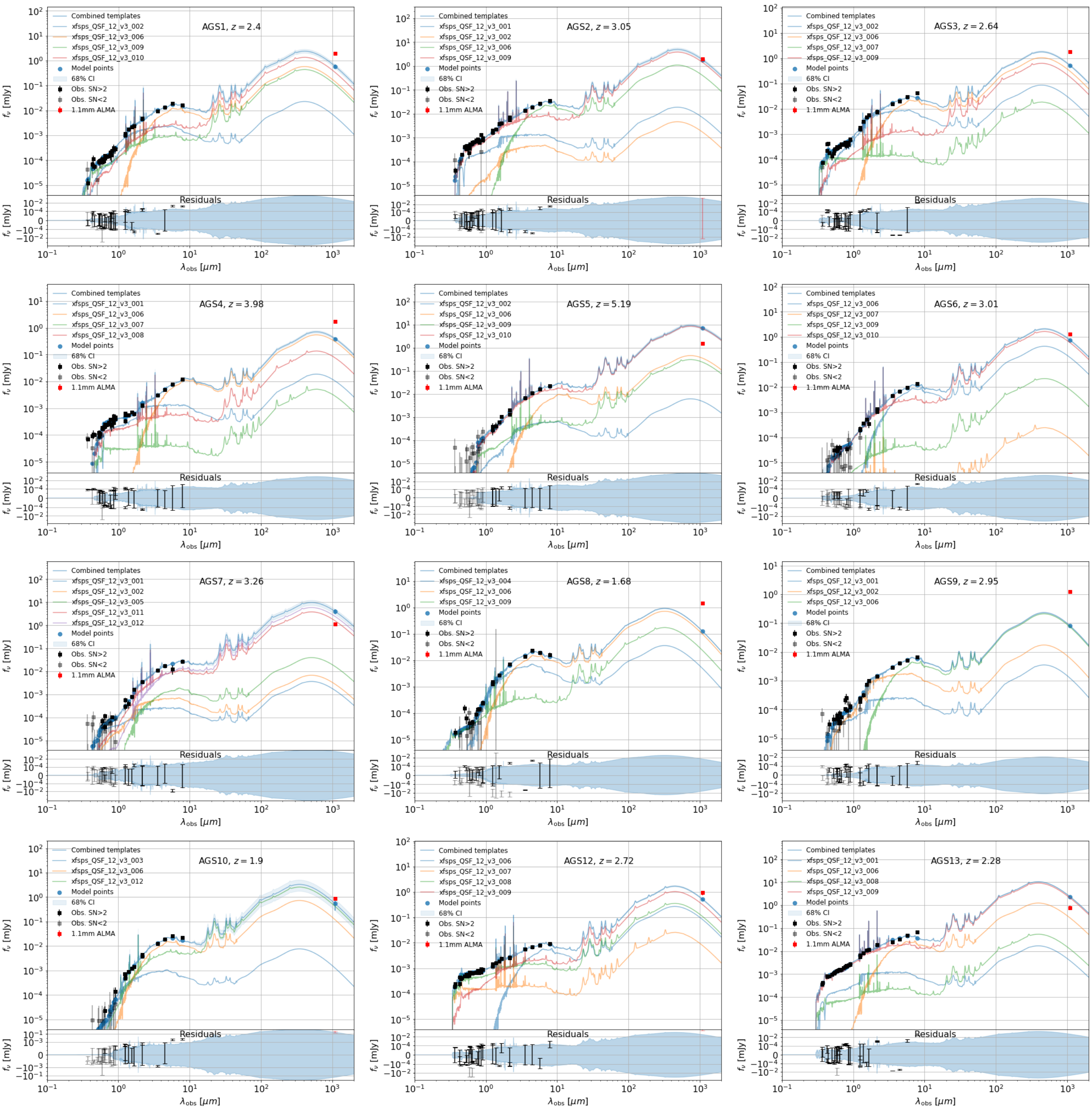
AGS1, $z = 2.4$
Combined templates
xfsps_QSF_12_v3_002
xfsps_QSF_12_v3_006
xfsps_QSF_12_v3_009
xfsps_QSF_12_v3_010
Model points
68% CI
Obs. SN>2
Obs. SN<2
1.1mm ALMA
Residuals
AGS2, $z = 3.05$
xfsps_QSF_12_v3_001
xfsps_QSF_12_v3_002
xfsps_QSF_12_v3_006
xfsps_QSF_12_v3_009
AGS3, $z = 2.64$
xfsps_QSF_12_v3_002
xfsps_QSF_12_v3_006
xfsps_QSF_12_v3_007
xfsps_QSF_12_v3_009
AGS4, $z = 3.98$
xfsps_QSF_12_v3_001
xfsps_QSF_12_v3_006
xfsps_QSF_12_v3_007
xfsps_QSF_12_v3_008
AGS5, $z = 5.19$
xfsps_QSF_12_v3_002
xfsps_QSF_12_v3_006
xfsps_QSF_12_v3_009
xfsps_QSF_12_v3_010
AGS6, $z = 3.01$
xfsps_QSF_12_v3_006
xfsps_QSF_12_v3_007
xfsps_QSF_12_v3_009
xfsps_QSF_12_v3_010
AGS7, $z = 3.26$
xfsps_QSF_12_v3_001
xfsps_QSF_12_v3_002
xfsps_QSF_12_v3_005
xfsps_QSF_12_v3_011
xfsps_QSF_12_v3_012
AGS8, $z = 1.68$
xfsps_QSF_12_v3_004
xfsps_QSF_12_v3_006
xfsps_QSF_12_v3_009
AGS9, $z = 2.95$
xfsps_QSF_12_v3_001
xfsps_QSF_12_v3_002
xfsps_QSF_12_v3_006
AGS10, $z = 1.9$
xfsps_QSF_12_v3_003
xfsps_QSF_12_v3_006
xfsps_QSF_12_v3_012
AGS12, $z = 2.72$
xfsps_QSF_12_v3_006
xfsps_QSF_12_v3_007
xfsps_QSF_12_v3_008
xfsps_QSF_12_v3_009
AGS13, $z = 2.28$
xfsps_QSF_12_v3_001
xfsps_QSF_12_v3_006
xfsps_QSF_12_v3_008
xfsps_QSF_12_v3_009
f_ν [mJy]
$\lambda_{\rm obs}$ [μm]

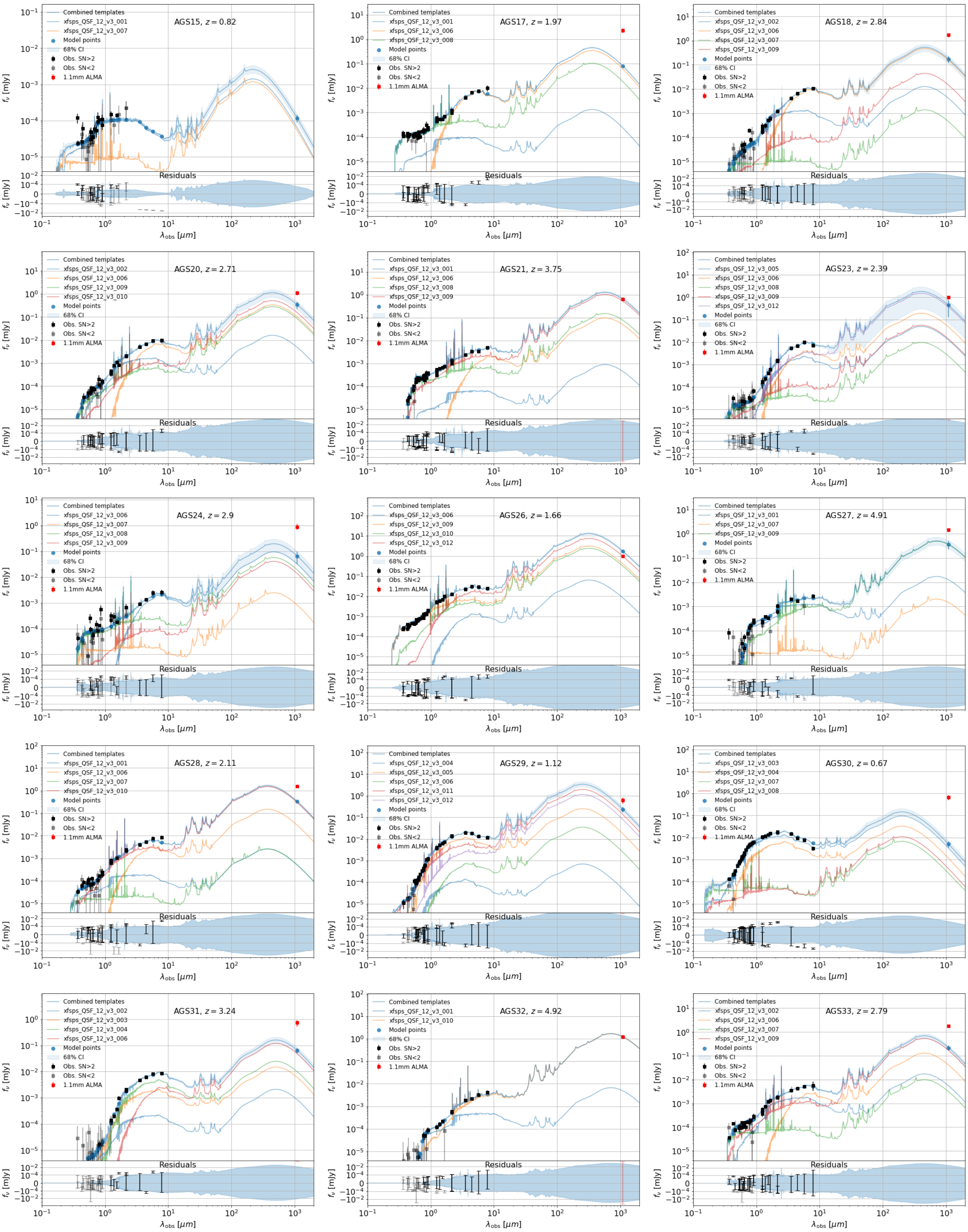

AGS15, $z = 0.82$
AGS17, $z = 1.97$
AGS18, $z = 2.84$
AGS20, $z = 2.71$
AGS21, $z = 3.75$
AGS23, $z = 2.39$
AGS24, $z = 2.9$
AGS26, $z = 1.66$
AGS27, $z = 4.91$
AGS28, $z = 2.11$
AGS29, $z = 1.12$
AGS30, $z = 0.67$
AGS31, $z = 3.24$
AGS32, $z = 4.92$
AGS33, $z = 2.79$
Combined templates
Model points
68% CI
Obs. SN>2
Obs. SN<2
1.1mm ALMA
Residuals
f_ν [mJy]
$\lambda_{\rm obs}$ [μm]

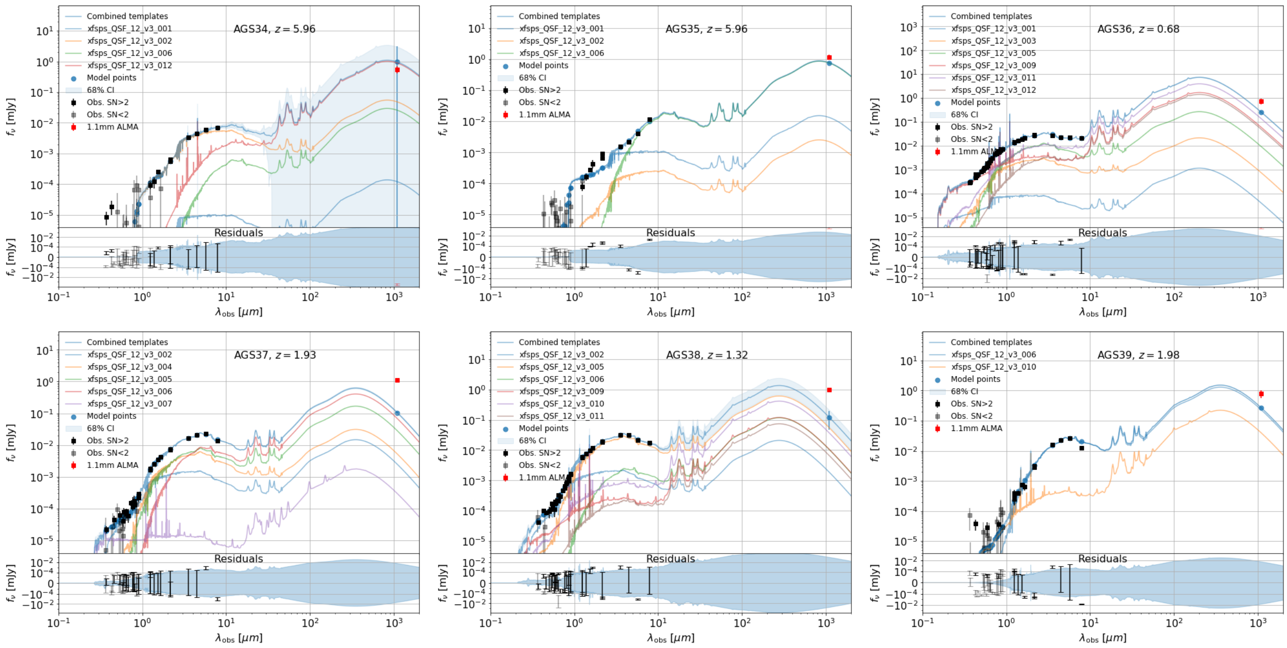

FIGURE 3.4: SEDs fit with the XFSPS-12O template set using UV-optical data only (excluding the 1.1mm ALMA point)

Comparing the model flux densities, Figure 3.5b, extracted from the resulting SED fits show that just 3/33 modelled ALMA detections (AGS2, AGS21, AGS32) are successfully predicting the 1.1mm flux as they lie within the 16th and 84th percentile confidence interval (also AGS34 although only due to an exaggerated upper and lower photo-z limit). For another 5/33 (AGS5, AGS7, AGS13, AGS26, AGS34*) the 1.1mm ALMA flux is overestimated by the fitted model. The flux of the remaining 25/33 galaxies is underestimated by the model at 1.1mm.

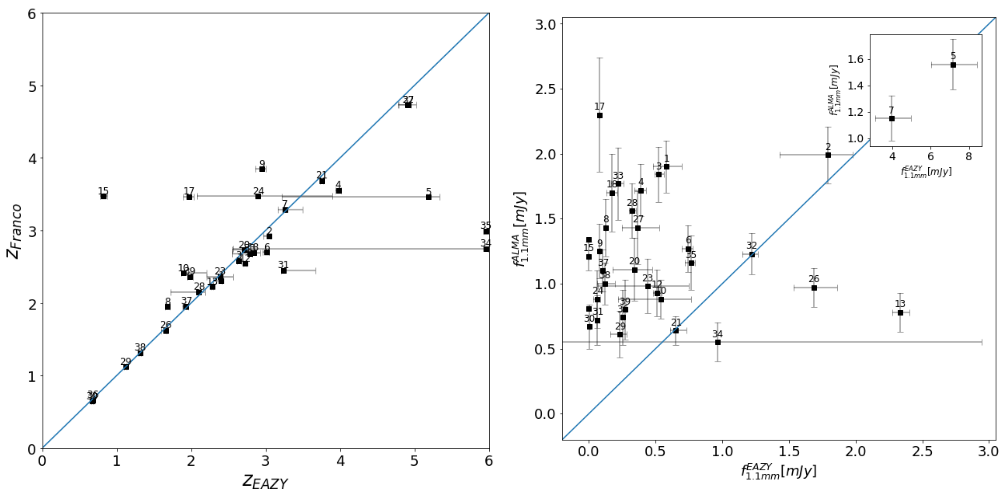

(A)

(B) 1.1mm EAZY and ALMA fluxes

FIGURE 3.5: 3.5a) Comparison of Franco et al. and EAZY redshifts from fitting UV-optical data only with the XFSPS-12O template set. 3.5b) Comparison of measured 1.1mm fluxes from Franco et al. and extracted from EAZY fitting UV-optical data only with the XFSPS-12O set.

Comparing the photometric redshifts determined by EAZY with the Franco et al. values, Figure 3.5a shows a nice trend along the $z_{Franco} = z_{EAZY}$ line. However, there are also cases where EAZY overestimates the redshift sending the source to the upper limit of the redshift grid, $z_{upper} = 6$, (AGS34, AGS35) or close to (AGS5). With an average $(z_{Franco}/z_{EAZY})_{\rm Avg} \approx 1.09$ several underestimations are also seen. Two of most severely underestimated EAZY photo-zs AGS15, ($z_{AGS15} = 0.82^{+0.06}_{-0.039}$) and AGS17 ($z_{AGS17} = 1.97^{+0.06}_{-0.08}$) also have 1.1mm fluxes off by orders of magnitude relative to the Franco et al. values. The outliers, AGS15 and 17, are among the so-called HST-dark galaxies (AGS4, 11, 15, 17, 24, 25) in the Franco et al. papers with no HST-WFC3 H-band (F160W 1.6μm) detection. These HST-dark galaxies may be close to another galaxy more luminous in the H-band, which can easily be confused as the optical counterpart for the ALMA source, due to outshining and obscuration of the real counterpart.

3.4.1 False associations and HST dark galaxies

As our catalogue contains 4 (AGS4, 15, 17, 24) of these HST-dark sources, they require an especially careful treatment to avoid false associations.

With the low redshift estimate of AGS15, $z_{AGS15} = 0.82^{+0.06}_{-0.039}$, and the fact that this estimate is well below the sample median, the crossmatched 3D-HST counterpart is regarded as a very likely false association, between the ALMA source and the 3D-HST catalogue.

For AGS17, Franco et al. 2018 [38] report a redshift of the closest neighbor associated with AGS17 $ID_{CANDELS}$ 4414 at $z_{AGS17} = 1.85$, and Skelton et al. 2014 [84] reports a redshift of $z_{AGS17} = 1.9772$ for the galaxy at AGS17, which is consistent with our EAZY photo-z estimate $z_{AGS17} = 1.97^{+0.06}_{-0.08}$. While not significantly offset from its counterpart Franco et al. 2018 [38] fit an SED to AGS17 counterpart $ID_{CANDELS}$ 4414 and obtain a FIR peak at $\sim 400\mu m$, which translates to an abnormally high SFR of $\sim 820 \pm 240 M_{\odot}\mathrm{yr}^{-1}$ at $z = 1.85$. However, such SFRs are not entirely impossible. As discussed in section 2.2, Fu et al. 2013 [23] found starbursts of $2000 M_{\odot} yr^{-1}$. However, the stellar mass obtained by Franco et al. 2018 [38] is an order of magnitude below the median stellar mass of their catalogue, and might therefore also be a false association. Due to this uncertainty in counterpart association and incomplete information about stellar mass and redshift, AGS15 and AGS17 are not taken into account in the follow-up work Franco et al. 2020 [40].

For AGS24 the photometric redshift estimated by EAZY $z_{AGS24} = 2.9$ does not directly point to a false association between the crossmatched 3D-HST counterpart and the ALMA source. Even though the estimated redshit is below the reported value by Franco et al., it is still a reasonable estimate given the sample median.

The last HST-dark galaxy, AGS4, has an EAZY redshift estimate of AGS4 ($z^{EAZY}_{AGS4} = 3.98^{+0.04}_{-0.04}$) which is close to, but below, the $z^{Franco}_{AGS4} = 4.32$ value reported by Franco et al.

2018[38]. Franco et al. 2018[38] note that the closest neighbor is $ID_{CANDELS}$ 8923, but several authors also detect another distant galaxy at the location of $ID_{CANDELS}$ 8923. Therefore Franco et al. 2018[38] use a deblending technique to separate the two sources to obtain low-z and high-z SEDs for the local galaxy $ID_{CANDELS}$ 8923 and the distant galaxy dubbed $ID_{CANDELS}$ 8923b. EAZY is then used to determine redshifts of $z_{8923} = 0.09^{+0.06}_{-0.07}$ and $z_{8923b} = 4.32^{+0.25}_{-0.21}$. The low-$z$ estimate is also obtained by Skelton et al. 2014[84] ($z_{8923} = 0.096$) for the 3D-HST catalogue (same catalogue as the one used in this study) using EAZY. How we can determine a redshift much closer to the Franco et al. value also using EAZY and without any deblending technique is presumably due to differences in the template set used and fit parameters adopted. Nevertheless, Franco et al. 2018[38] provides an explanation to argue that AGS4 is not associated with the low-z 8923 as this would mean an extraordinarily cold dust temperature with a FIR peak at 350μm, thus the counterpart to AGS4 must be the high-z galaxy 8923b.

With this breakdown of HST-dark galaxy redshifts in mind, we do note that there are also a handful of good EAZY redshift estimates in agreement with the reported Franco et al. values. On the other hand the majority of the modeled 1.1mm fluxes are underestimated by these fits inferring that we are unable to predict FIR SED given just constraints up to the 8μm IRAC band with the XFSPS-12O set. There may be several explanations to this skewed number of underestimations, e.g. we might be using a template set that is not representative of the sample. To test this hypothesis we tested the quality of the SED fit by including Spitzer and Herschel (MIPS 24μm, SPIRE 250/350/500μm, PACS 70/100/160μm) from Jin et al. 2018[85] (henceforth reffered to as the Super-deblended catalogue) to constrain the template combination at longer wavelengths.

By crossmatching right ascension and declination coordinates of the sample with the Super-deblended catalogue we found 22 matches separated by less than 1arcsec. Among the matches, two galaxies (AGS17 and AGS4) were manually excluded due to suspicions of false associations. This was based on inconsistencies with their Franco et al. redshifts and CANDELS redshifts in the Super-deblended catalogue. For AGS17 the Super-deblended catalogue reported a redshift $z^{CANDELS}_{AGS17} = 0.098$ while Franco et al. found $z^{Franco}_{AGS17} = 3.467$. For AGS4 $z^{CANDELS}_{AGS4} = 0.366$ in the Super-deblended catalogue and $z^{Franco}_{AGS4} = 3.556$. Thus 20/33 correctly crossmatched galaxies had their SEDs extended with Super-deblended catalogue data. The remaining 13/33 galaxies had no entries in the Super-deblended catalogue, so only 3D-HST catalogued data was used for these sources.

3.5 SED quality control and template optimization

Given these guiding constraints in the FIR, the modelled SEDs still showed difficulties at reproducing the FIR. Even subjects with Herschel and Spitzer data showed a shift in their

SED both horizontally and vertically from the data points as shown on the Figure 3.6 example (Appendix A Figure A.1 for all SEDs). E.g. the Herchel and Spitzer measurements were underestimated by the modeled SED.

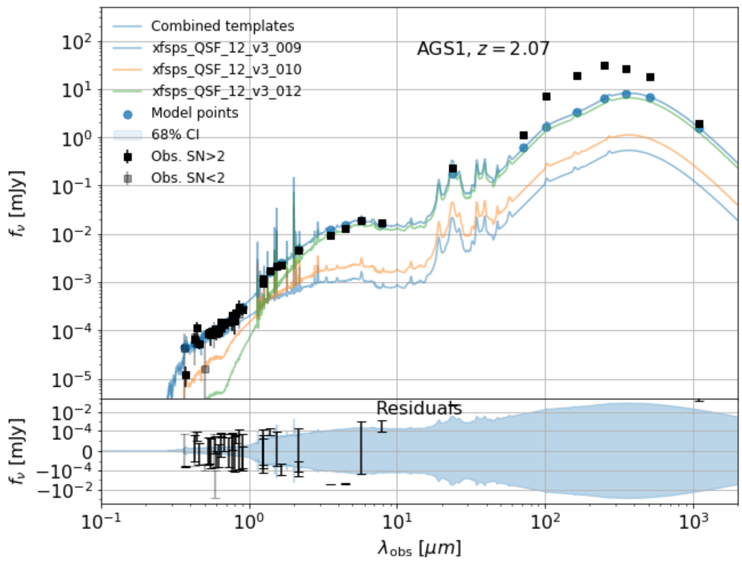

FIGURE 3.6: Showcase of the model underestimation of infrared fluxes offset from Herschel and Spitzer observations using the XFSPS-12O set (including IR data).

There may be several ways to explain this discrepancy between model and data.

First thought was trying to explain the offset with a simple scaling factor between the 3D-HST catalogue and the Super-deblended catalogue. As the nature of the offsets looked much like a simple vertical scaling problem. However, the Super-deblended catalogue did not include any IRAC channels etc. common to the 3D-HST catalogue making this comparison challenging. The last hint dismissing this scaling factor explanation was the fact that one galaxy, AGS13, which already fit relatively well would be offset by this scaling factor.

Second alternative solution explaining the bad fits came from the template set used to fit the SEDs. The templates used might not have been able to account for the dusty infrared emission in our catalogue of mostly ULIRGs. In UVJ-color space this means that either the templates *do not* sample the color space sufficiently to reproduce the color of the galaxies in our catalogue, or the templates *do* sample the color space sufficiently but their L_{IR}/L_V luminosity ratios are too low. The latter option was explored by generating a range of galaxy templates using Flexible Stellar Population Synthesis for Python (FSPS, Conroy, Gunn, and White 2009 [54], Conroy and Gunn 2010 [55]).

3.5.1 Flexible Stellar Population Synthesis for Python (FSPS)

A total of 1 million FSPS spectra were generated with the following parameters.

- The stellar population age was varied across 100 values from ~ 0.03 to ~ 13.80 Gyr.
- For the dust parameter 100 values were adopted ranging from 0.0 to 3.15. The dust value is the opacity at 5500Å, as defined in Equation 2.15, which is about the central wavelength of the V-band.
- The SFH e-folding time was varied across 100 values ranging from ~ 0.1 to ~ 2. The SFH model was set to a delayed τ-model of the form SFR $\sim t\exp(-t/\tau)$
- The dust type defining the attenuation curve of dust was set to the Calzetti et al. 2000 [26] model as described in section 2.2.
- Nebular line emission and continuum emission, based on Cloudy models from Byler et al. 2017 [86], was enabled.
- The IMF used was the Kroupa model (Equation 1.4) model as described in subsection 1.2.1 and Kroupa 2001 [8].

Upon generating the FSPS spectra all of them were convolved through the U- and V-filters (Apellániz 2006 [87]) and the 2MASS J-filter, all included in the default EAZY filter transmission file, to get their respective UVJ fluxes. Their U-V and V-J colors were determined as described in section 2.3, as was the colors of the input XFSPS-12O EAZY templates. Shown on Figure 3.7 is the entire FSPS generated sample and the XFSPS-12O templates on a U-V and V-J color-color diagram.

From Figure 3.7 it is clear that there exists a large subsample of galaxies with approximately the same color for each EAZY template. Within the ± 0.1 UVJ color box the luminosity ratios, L_{IR}/L_V, for each FSPS generated galaxy template was determined. The L_{IR} component of this luminosity ratio was determined by generating a template with the exact same parameters, but with dust emission turned off. The FSPS template without dust emission was then subtracted from the FSPS template with dust emission, and the difference was integrated to get the infrared luminosity.

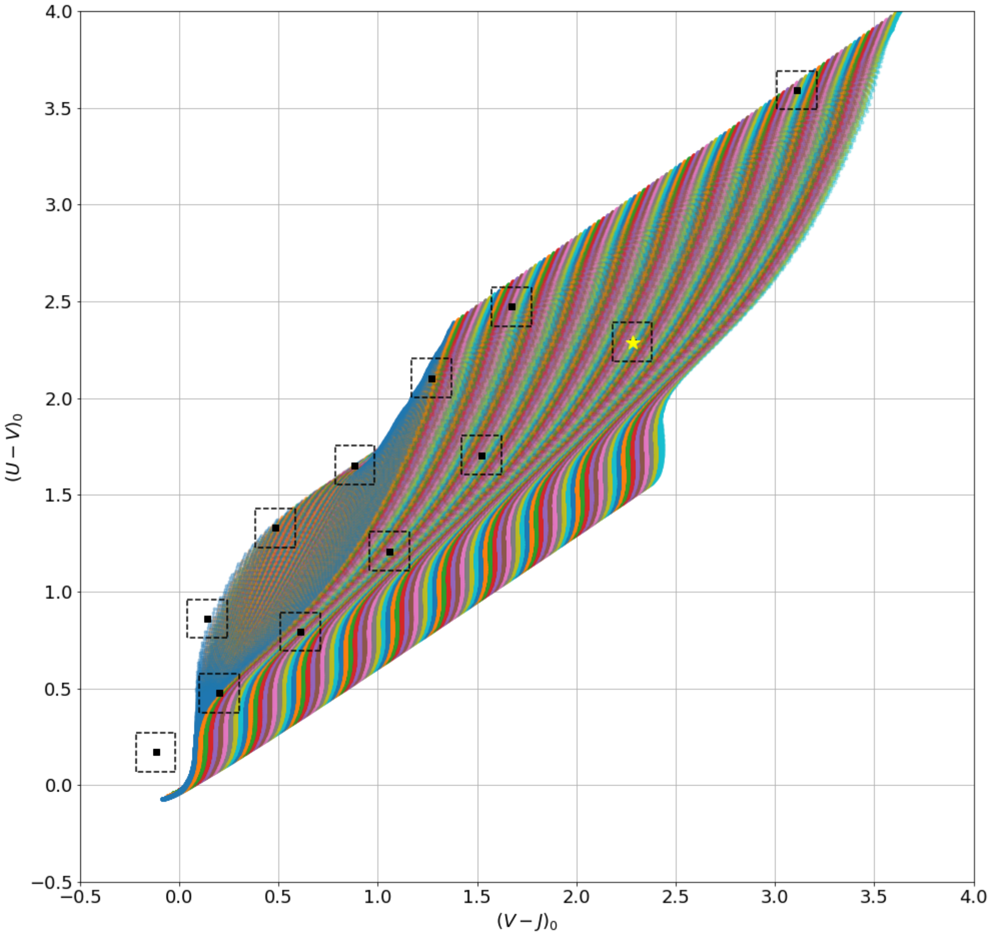

FIGURE 3.7: UVJ-color diagram of the FSPS generated galaxy spectra (colored points) and the XFSPS-12O templates (black squares). A ±0.1 box in U-V and V-J color has been drawn with a dashed black line around the templates to demonstrate the selection of galaxies close in color. We concentrate on the dusty template marked with a star, as this template ought to dominate the SED fits.

From Figure 3.7 it is also immediately evident that not all XFSPS-12O templates are fully sampled within their ±0.1 UVJ color boxes. But as we are mostly concerned with high redshift dusty galaxies, we direct our attention to the bottom angled row of input templates, more specifically the 12th template of the XFSPS-12O set marked with a yellow star, as this dusty template ought to dominate the dusty SED fits.

We examined the ±0.1 UVJ subsample within this 12th template of interest to ensure that no apparent errors were present. This check-up was visualized in a Corner plot, to reveal the covariances between each free parameter - respectively stellar population age, dust value, SFH e-folding time, and luminosity ratio.

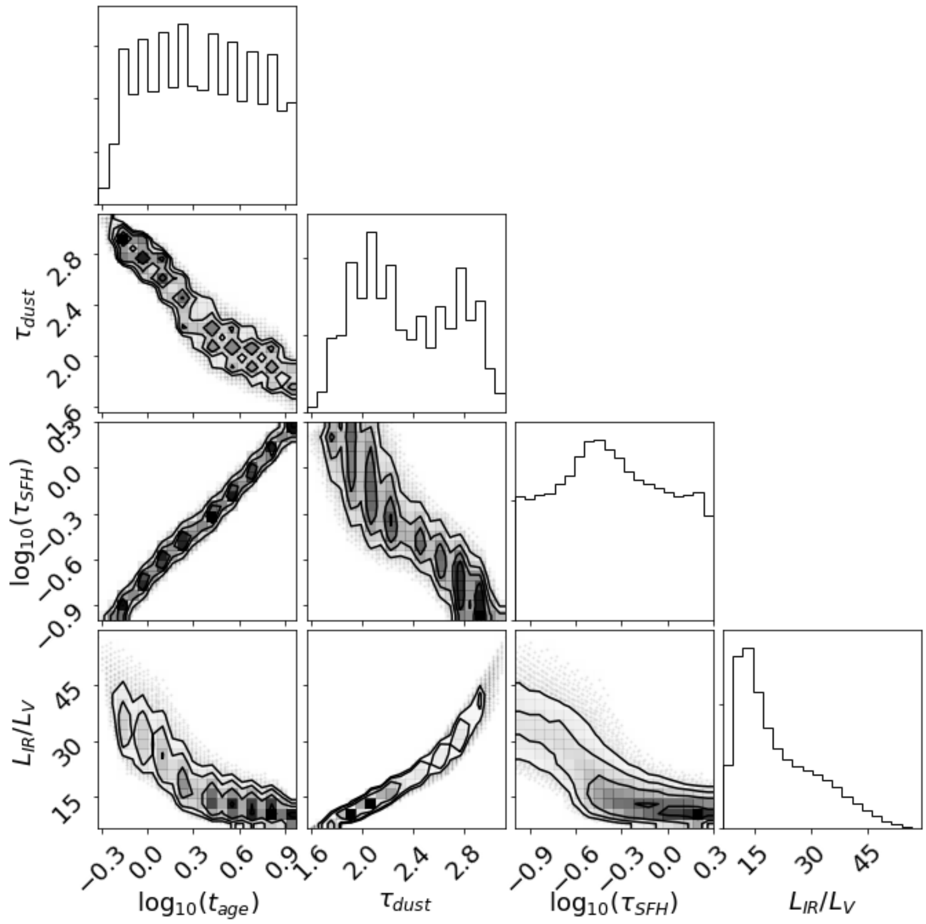

FIGURE 3.8: Visualization of covariances within each free parameter, namely stellar population age, dust value, SFH e-folding time, and luminosity ratio. Demonstrated here are the parameters of the FSPS generated galaxies within the ±0.1 UVJ box of template 12 subsample ($n = 4731$).

From Figure 3.8 we can deduce some simple relationships about the covariance of these parameters.

- The amount of dust is higher for younger galaxies. This is typically true as young galaxies with this color are forming new stars and have not had time to shed their dust.
- Younger galaxies have higher L_{IR}/L_V luminosity ratios which is consistent with the fact that these galaxies often contain more infrared emitting dust.
- Low values of SFH e-folding time produces dustier galaxies. A low τ_{SFH} leads to more rapid star formation, which is often correlated with dust production and accumulation.

With this kind of covariance evaluation one has to be careful with the interpretation of the histograms. These histograms should not be interpreted as true distributions for these free parameters, as they do not say much about the distribution but more about the sampling adopted.

Upon validating the covariances the generated template with the highest luminosity ratio ($L_{IR}/L_V \approx 60$) within the ± 0.1 UVJ box around the template of interest was picked out. This template was added to the template set to replace 12th template and the SED fits were performed again with this new template set, XFSPS-12M .

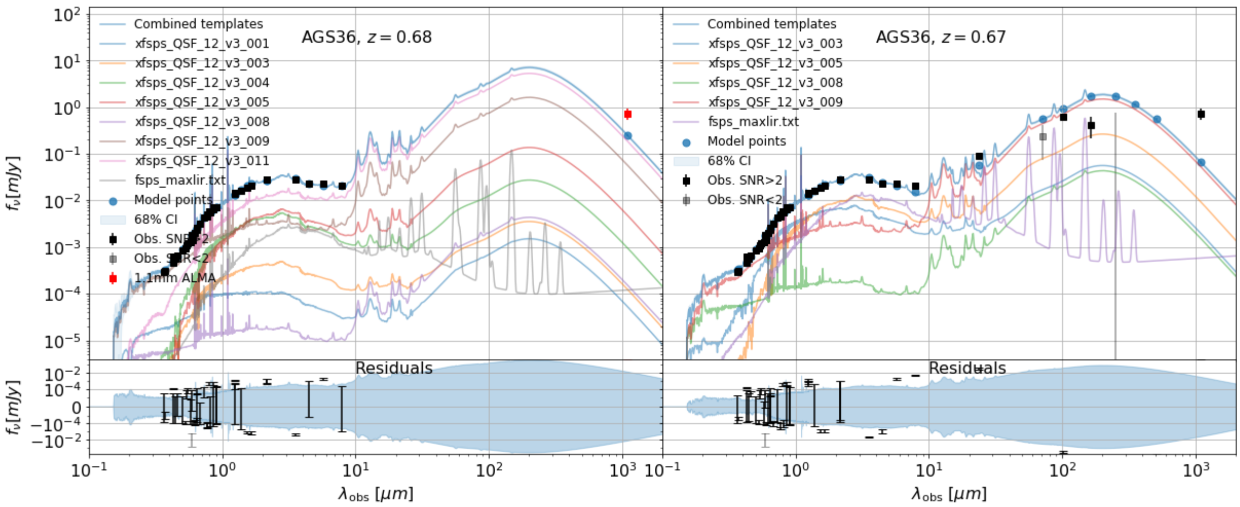

FIGURE 3.9: *(Left)* XFSPS-12M template fit excluding IR data. *(Right)* XFSPS-12M template fit including IR data.

The added maximum L_{IR}/L_V generated template was used in 11/33 fits. However, only 1/11 fits (AGS36 Figure 3.9) used the maximum L_{IR}/L_V template when fitting with IR data and without IR data. The rest of the 10/11 fits (Appendix A Figure A.8) only use the added maximum L_{IR}/L_V template when the IR data is not included, and then it is discarded again when IR data is included. Note that throughout this study, when stating that *IR data is included* etc. this means Super-deblended data (MIPS 24μm, PACS 70μm/100μm/160μm, SPIRE 250μm/350μm/500μm) *and* the 1.1mm ALMA data, with the exception of the synthetic photometry section IR data means up to the 500μm SPIRE.

Even in the 11/33 cases where the maximum L_{IR}/L_V template is used the fits with this XFSPS-12M set do not change notably compared to the fits with the XFSPS-12O set (Figure 3.4), and 10/11 fits using the maximum L_{IR}/L_V template still underestimate the 1.1mm flux when IR data is excluded. Generating FSPS templates with varying stellar population ages, dust opacities, and SFH e-folding times, and adding higher L_{IR}/L_V templates does not seem to solve the fit problems in the infrared where the Herschel, Spitzer, and ALMA fluxes are still underestimated.

3.5.2 Infrared templates

As the FSPS models could not account for the measured FIR fluxes we resorted to another set of 10 infrared dust models by Magdis et al. 2012 [88]. These templates are based on the dust models by Draine and Li 2007 [89], which assumes the dust population to be a mixture of carbonaceous and amorphous silicate grains. Additionally, the dust population is split into two components in terms of the heating mechanism. The first component comprises the majority of the dust population and is present in the diffuse ISM where it is heated by the interstellar radiation field, with a constant intensity U_{min}. The smaller fraction, γ, consists of dust in environments where the interstellar radiation field is more intense such as photodissociation regions, with intensities ranging from U_{min} to U_{max}. Nine of the ten Magdis et al. 2012 [88] templates each represent a redshift range, while the last template is a starburst template universal for all redshifts.

- IR template 1: $z = 0 - 0.025$.
- IR template 2: $z = 0.05 - 0.275$.
- IR template 3: $z = 0.3 - 0.6250$.
- IR template 4: $z = 0.65 - 0.975$.
- IR template 5: $z = 1.0 - 1.30$.
- IR template 6: $z = 1.325 - 1.725$.
- IR template 7: $z = 1.75 - 2.25$.
- IR template 8: $z = 2.27 - 3.0$.
- IR template 9: $z > 3.0$.
- IR template 10: Universal starburst.

These 10 infrared templates were used in addition to the XFSPS-12O set but where dust emission of the XFSPS-12O had been turned off to ensure the 10 IR templates were used to fit the infrared. In contrast to the XFSPS-12O templates, which are defined from $9.1nm$ to $1cm$, the 10 infrared templates are only defined in the $1\mu m$ to $1cm$ regime. While reproducing the FIR SEDs more accurately when fit with UV-optical and IR data, this set was prone to extrapolation errors as illustrated on Figure 3.10 (and the rest of the sample Appendix A Figure A.8). This caused artificially high model values when EAZY tried to automatically extrapolate the infrared templates to shorter wavelengths $< 1\mu m$ where they were not initially defined

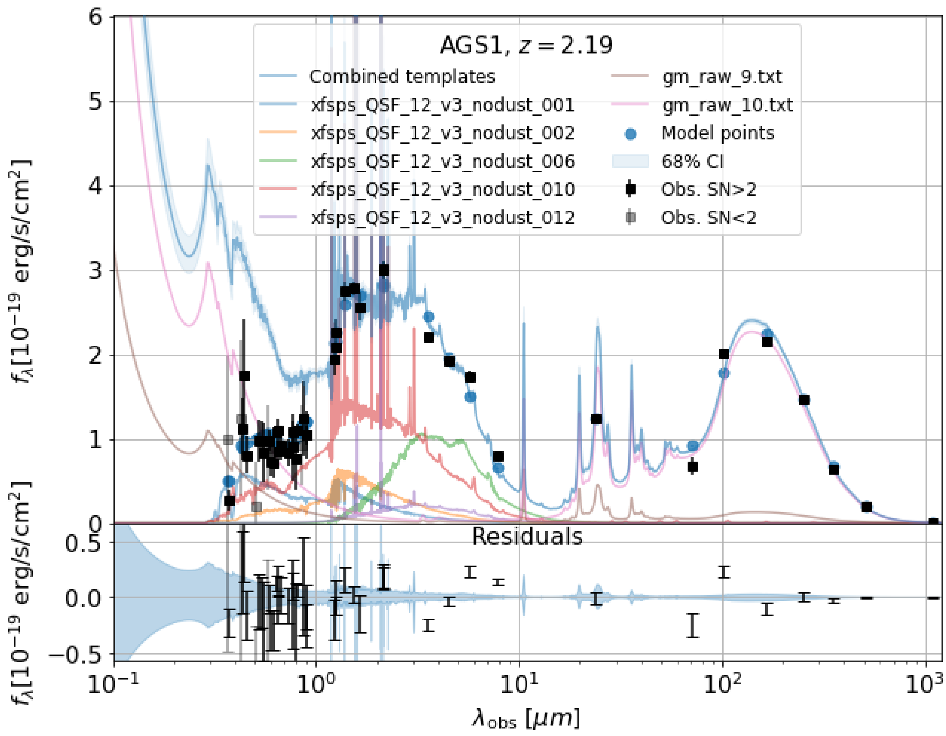

FIGURE 3.10: SED fits including IR data using XFSPS-1210R including the infrared Magdis et al. 2012 [88] templates. The fits in the IR are clearly improved compared to fits with the XFSPS-12O.

As a countermeasure a range of different extrapolation methods were tested $< 1\mu m$ to correct this extrapolation error. The extrapolation and truncation schemes explored are discussed in detail in Appendix A section A.3. The final set of templates devised following considerations regarding infrared luminosity and energy absorbed, along with minimization of the IRAC band deviation was the XFSPS-1210PAH template set. With the XFSPS-1210PAH, the SED fits were able to reproduce the FIR SED for the majority of the sample when IR data was included, Figure 3.11.

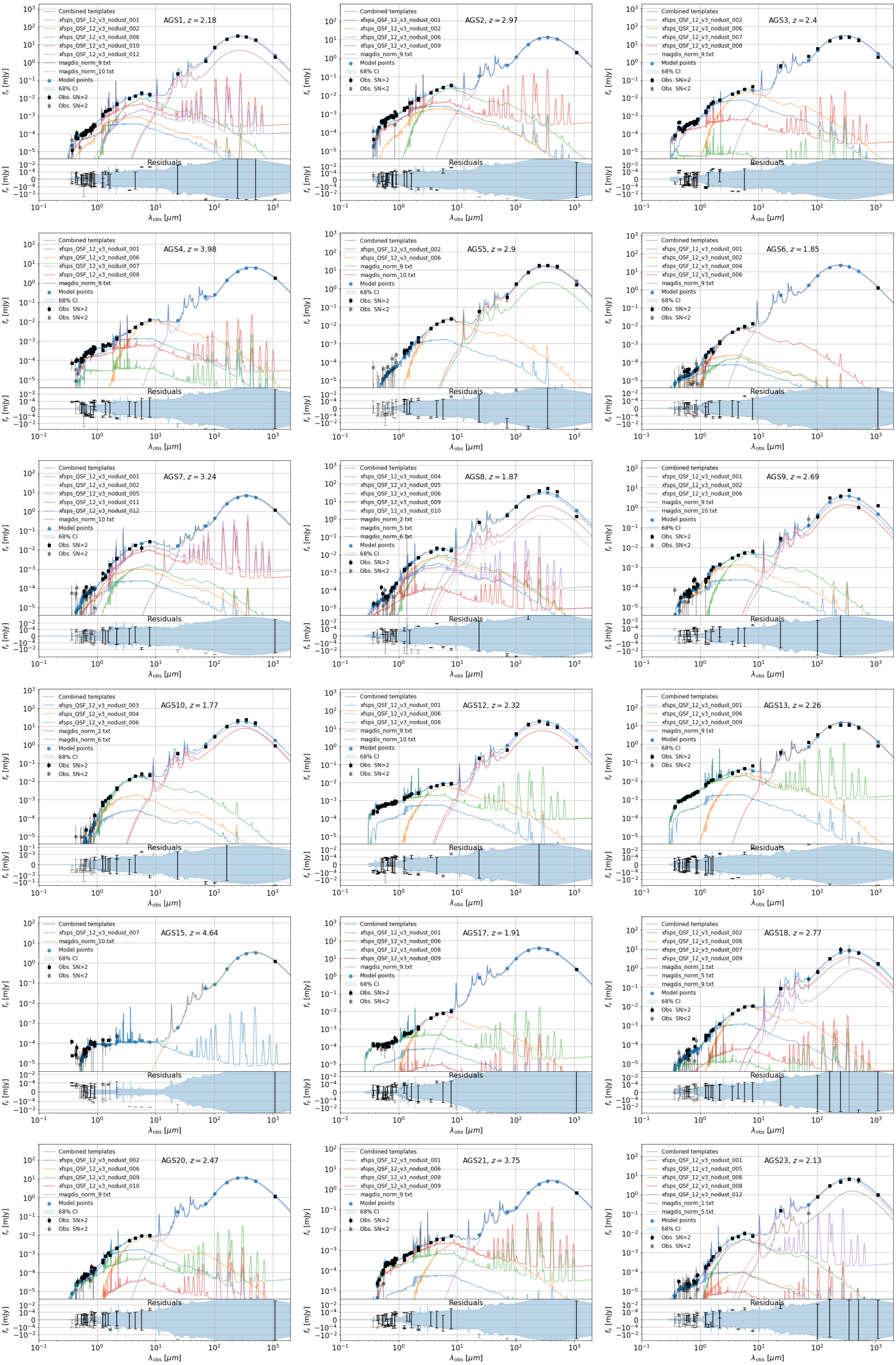
AGS1, $z = 2.18$
AGS2, $z = 2.97$
AGS3, $z = 2.4$
AGS4, $z = 3.98$
AGS5, $z = 2.9$
AGS6, $z = 1.85$
AGS7, $z = 3.24$
AGS8, $z = 1.87$
AGS9, $z = 2.69$
AGS10, $z = 1.77$
AGS12, $z = 2.32$
AGS13, $z = 2.26$
AGS15, $z = 4.64$
AGS17, $z = 1.91$
AGS18, $z = 2.77$
AGS20, $z = 2.47$
AGS21, $z = 3.75$
AGS23, $z = 2.13$
Residuals
f_ν [mJy]
λ_{obs} [μm]

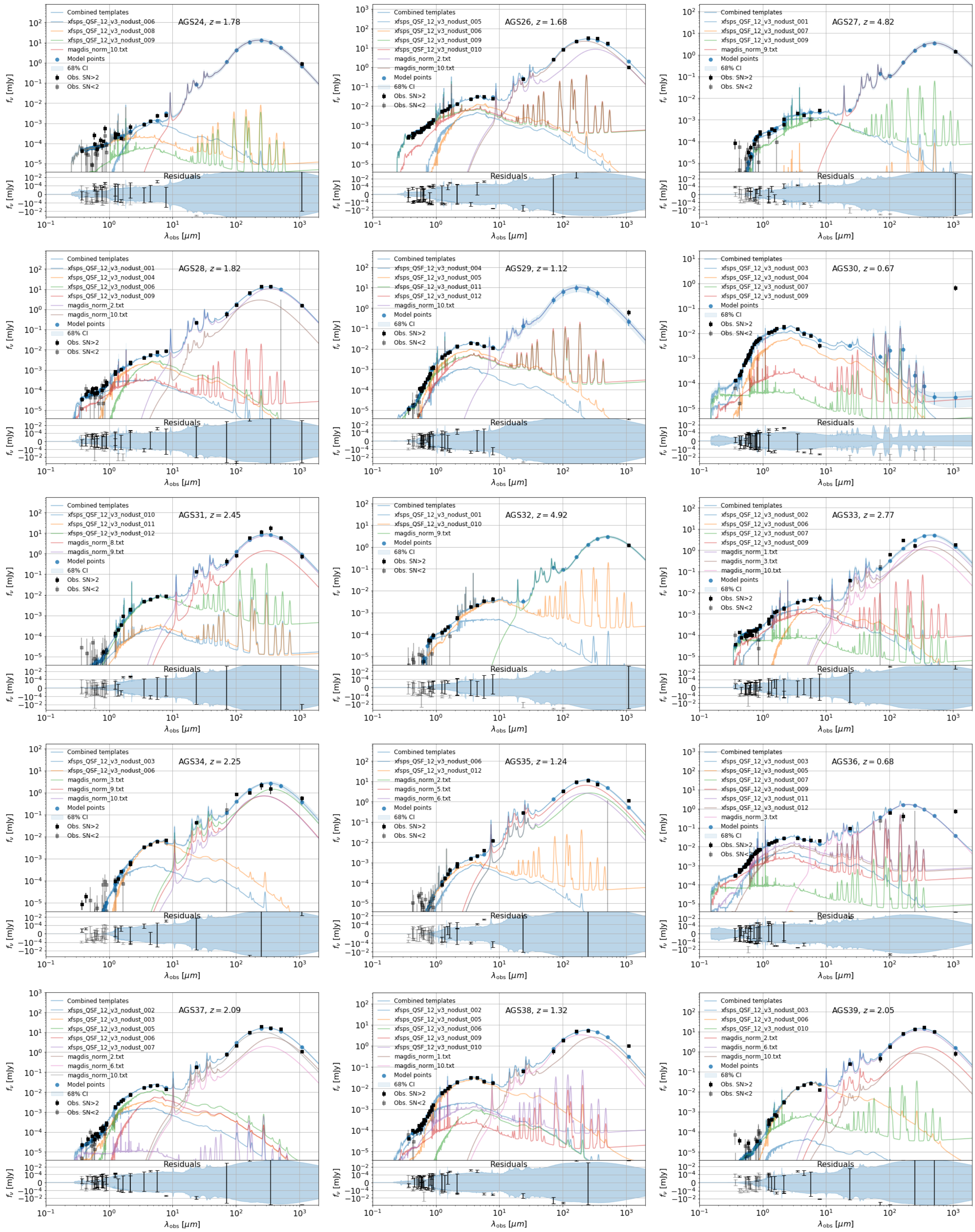

FIGURE 3.11: SEDs fit with the XFSPS-1210PAH template set including Super-deblended and 1.1mm ALMA infrared data.

The high quality of the SEDs is also reflected by the photometric redshift estimates which are in overall agreement with the redshift reported by Franco et al. (Figure 3.12a). Additionally, Figure 3.12b show the majority of 1.1mm model fluxes are reproduced within a factor of 2 of the ALMA measured flux.

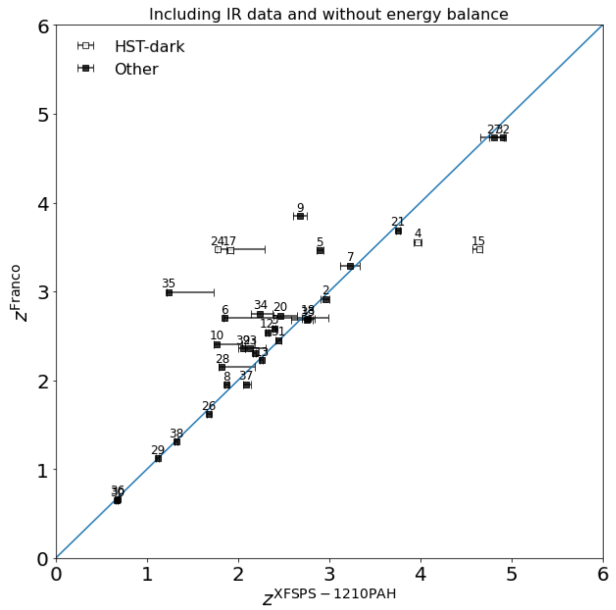

(A)

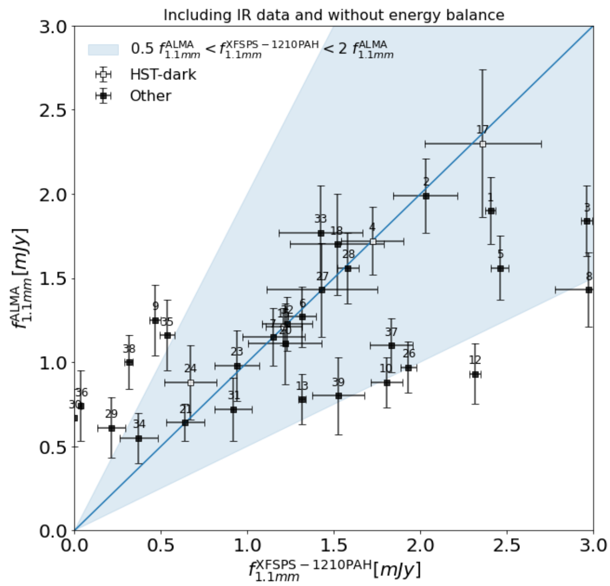

(B)

FIGURE 3.12: 3.12a) Comparison of the Franco et al. redshifts and EAZY redshifts from the XFSPS-1210PAH fits including infrared data. 3.12b) Comparison of the measured ALMA fluxes and the modelled 1.1mm fluxes from the fits with the XFSPS-1210PAH template set including IR data.

The problem with using the IR templates at optical wavelengths is that they are used at the expense of dustier stellar FSPS templates as can be seen on the SEDs produced Figure 3.11 where the IR templates (labelled *magdis_norm_ ... .txt*) spills into the 8μm and 5.8μm IRAC channels 3 and 4. This unphysical weighing of the IR template at optical wavelengths means that the energy absorbed decreases such that there no longer is an almost one-to-one relationship between the infrared luminosity, L_{IR} , and energy absorbed. Furthermore, the infrared templates themselves are not energy balanced as the fitted PAH component has merely been attached to the FIR component with no scaling to ensure any relationship between the energy absorbed and the infrared luminosity. In other words, even though the XFSPS-1210PAH set provides almost flawless SED fits for the sample, the energy balance is broken when using the IR templates.

3.5.3 Energy Balance

Ideally, we would like to have a template set that can produce good fits to the data and still be energy balanced. Imposing this criteria of energy balance, we have to look for another template set which is representative our sample of dusty galaxies. However, we can still use the XFSPS-1210PAH set as a reference to how the fits should ideally look and what kind of L_{IR} values we should expect. Using EAZY, Gabriel Brammer generated a new set of 12 templates including 10 XFSPS templates and 2 starbursting galaxies to represent possible extreme cases within our sample. The infrared regime of the 10 XFSPS templates were replaced by Magdis et al. 2012 [88] template #9 which was scaled to the energy absorbed value to ensure energy balance. This energy absorbed is determined by calculating the Calzetti model for the given τ_{dust}, which is then applied to the SED, and the energy absorbed is then the difference in the integrated energy of the attenuated and unattenuated SED. In the following this set of templates is dubbed the XFSPS-12SB. Figure 3.13 shows comparisons of L_{IR} values and SED fits with the XFSPS-1210PAH (left subplots of each pair) and with the XFSPS-12SB (right subplots of each pair).

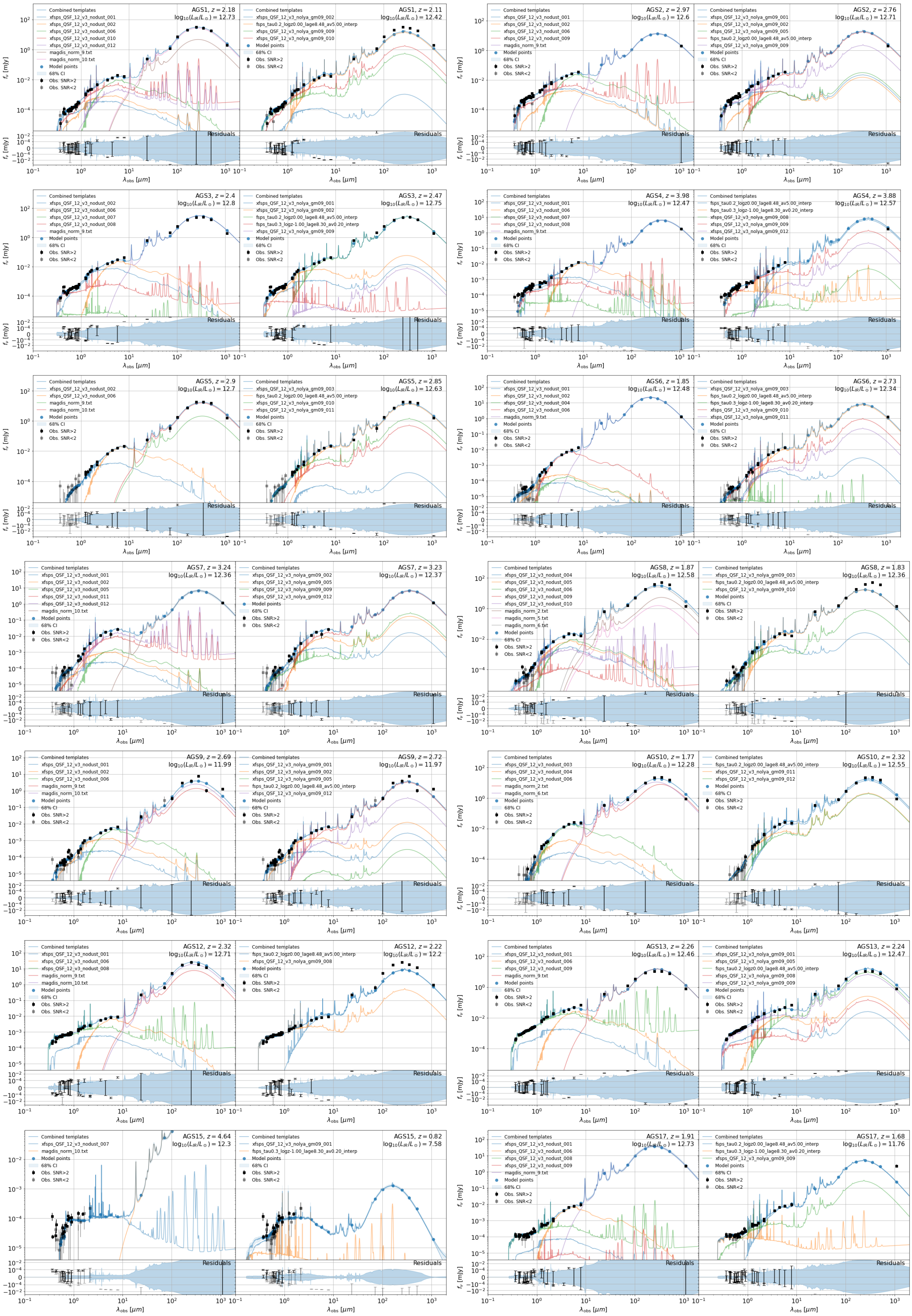
AGS1, $z = 2.18$ $\log_{10}(L_{IR}/L_\odot) = 12.73$
AGS1, $z = 2.11$ $\log_{10}(L_{IR}/L_\odot) = 12.42$
AGS2, $z = 2.97$ $\log_{10}(L_{IR}/L_\odot) = 12.6$
AGS2, $z = 2.76$ $\log_{10}(L_{IR}/L_\odot) = 12.71$
AGS3, $z = 2.4$ $\log_{10}(L_{IR}/L_\odot) = 12.8$
AGS3, $z = 2.47$ $\log_{10}(L_{IR}/L_\odot) = 12.75$
AGS4, $z = 3.98$ $\log_{10}(L_{IR}/L_\odot) = 12.47$
AGS4, $z = 3.88$ $\log_{10}(L_{IR}/L_\odot) = 12.57$
AGS5, $z = 2.9$ $\log_{10}(L_{IR}/L_\odot) = 12.7$
AGS5, $z = 2.85$ $\log_{10}(L_{IR}/L_\odot) = 12.63$
AGS6, $z = 1.85$ $\log_{10}(L_{IR}/L_\odot) = 12.48$
AGS6, $z = 2.73$ $\log_{10}(L_{IR}/L_\odot) = 12.34$
AGS7, $z = 3.24$ $\log_{10}(L_{IR}/L_\odot) = 12.36$
AGS7, $z = 3.23$ $\log_{10}(L_{IR}/L_\odot) = 12.37$
AGS8, $z = 1.87$ $\log_{10}(L_{IR}/L_\odot) = 12.58$
AGS8, $z = 1.83$ $\log_{10}(L_{IR}/L_\odot) = 12.36$
AGS9, $z = 2.69$ $\log_{10}(L_{IR}/L_\odot) = 11.99$
AGS9, $z = 2.72$ $\log_{10}(L_{IR}/L_\odot) = 11.97$
AGS10, $z = 1.77$ $\log_{10}(L_{IR}/L_\odot) = 12.28$
AGS10, $z = 2.32$ $\log_{10}(L_{IR}/L_\odot) = 12.55$
AGS12, $z = 2.32$ $\log_{10}(L_{IR}/L_\odot) = 12.71$
AGS12, $z = 2.22$ $\log_{10}(L_{IR}/L_\odot) = 12.2$
AGS13, $z = 2.26$ $\log_{10}(L_{IR}/L_\odot) = 12.46$
AGS13, $z = 2.24$ $\log_{10}(L_{IR}/L_\odot) = 12.47$
AGS15, $z = 4.64$ $\log_{10}(L_{IR}/L_\odot) = 12.3$
AGS15, $z = 0.82$ $\log_{10}(L_{IR}/L_\odot) = 7.58$
AGS17, $z = 1.91$ $\log_{10}(L_{IR}/L_\odot) = 12.73$
AGS17, $z = 1.68$ $\log_{10}(L_{IR}/L_\odot) = 11.76$
Residuals
f_ν [mJy]
λ_{obs} [μm]

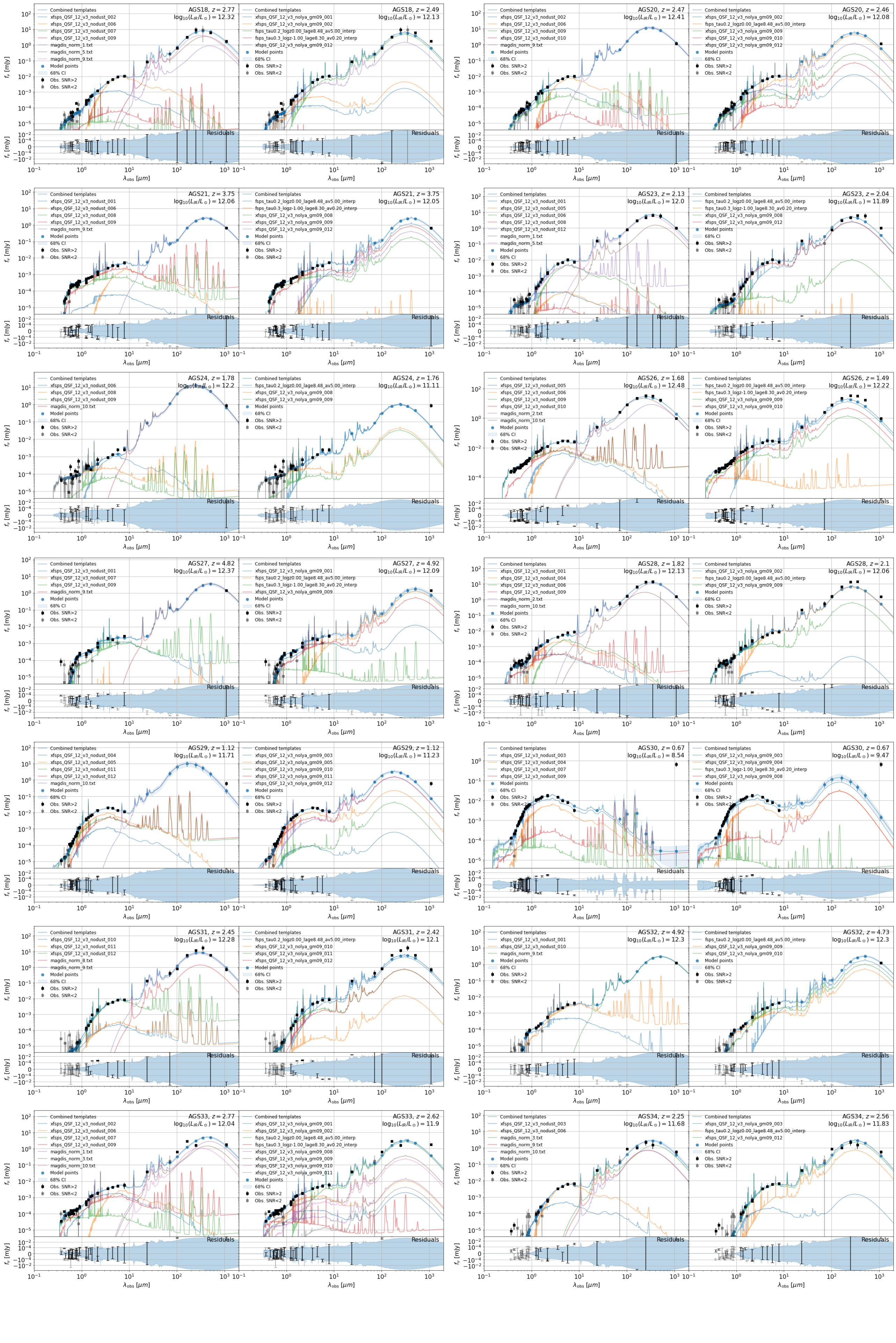

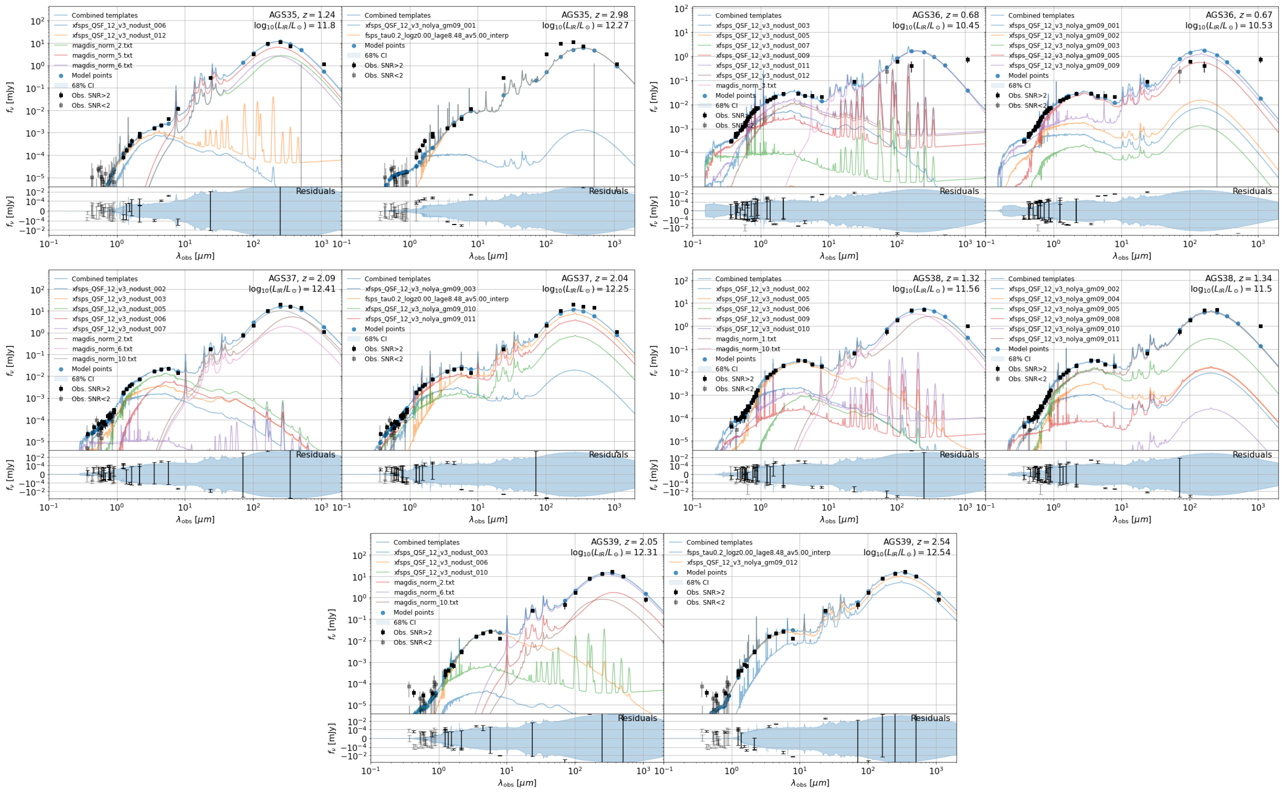

FIGURE 3.13: Side-by-side SED fits including IR data (Super-deblended and 1.1mm ALMA) with the left fit of each pair being with the XFSPS-1210PAH set and the right fit of each pair being with the XFSPS-12SB template set.

The new XFSPS-12SB set provides good fits with a quality comparable to that of the XFSPS-1210PAH, when FIR data is included and only with a few exceptions. The new fits do however deviate slightly in terms of infrared luminosity (Equation 2.11) and 1.1mm flux, where the XFSPS-12SB generally produce lower values.

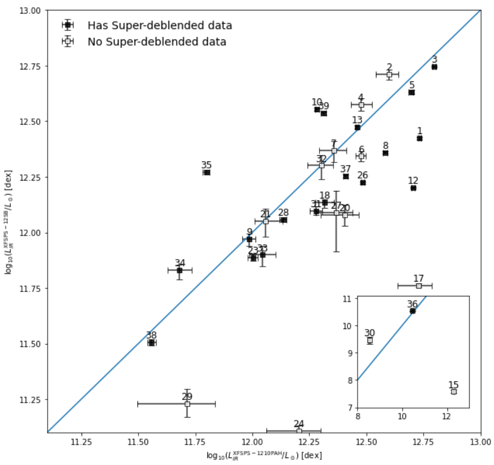

(A)

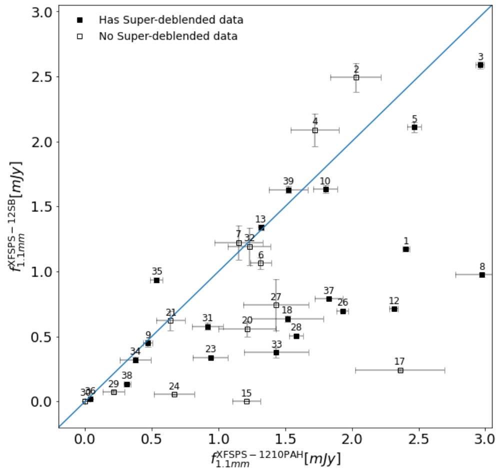

(B)

FIGURE 3.14: 3.14a) Comparison of IR luminosities from the XFSPS-12SB and XFSPS-1210PAH fits including IR data. The inset plot shows a subset of outliers. 3.14b) Comparison of the model 1.1mm fluxes from fits with the XFSPS-12SB and XFSPS-1210PAH set including IR data.

While the L_{IR} and 1.1mm fluxes are slightly off, the XFSPS-12SB performs much better in terms of L_{IR}/energy_abs which is down to a simple factor (median $\sim$ 2.9), compared to an order of magnitude (median $\sim$ 14.7) with the XFSPS-1210PAH. Similar to the XFSPS-1210PAH set the photometric redshift estimates from the XFSPS-12SB set are also in agreement with the Franco et al. reported redshifts.

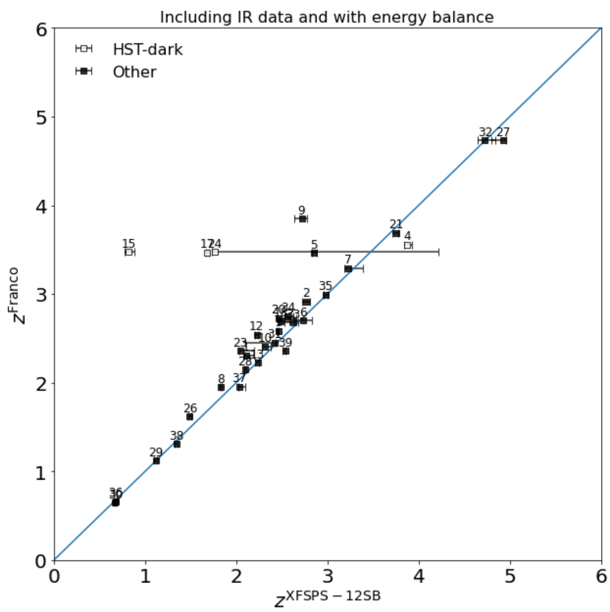

(A)

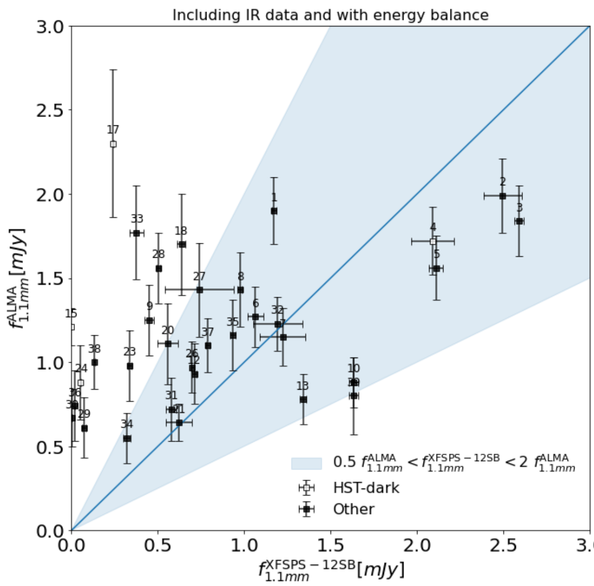

(B)

FIGURE 3.15: 3.15a) Comparison of the Franco et al. redshifts and EAZY redshifts from the XFSPS-12SB fits including infrared data. 3.15b) Comparison of the measured ALMA fluxes and the modelled 1.1mm fluxes from the fits with the XFSPS-12SB template set including IR data.

While a portion of the 1.1mm modeled fluxes are underestimated compared to the ALMA flux, a large fraction of 1.1mm modeled fluxes are still in agreement with the ALMA fluxes within a factor of 2. This is a significant improvement from the original XFSPS-12O set imposing energy balance where the FIR SED was systematically underestimated even when Super-deblended data was included.

3.6 Chapter summary

Initially fitting the catalogue containing 3D-HST data up to the $8\mu m$ IRAC channel 4, with the default XFSPS-12O template showed a significant underprediction of the FIR SED and the 1.1mm flux values. Upon trying to improve the SED fits, Super-deblended catalogue data (MIPS $24\mu m$, PACS $70\mu m/100\mu m/160\mu m$, SPIRE $250\mu m/350\mu m/500\mu m$) was included for cross-matched sources. For the 20 sources with cross-matched Super-deblended data, the FIR SED still seemed to be systematically underestimated when fitting with the XFSPS-12O.

An attempt was made to solve this problem by generating 1 million galaxy templates with FSPS with varying stellar population ages, dust opacities, and SFH e-folding times. We then sought to replace the most used dusty template #12 of the XFSPS-12O set with the FSPS template from the generated sample which had the highest L_{IR}/L_V ratio but approximately same UVJ color. This new XFSPS-12M set was then used to fit the data, but fits showed little to no usage of the replacement template, and therefore also no real improvement to the SED fits compared to the XFSPS-12O set.

As no improvement was found with the FSPS generated templates, a different approach was taken to add 10 IR templates from Magdis et al. 2012 [88] which could be used in the FIR. Following extrapolation and truncation methods explored in Appendix A section A.3, this XFSPS-1210PAH set produced high quality FIR fits, but suffered from the lack of energy balance, which was initially desired.

To impose energy balance another template set including two starbursting templates was devised (XFSPS-12SB). Including FIR data, the XFSPS-12SB set produced high quality fits in many cases comparable to the XFSPS-1210PAH fits (Figure 3.13), while still imposing energy balance.

The key take-aways from this exercise are the following.

- We have developed two template sets; One imposing energy balance (XFSPS-12SB) and one not imposing energy balance (XFSPS-1210PAH).
- Both template sets are able to reproduce photometric redshifts in agreement with the Franco et al. values when IR data is included.

One may keep meticulously optimizing the template set to improve the SED fits, however in the end we may be limited by the individual morphology of each galaxy as will be elaborated further on in the coming chapter.

Chapter 4

Results

Having developed a set of SPS models that can produce good fits to the DSFG SEDs of the 33 galaxies of the GOODS-ALMA test sample, we turn to the real test we set out to do in this section. Namely, evaluating the constraint of energy balance when only fitting UV-optical data. To execute this test we need to take a closer look on the morphology of the galaxies in the sample.

At the end of this section we will produce synthetic maps covering the same region as the 69arcmin^2 1.1mm GOODS-ALMA map using the optimized SPS models of the XFSPS-12SB set to test the robustness of the energy balance constraint.

4.1 Galaxy structure and morphology

We start off by investigating the structure and morphology of each AGS galaxy and how it may affect the SED fitting. From the provided photometric GOODS-ALMA mosaic map (Gómez-Guijarro et al. in prep) we compute the histogram by binning the data using the Freedman Diaconis Estimator, and determine the RMS sensitivity ($\sigma \simeq 0.085$mJy/beam) by fitting a gaussian to the histogram pixel distribution (Figure 4.1).

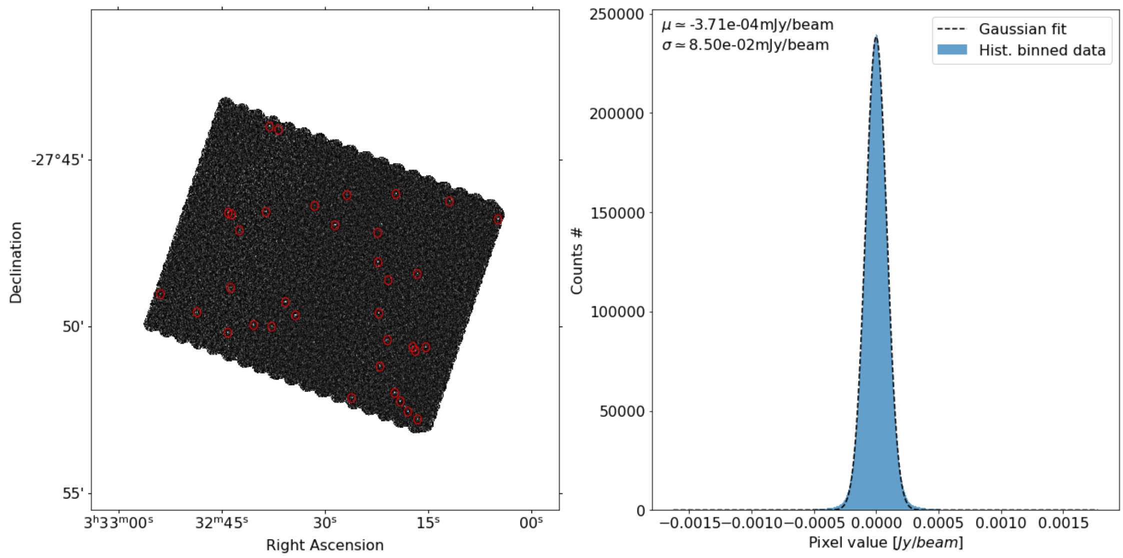

FIGURE 4.1: *Left*) The Franco et al. GOODS-ALMA map with the position of the AGS highlighted by 8arcsec circles. *Right*) The binned pixel distrubution of the GOODS-ALMA map along with the best fit gaussian.

With the GOODS-ALMA mosaic and photometric F160W 3D-HST data we can closely inspect each individual galaxy in close-up cutouts of $1.8'' \times 1.8''$. The right subplot of Figure 4.2 shows the first cutout of the raw archive F160W 3D-HST mosaic. A very distinct offset between the ALMA contours and the 3D-HST counterpart is clearly visible, and multiple AGS sources showed a similar offset. This suspicious systematic offset had us doubting the robustness of the astrometry of the 3D-HST data and F160W mosaic. Franco et al. 2020 [39] describe a similar global systematic offset of $\Delta\text{RA} = -96 \pm 83$mas and $\Delta\text{Dec} = 252 \pm 107$mas derived from 375 HST v2.0 sources common to the Panoramic Survey Telescope and Rapid Response System (Pan-STARRS) Data Release 2 (Flewelling et al. 2016 [90]). Along with this global correction they derive an additional local calibration error varying with position (largest at the mosaic edges) which was introduced when the HST v2.0 mosaic was built.

With this correction in mind we reviewed the astrometry of the mosaics. Gabriel Brammer found a non-negligible global offset between the 3D-HST mosaics and the GOODS-ALMA astrometric frame and aligned the 3D-HST mosaics to the Pan-STARRS/GAIA frame as was done by Franco et al. 2020 [39] with the HST v2.0 mosaic. The cutout following this astrometric correction is illustrated on the left subplot of Figure 4.2 and shows a significant improvement in the alignment of sources.

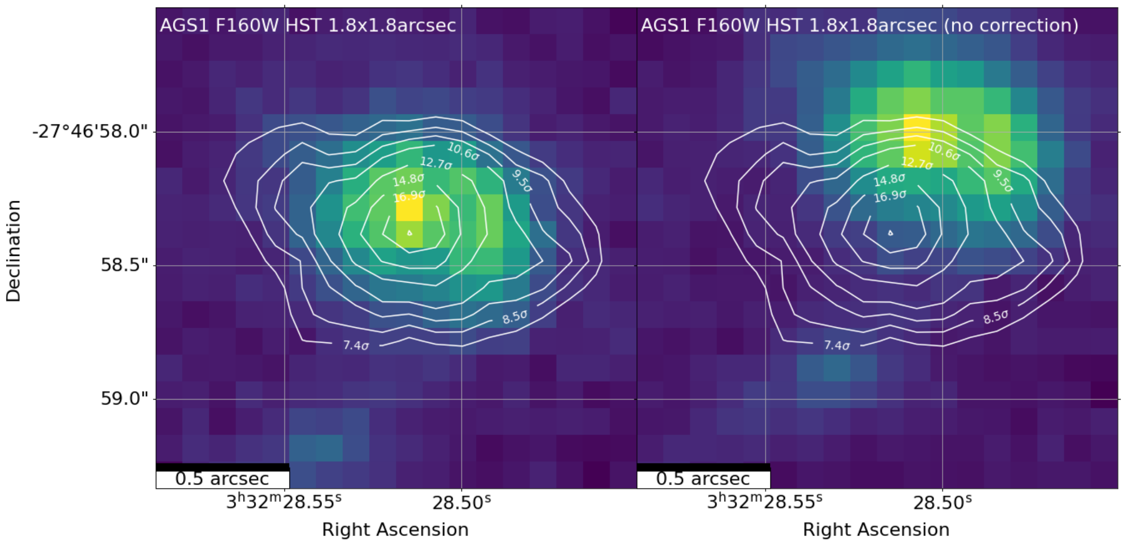

FIGURE 4.2: *Left*) Example F160W cutout of galaxy with associated ALMA contours after astrometric correction. *Right*) The same galaxy with its associated ALMA contours before astrometric correction.

Having corrected the 3D-HST mosaics we examined the morphology of each galaxy by creating improved aligned cutouts of 1.8″ × 1.8″ and larger 10″ × 10″ centered on the GOODS-ALMA position reported by Franco et al. 2020 [40], Figure 4.3.

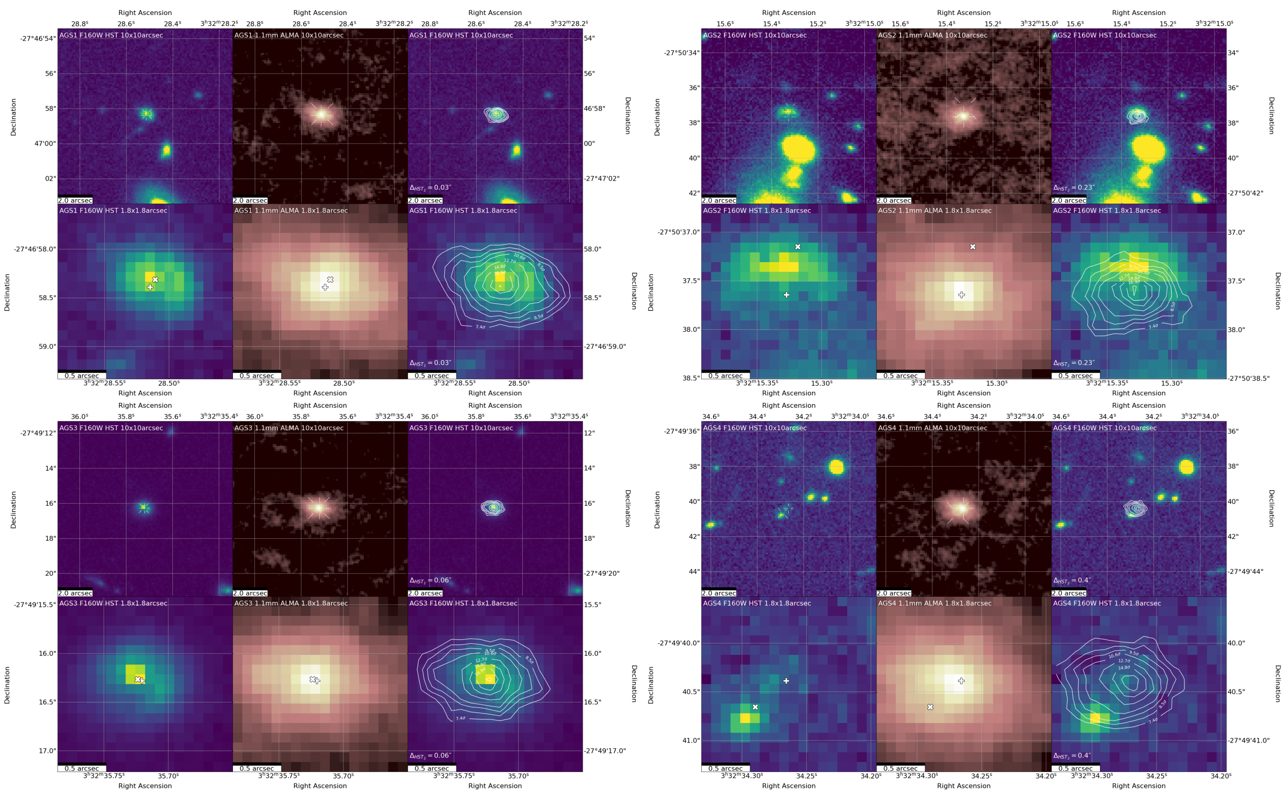

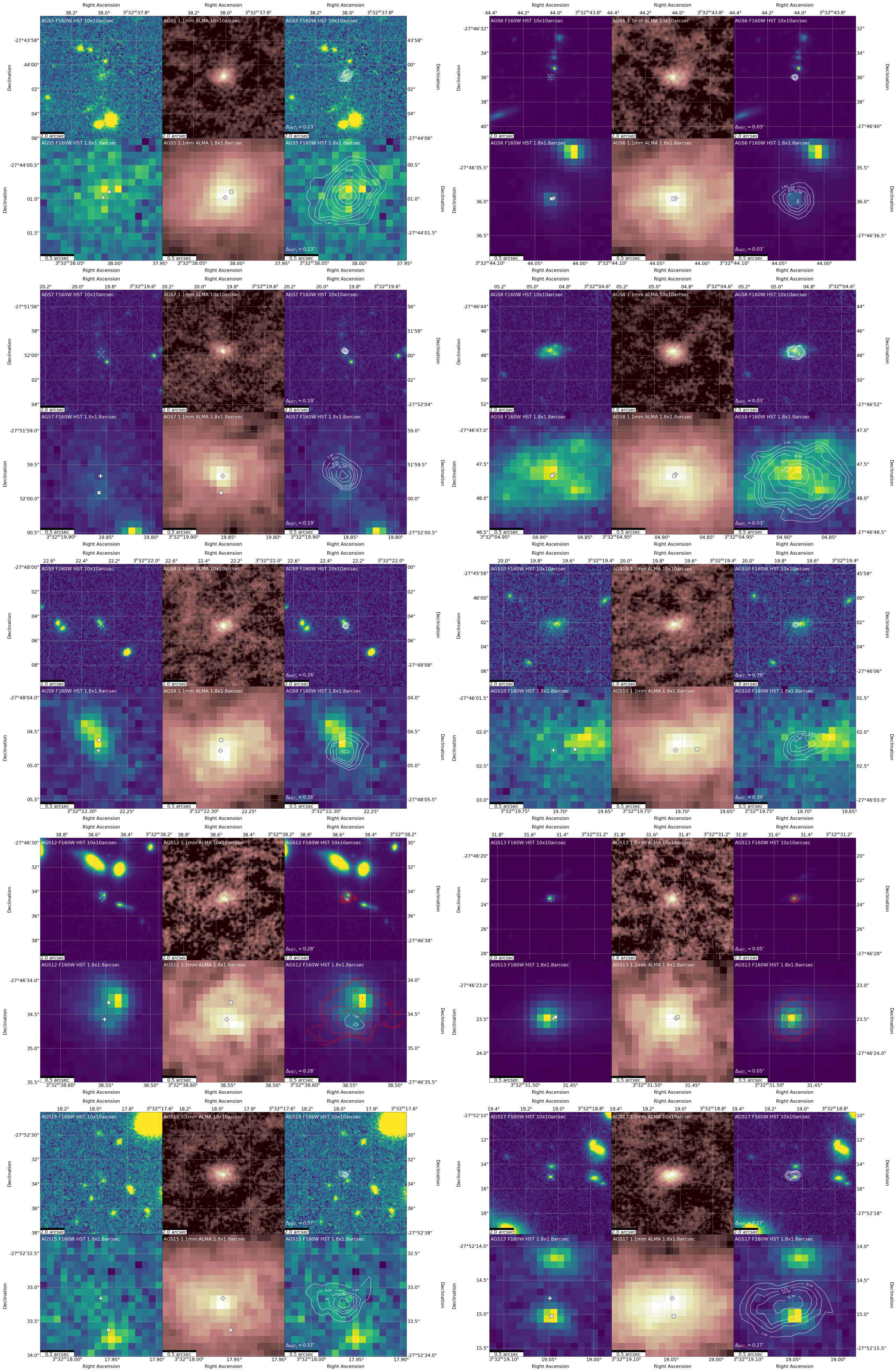
AGS5 F160W HST 10x10arcsec
AGS5 1.1mm ALMA 10x10arcsec
AGS5 F160W HST 1.8x1.8arcsec
AGS5 1.1mm ALMA 1.8x1.8arcsec
AGS6 F160W HST 10x10arcsec
AGS6 1.1mm ALMA 10x10arcsec
AGS6 F160W HST 1.8x1.8arcsec
AGS6 1.1mm ALMA 1.8x1.8arcsec
AGS7 F160W HST 10x10arcsec
AGS7 1.1mm ALMA 10x10arcsec
AGS7 F160W HST 1.8x1.8arcsec
AGS7 1.1mm ALMA 1.8x1.8arcsec
AGS8 F160W HST 10x10arcsec
AGS8 1.1mm ALMA 10x10arcsec
AGS8 F160W HST 1.8x1.8arcsec
AGS8 1.1mm ALMA 1.8x1.8arcsec
AGS9 F160W HST 10x10arcsec
AGS9 1.1mm ALMA 10x10arcsec
AGS9 F160W HST 1.8x1.8arcsec
AGS9 1.1mm ALMA 1.8x1.8arcsec
AGS10 F160W HST 10x10arcsec
AGS10 1.1mm ALMA 10x10arcsec
AGS10 F160W HST 1.8x1.8arcsec
AGS10 1.1mm ALMA 1.8x1.8arcsec
AGS12 F160W HST 10x10arcsec
AGS12 1.1mm ALMA 10x10arcsec
AGS12 F160W HST 1.8x1.8arcsec
AGS12 1.1mm ALMA 1.8x1.8arcsec
AGS13 F160W HST 10x10arcsec
AGS13 1.1mm ALMA 10x10arcsec
AGS13 F160W HST 1.8x1.8arcsec
AGS13 1.1mm ALMA 1.8x1.8arcsec
AGS15 F160W HST 10x10arcsec
AGS15 1.1mm ALMA 10x10arcsec
AGS15 F160W HST 1.8x1.8arcsec
AGS15 1.1mm ALMA 1.8x1.8arcsec
AGS17 F160W HST 10x10arcsec
AGS17 1.1mm ALMA 10x10arcsec
AGS17 F160W HST 1.8x1.8arcsec
AGS17 1.1mm ALMA 1.8x1.8arcsec
Right Ascension
Declination

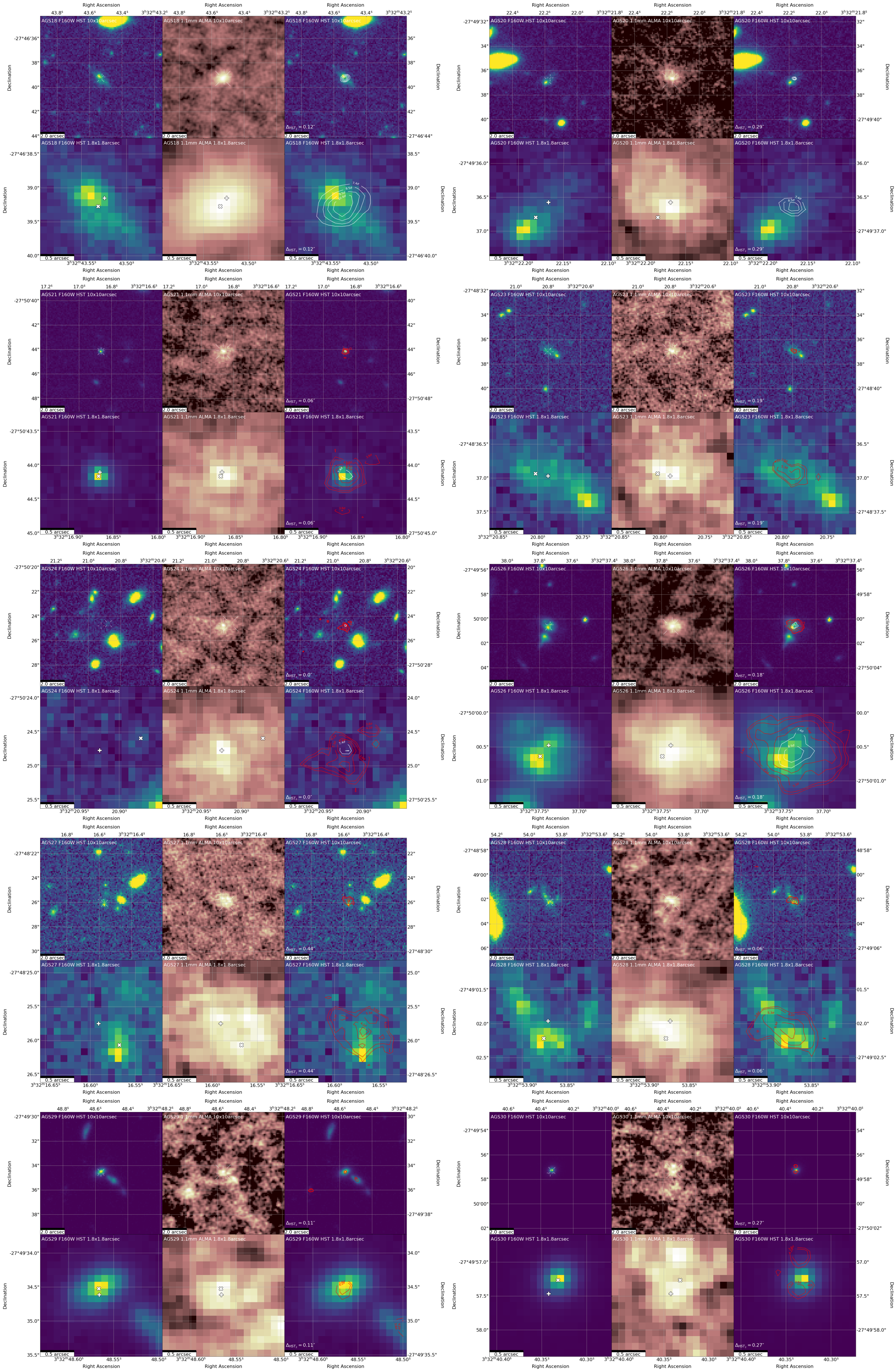
AGS18 F160W HST 10x10arcsec
AGS18 1.1mm ALMA 10x10arcsec
AGS18 F160W HST 1.8x1.8arcsec
AGS18 1.1mm ALMA 1.8x1.8arcsec
AGS20 F160W HST 10x10arcsec
AGS20 1.1mm ALMA 10x10arcsec
AGS20 F160W HST 1.8x1.8arcsec
AGS20 1.1mm ALMA 1.8x1.8arcsec
AGS21 F160W HST 10x10arcsec
AGS21 1.1mm ALMA 10x10arcsec
AGS21 F160W HST 1.8x1.8arcsec
AGS21 1.1mm ALMA 1.8x1.8arcsec
AGS23 F160W HST 10x10arcsec
AGS23 1.1mm ALMA 10x10arcsec
AGS23 F160W HST 1.8x1.8arcsec
AGS23 1.1mm ALMA 1.8x1.8arcsec
AGS24 F160W HST 10x10arcsec
AGS24 1.1mm ALMA 10x10arcsec
AGS24 F160W HST 1.8x1.8arcsec
AGS24 1.1mm ALMA 1.8x1.8arcsec
AGS26 F160W HST 10x10arcsec
AGS26 1.1mm ALMA 10x10arcsec
AGS26 F160W HST 1.8x1.8arcsec
AGS26 1.1mm ALMA 1.8x1.8arcsec
AGS27 F160W HST 10x10arcsec
AGS27 1.1mm ALMA 10x10arcsec
AGS27 F160W HST 1.8x1.8arcsec
AGS27 1.1mm ALMA 1.8x1.8arcsec
AGS28 F160W HST 10x10arcsec
AGS28 1.1mm ALMA 10x10arcsec
AGS28 F160W HST 1.8x1.8arcsec
AGS28 1.1mm ALMA 1.8x1.8arcsec
AGS29 F160W HST 10x10arcsec
AGS29 1.1mm ALMA 10x10arcsec
AGS29 F160W HST 1.8x1.8arcsec
AGS29 1.1mm ALMA 1.8x1.8arcsec
AGS30 F160W HST 10x10arcsec
AGS30 1.1mm ALMA 10x10arcsec
AGS30 F160W HST 1.8x1.8arcsec
AGS30 1.1mm ALMA 1.8x1.8arcsec
Right Ascension
Declination
2.0 arcsec
0.5 arcsec

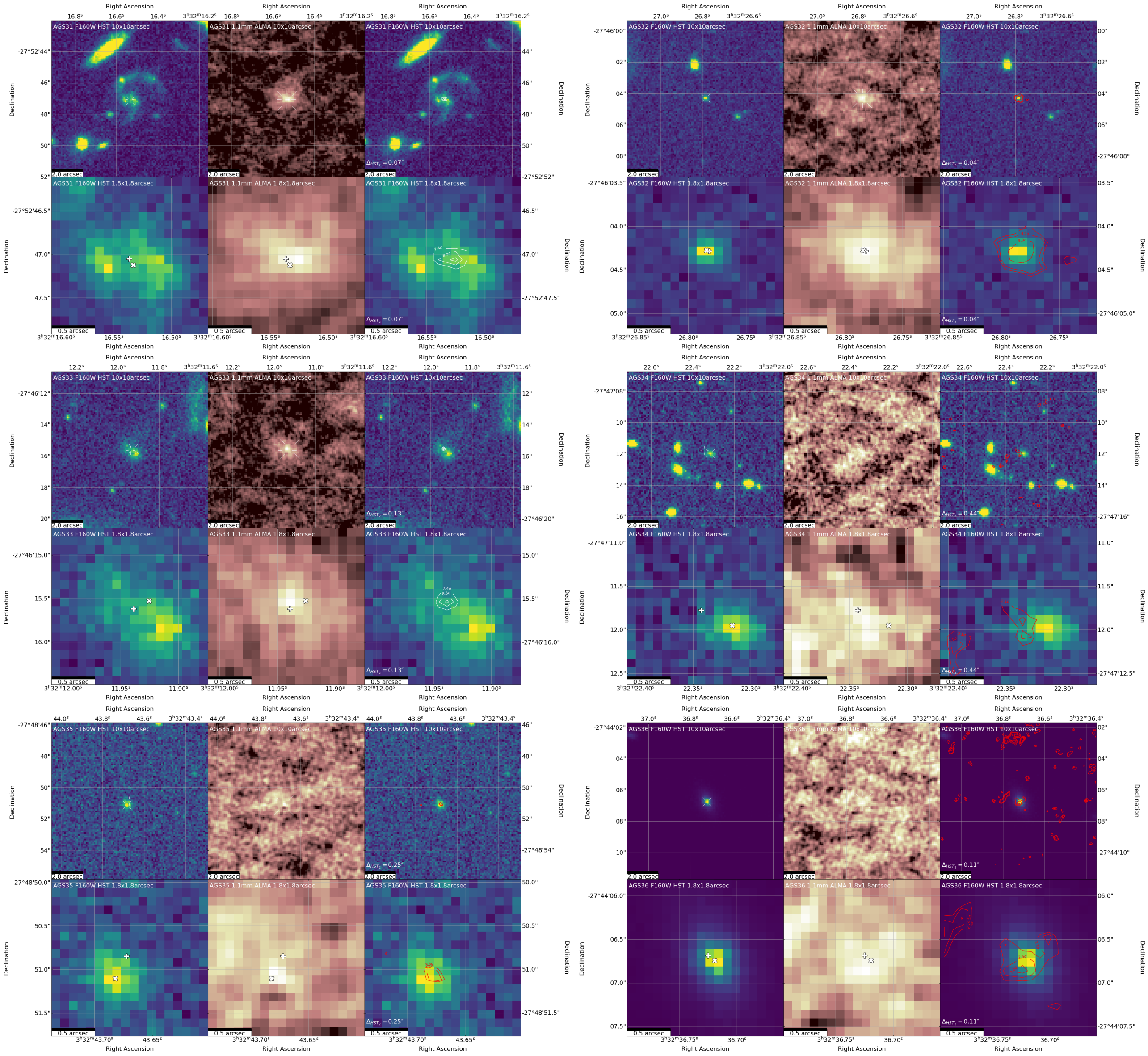

AGS31 F160W HST 10x10arcsec
AGS31 1.1mm ALMA 10x10arcsec
AGS31 F160W HST 10x10arcsec
AGS31 F160W HST 1.8x1.8arcsec
AGS31 1.1mm ALMA 1.8x1.8arcsec
AGS31 F160W HST 1.8x1.8arcsec
AGS32 F160W HST 10x10arcsec
AGS32 1.1mm ALMA 10x10arcsec
AGS32 F160W HST 10x10arcsec
AGS32 F160W HST 1.8x1.8arcsec
AGS32 1.1mm ALMA 1.8x1.8arcsec
AGS32 F160W HST 1.8x1.8arcsec
AGS33 F160W HST 10x10arcsec
AGS33 1.1mm ALMA 10x10arcsec
AGS33 F160W HST 10x10arcsec
AGS33 F160W HST 1.8x1.8arcsec
AGS33 1.1mm ALMA 1.8x1.8arcsec
AGS33 F160W HST 1.8x1.8arcsec
AGS34 F160W HST 10x10arcsec
AGS34 1.1mm ALMA 10x10arcsec
AGS34 F160W HST 10x10arcsec
AGS34 F160W HST 1.8x1.8arcsec
AGS34 1.1mm ALMA 1.8x1.8arcsec
AGS34 F160W HST 1.8x1.8arcsec
AGS35 F160W HST 10x10arcsec
AGS35 1.1mm ALMA 10x10arcsec
AGS35 F160W HST 10x10arcsec
AGS35 F160W HST 1.8x1.8arcsec
AGS35 1.1mm ALMA 1.8x1.8arcsec
AGS35 F160W HST 1.8x1.8arcsec
AGS36 F160W HST 10x10arcsec
AGS36 1.1mm ALMA 10x10arcsec
AGS36 F160W HST 10x10arcsec
AGS36 F160W HST 1.8x1.8arcsec
AGS36 1.1mm ALMA 1.8x1.8arcsec
AGS36 F160W HST 1.8x1.8arcsec
Right Ascension
Declination

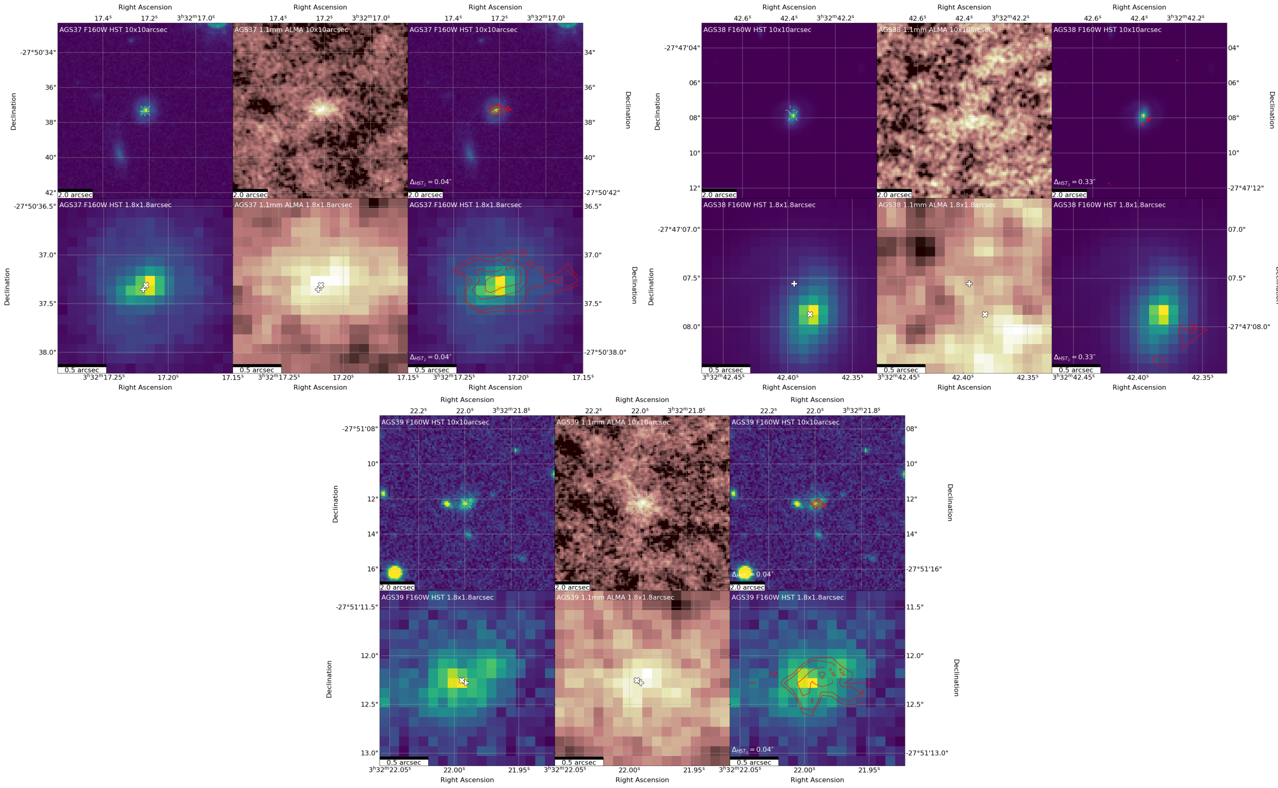

FIGURE 4.3: Galaxy cutouts of AGS galaxies. The top row of each figure shows 10x10 arcsecond cutouts centered on the ALMA source position of respectively F160W mosaic, GOODS-ALMA mosaic, and F160W mosaic with ALMA contours. The bottom row of each figure displays the same, but zoomed to a 1.8x1.8 cutout. The straight marker denote the position of the 1.1mm ALMA source and angled markers denote the position of the 3D-HST counterpart.

By closer inspection of each individual galaxy it is apparent that the contours of several sources are not perfectly aligned with their respective 3D-HST counterpart even after applying the astrometric correction. It is then indeed valid to question the association of the sources. But even with this misalignment, they may still be the same galaxy. As an example we refer to the local starburst galaxies e.g. the merging Antennae Galaxies (NGC 4038/ 4039), Figure 4.4.

FIGURE 4.4: The Antennae Galaxies. Credit: ESA/Hubble & NASA

In this particular example we see that even within the merger, there are regions where dust is significantly more prevalent than others. If an optical HST measurement is taken at a bluer and dust-free region, and an ALMA 1.1mm measurement is taken in a much dustier region, offset from the position of the HST measurement, the blue SED data will suggest a dust-poor galaxy and the red SED will suggest a dust-rich galaxy. This inconsistency with the optical and IR data can cause difficulties trying to impose energy balance which can then produce bad fits. In this case the fitting code may not be at fault, but rather the data is inconsistent.

Figure 4.5 shows the resulting SED fit with the XFSPS-12SB along with contoured F160W cutouts to evaluate whether or not it is reasonable to assume energy balance for these AGS galaxies.

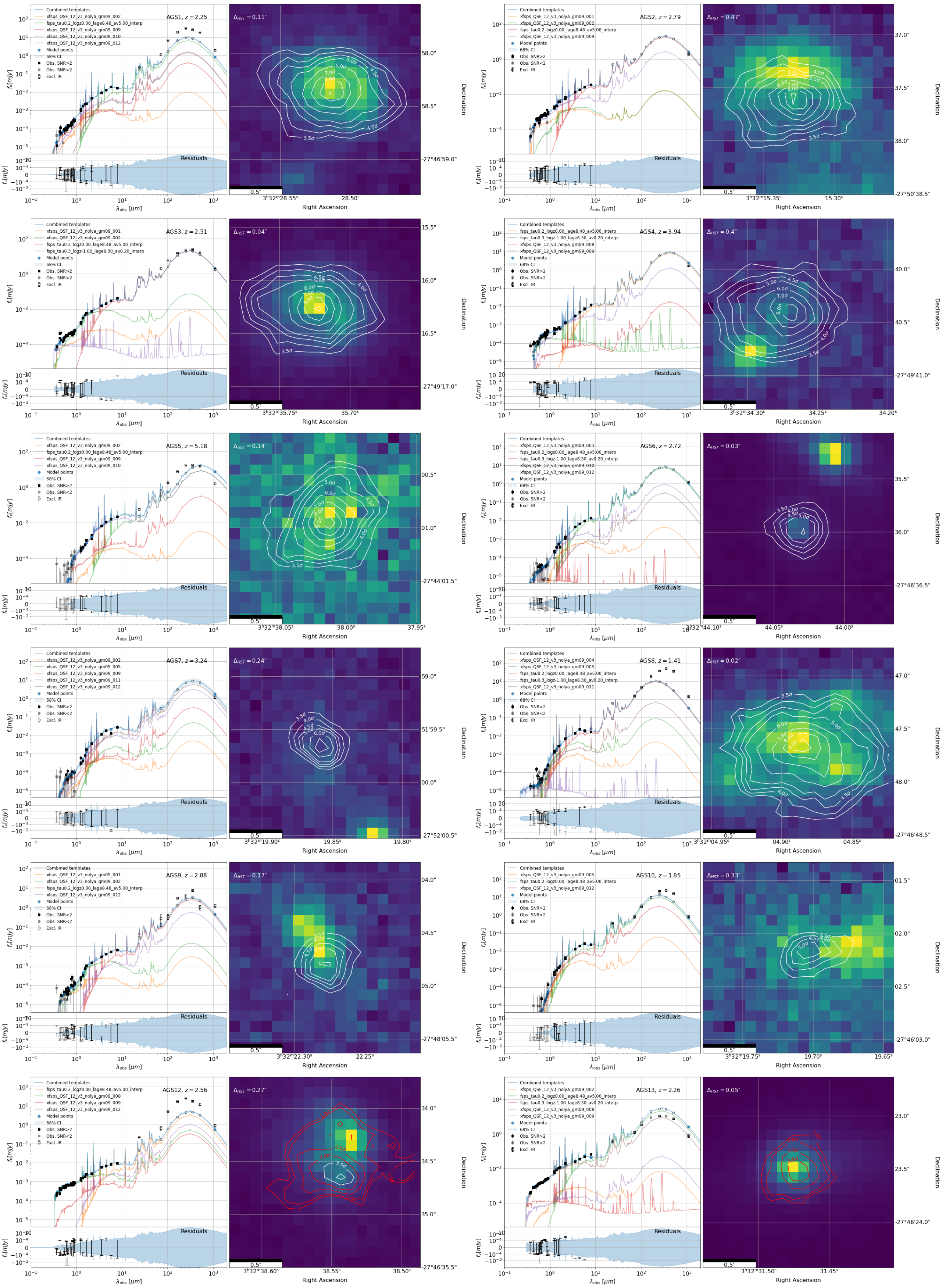
AGS1, z = 2.25
AGS2, z = 2.79
AGS3, z = 2.51
AGS4, z = 3.94
AGS5, z = 5.18
AGS6, z = 2.72
AGS7, z = 3.24
AGS8, z = 1.41
AGS9, z = 2.88
AGS10, z = 1.85
AGS12, z = 2.56
AGS13, z = 2.26
Combined templates
Model points
68% CI
Obs. SNR>2
Obs. SNR<2
Excl. IR
Residuals
Right Ascension
Declination

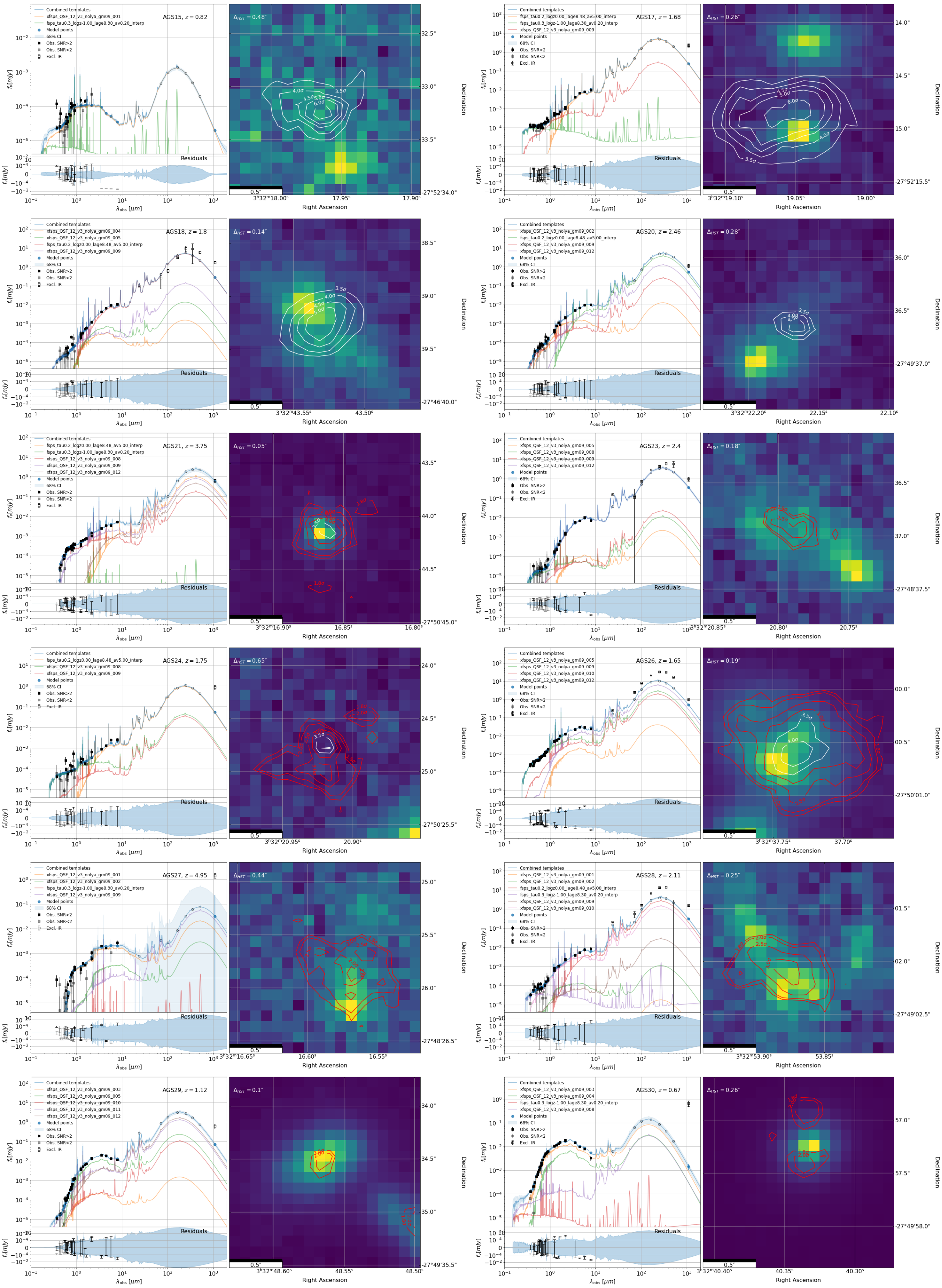
AGS15, $z = 0.82$
AGS17, $z = 1.68$
AGS18, $z = 1.8$
AGS20, $z = 2.46$
AGS21, $z = 3.75$
AGS23, $z = 2.4$
AGS24, $z = 1.75$
AGS26, $z = 1.65$
AGS27, $z = 4.95$
AGS28, $z = 2.11$
AGS29, $z = 1.12$
AGS30, $z = 0.67$
Combined templates
Model points
68% CI
Obs. SNR>2
Obs. SNR<2
Excl. IR
Residuals
λ_{obs} [μm]
f_ν[mJy]
Right Ascension
Declination

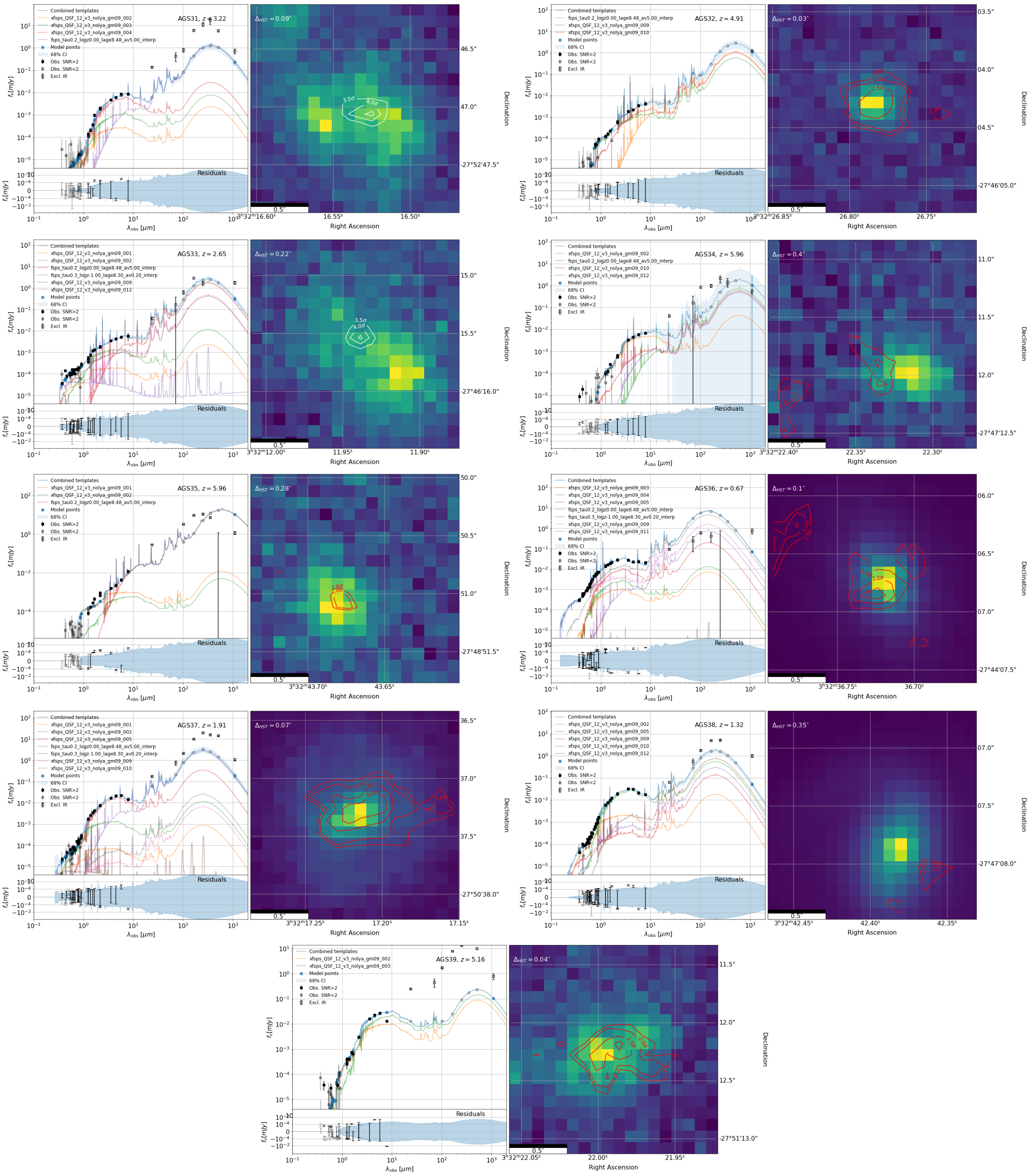

FIGURE 4.5: SED fits with the XFSPS-12SB template set excluding infrared data, along with 1.8x1.8 arcsecond F160W cutouts and ALMA contours. The separation between ALMA source and 3D-HST source is given by the value Δ_{HST} in the top left corner of the F160W cutout.

For some sources with weaker SNR contours (e.g. AGS30 and AGS38) it is clear that the offset from the HST counterpart may be having an effect on the SED predictions as the assumption of energy balance is invalidated. Even for stronger sources with higher SNR contours (AGS31 and AGS33) there are cases where the morphologies do not line up creating difficulties for the SED fitting, implying that the offset plays a limiting role in our prediction of the FIR SED. Another limiting trait may be identified by inspecting AGS31, which Franco et al. 2020 [40] argues shows morphological characteristics of a merger in the form of large tidal tails. This might mean that complex morphologies may also have an effect on the FIR SED fit when using energy balance and UV-optical data. However with none of these limiting traits, e.g. with a simple point-like compact morphology and a small spatial offset (AGS3, 6, 21, 32) we are able to produce good FIR SEDs and 1.1mm predictions with energy balance.

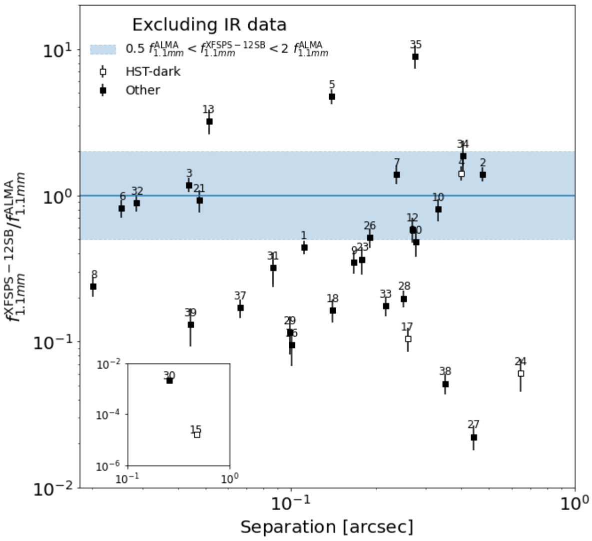

(A)

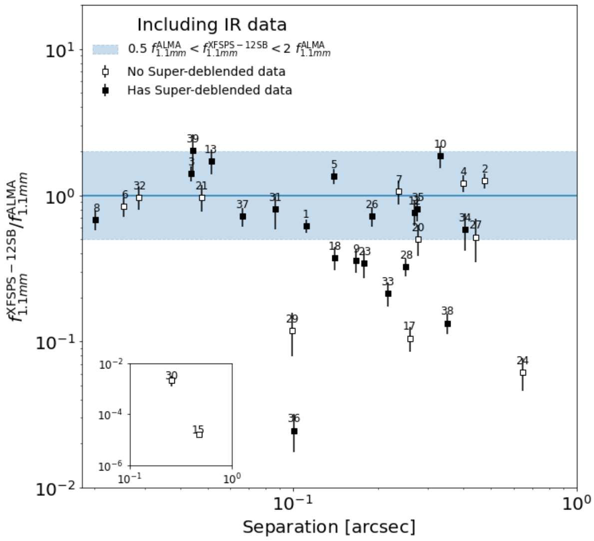

(B)

FIGURE 4.6: 4.6a) Ratio of energy balance XFSPS-12SB modeled 1.1mm fluxes to 1.1mm ALMA fluxes versus spatial separation between 1.1mm ALMA source and HST H-band counterpart with UV-optical data and 4.6b) including IR data (Super-deblended and 1.1mm ALMA).

The spatial offset effect is more clearly illustrated on Figure 4.6a by comparing the flux ratio $f_{1.1mm}^{\mathrm{XFSPS-12SB}}/f_{1.1mm}^{\mathrm{ALMA}}$ with the spatial separation. It can also be seen on Figure 4.6b how the 1.1mm flux is more accurately reproduced when including IR constraints, as the majority of sources are reproduced within a factor of 2 of the ALMA flux and all sources with a $<$ 0.1arcsec separation are within a factor of 2.

The same comparison of predicted flux and spatial offset can be done without imposing energy balance by fitting with the XFSPS-1210PAH set.

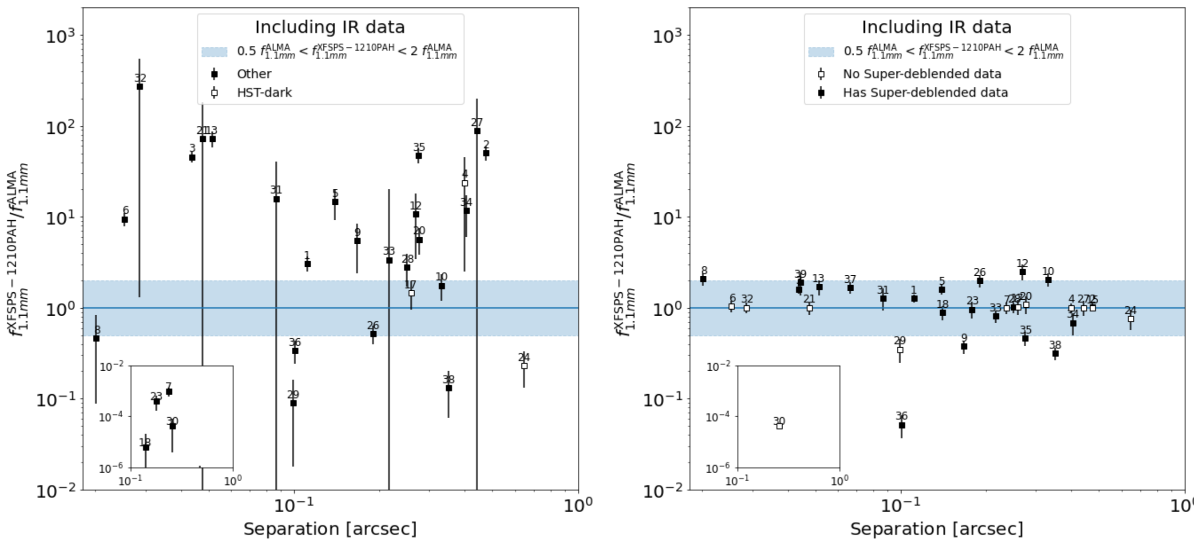

(A) (B)

FIGURE 4.7: 4.7a) Ratio of XFSPS-1210PAH (not imposing energy balance) modeled 1.1mm fluxes to 1.1mm ALMA fluxes versus spatial separation between 1.1mm ALMA source and HST H-band counterpart with UV-optical data and 4.7b) including IR data (Super-deblended and 1.1mm ALMA).

Figure 4.7 shows how predictions excluding energy balance and IR data lacks the constraints to accurately predict the 1.1mm flux and FIR SED. Meanwhile the fits including IR constraints are able to reproduce the fluxes of almost all sources within a factor of 2 of the ALMA fluxes.

In general the SED fits excluding IR constraints produce significantly different 1.1mm fluxes compared to fits including IR constraints. One might worry that the main driver in the differently predicted FIR may come from redshift differences when modeling with-/without IR data.

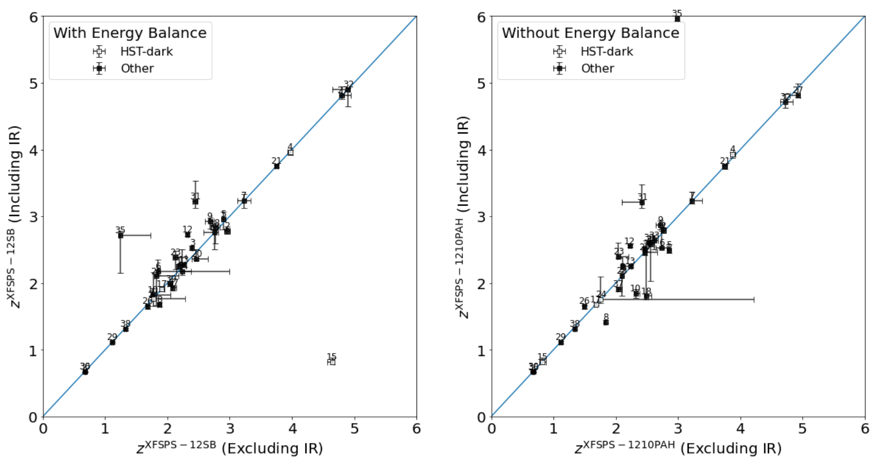

FIGURE 4.8: (*Left*) Photometric redshift estimate comparison between UV-optical fits and UV-optical-IR (Super-deblended and 1.1mm ALMA) fits with the energy balanced XFSPS-12SB set and (*Right*) with the XFSPS-1210PAH set not imposing energy balance.

Figure 4.8 does however dismiss any redshift degeneracy when fitting with/without IR data. The difference in the predicted FIR may lie in systematics within the data set, e.g. shallow and large beam size IRAC channel 3/4 data is weighted too much in UV-optical fits as these fits are very sensitive to the limited data available, thus strongly affecting the FIR SED. Essentially the question is why the code is not picking the best UV-optical-IR solution when fitting the UV-optical range.

Section summary

In this section we have investigated the robustness of the energy balance principle within our sample of DSFGs by fitting UV-optical and UV-optical-IR data. The take-aways from this analysis are.

- Energy balance does not work for UV-optical fits where the 1.1mm ALMA source and HST H-band counterpart are spatially disconnected.
- The morphology also seems to play a role, as complex morphologies, like merging traits in the form of tidal tails, produce bad UV-optical data fits with energy balance, even when the offset is small.
- The few good UV-optical fits are produced for sources with a small spatial offset and a compact HST H-band counterpart
- Energy balance does seem to work for fits including IR constraints, which reproduced the FIR SED more accurately and estimated the majority of 1.1mm fluxes within a factor of 2 of the ALMA fluxes.

We can generalize this methodology to try and predict what the 1.1mm FIR Universe looks like according to EAZY when imposing energy balance and providing UV-optical data or UV-optical-IR (up to 500μm SPIRE) constraints.

4.2 The Universe according to EAZY: Synthetic photometry

To determine the Universe predicted by EAZY we aim to produce a 1.1mm synthetic map, comparable to the real 69arcmin^2 1.1mm GOODS-ALMA map provided, Gómez-Guijarro et al. in prep, Figure 4.9. It is worth noting that the provided map is not identical to the map presented in the Franco et al. papers, and thus not with the same depth. This is particularly visible for sources of the Franco et al. 2020 [39] Supplementary Catalog where

IRAC and VLA was used to crossmatch and extend the source detection to lower SNR. These sources appear very faint on the map provided due to the extra lack of depth.

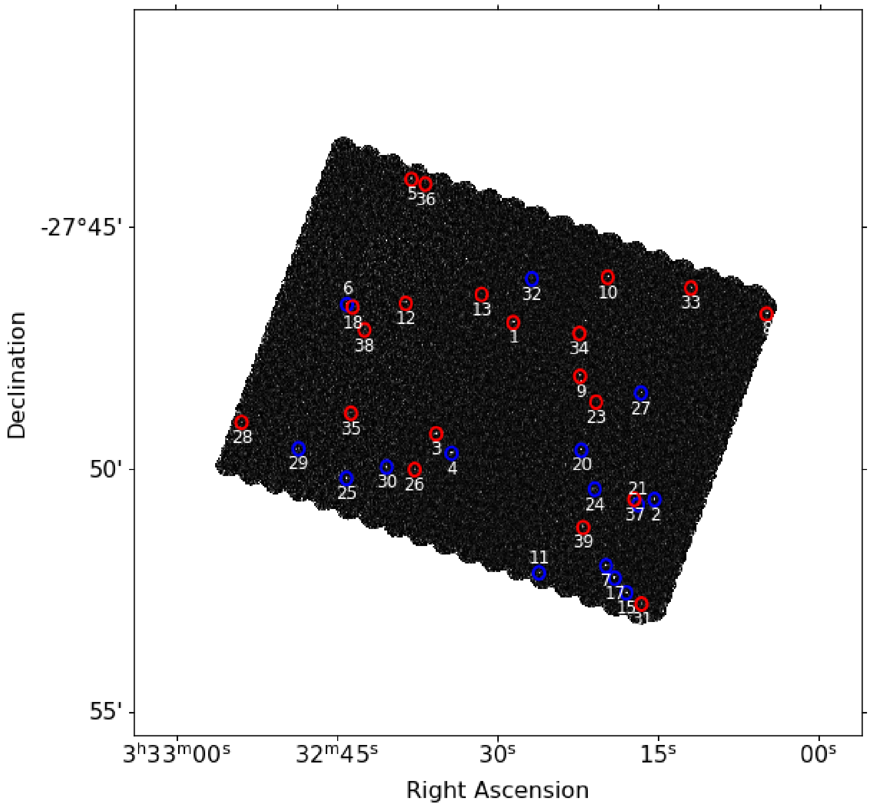

FIGURE 4.9: The 69arcmin^2 GOODS-ALMA field by Franco et al. with the position of each AGS source highlighted. Blue circles represent AGS sources without Super-deblended IR data, and red circles represent AGS sources with crossmatching Super-deblended IR data.

In order to generate the synthetic maps we determine all sources from the 3D-HST catalogue overlapping with the 69arcmin^2 1.1mm GOODS-ALMA map and use EAZY to fit all these galaxies and extract the predicted 1.1mm model flux. First a subcatalogue of sources with optical 3D-HST data cross-matched (within 1 arcsec) with Super-deblended IR (MIPS 24μm, PACS 70μm/100μm/160μm, SPIRE 250μm/350μm/500μm) data is produced.

When referring to synthetic maps excluding/including IR data we now mean UV-optical only or UV-optical-IR data (up to the 500μm SPIRE band and excluding the 1.1mm ALMA data as that is what we are trying to predict) in this section 4.2.

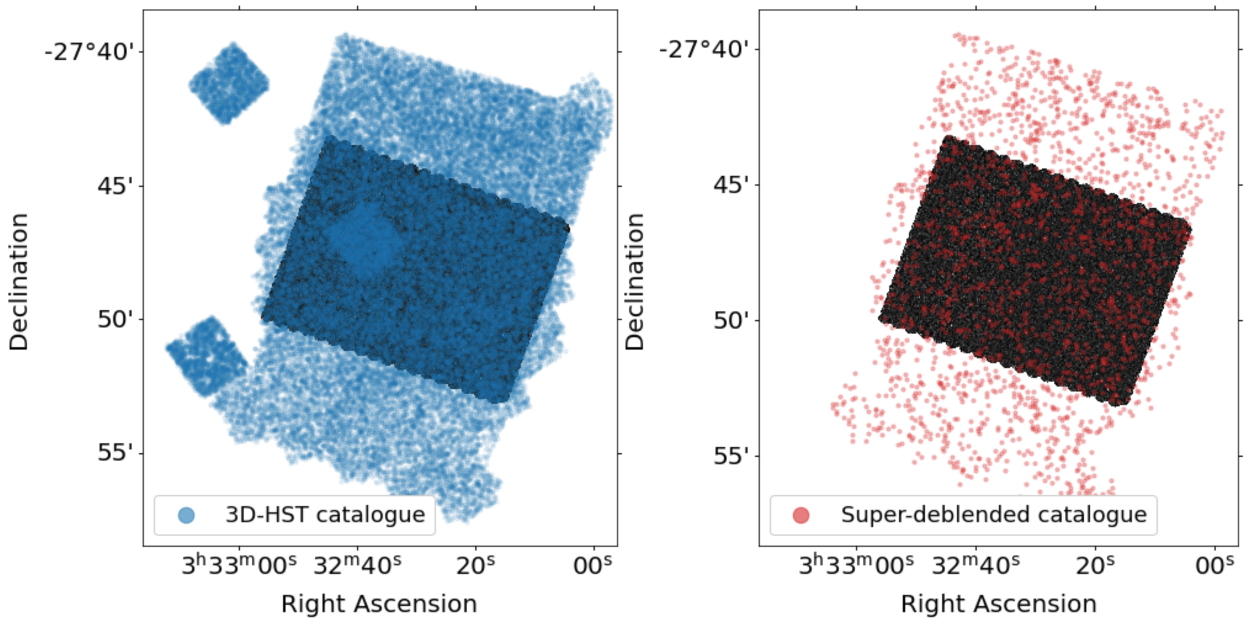

FIGURE 4.10: *Left*) All sources of the 3D-HST catalogue superimposed on the GOODS-ALMA map. *Right*) All sources of the Super-deblended catalogue superimposed on the GOODS-ALMA map.

Figure 4.10 shows all sources of the 3D-HST catalogue overlaid on the 1.1mm GOODS-ALMA map, and all the Super-deblended sources on top of the 1.1mm map. The blue map of 3D-HST sources shows several dense patches of sources, one concentrated on top of the 1.1mm GOODS-ALMA map. This dense patch consists of four 4.7 arcmin Hubble Ultra Deep Field survey (HUDF) pointings, and with ~ 620 sources/arcmin^2 they are twice as dense as the rest of the Franco et al. GOODS-ALMA field.

The synthetic map is created by initializing a Python array corresponding to the same size and shape as the given GOODS-ALMA map. This empty array is then filled with gaussian noise, sampled from the Figure 4.1 pixel distribution of the GOODS-ALMA map with $\sigma_{\text{RMS}} \simeq 0.085$mJy/beam and a mean of ~ 0mJy/beam. All sources that fall within the 1.1mm GOODS-ALMA map are compiled to a new catalogue and fit with EAZY and the XFSPS-12SB set and their 1.1mm model flux is extracted. This flux is then convolved with the PSF (by multiplication). The PSF has been cut in a 50×50 pixel crop around the center and it has been normalized to the peak value, as Franco et al. 2020 [40] report peak flux values, we stick to this convention.

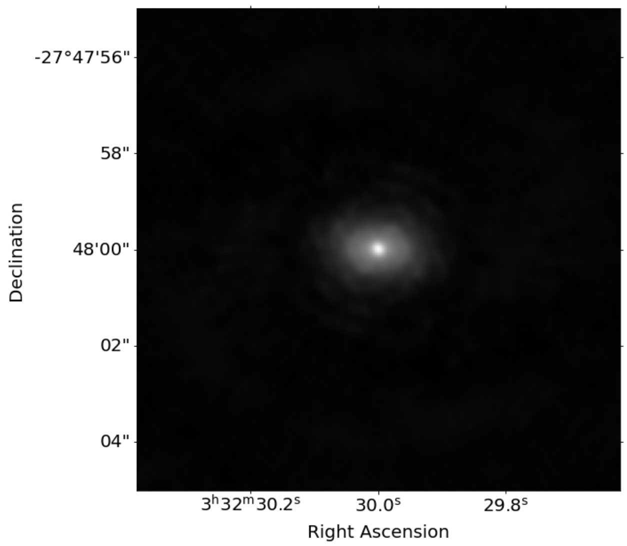

FIGURE 4.11: The ALMA PSF image.

Following the source convolution by the PSF, the source is placed on top of the empty noise map. This addition of sources is done in a simple FOR loop iterating over all objects in the catalogue. Once all sources were placed this procedure was repeated for the catalogue with cross-matched Super-deblended FIR data. Both synthetic maps were visualized on a plot with the same normalization Figure 4.12.

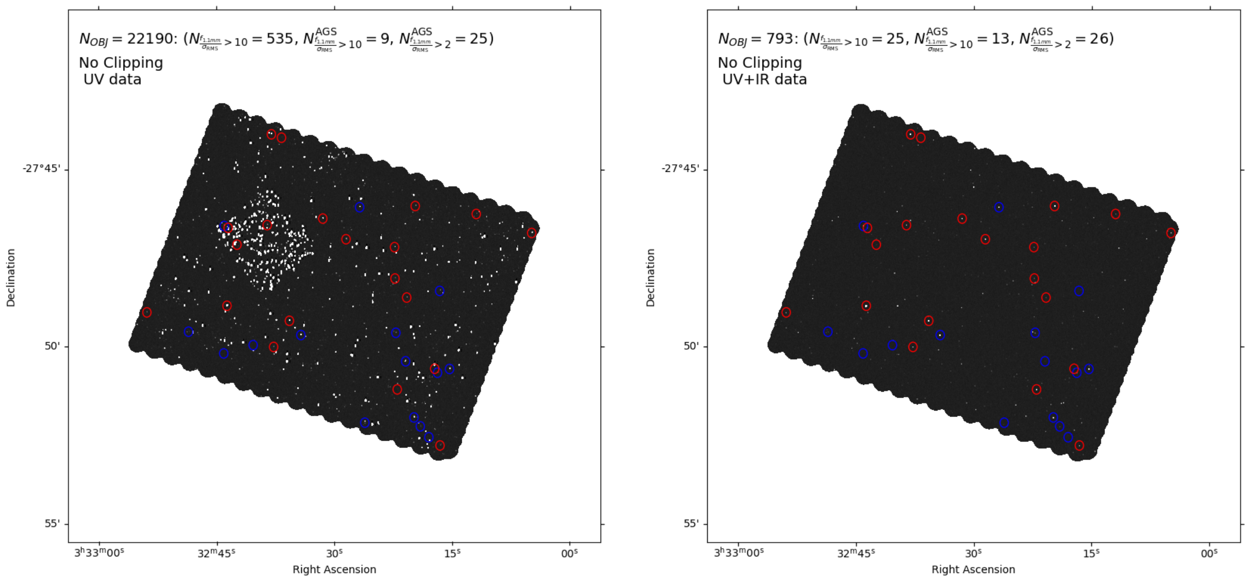

FIGURE 4.12: (*Left*) Synthetic map generated using UV-optical data only and (*Right*) Including FIR data

From Figure 4.12 we clearly see that the UV-optical-IR synthetic map looks more accurate and comparable to the GOODS-ALMA map, as it is significantly dimmer when IR data up to the 500μm SPIRE band is included. However, when IR data is excluded and only optical data up to the 8μm IRAC band is fit, the Universe looks much brighter. This is in stark contrast to what we found on Figure 3.15b where the XFSPS-12SB set was underpredicting the 1.1mm flux for the most part, whereas now the synthetic map visually points to an overestimation of 1.1mm sources.

With this strange excess brightness on the UV-optical map, we focus our efforts on improving this map by exploring a range of selection criteria for the UV-optical synthetic map, which will lastly also be applied to the UV-optical-IR map for possible improvements.

4.2.1 Sample inspection and selection

Particularly the HUDF region of the UV-optical map seems to produce an excess of bright sources at 1.1mm, and upon inspection of the output SEDs and the corresponding redshifts we find 337 sources redshifted to the very end of the redshift grid with $z \sim 5.95$ whereof 161 of them are within the HUDF, and 57/161 in the HUDF have SNR > 2 on the synthetic map. Figure 4.13c shows 13 of these galaxies in the HUDF exhibit SNRs beyond $f_{1.1mm}/\sigma_{rms} > 1000$.

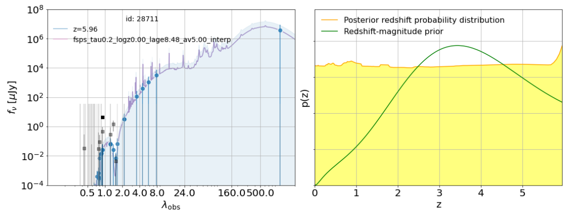

(A)

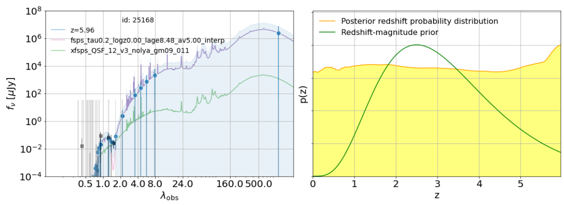

(B)

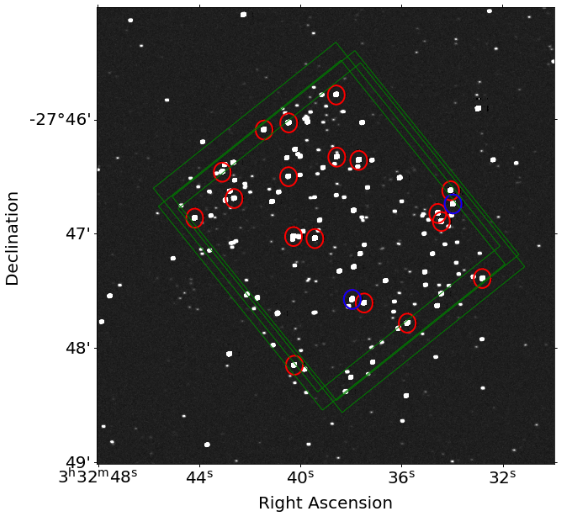

(C)

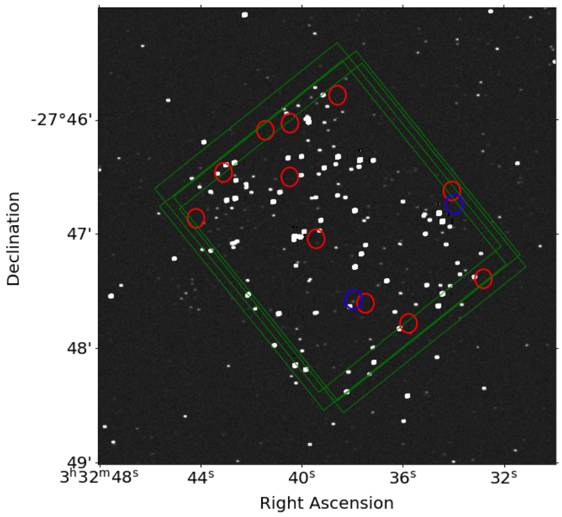

(D)

FIGURE 4.13: 4.13a, 4.13b) The SEDs of the two blue sources are shown above with SNR $f_{1.1mm}/\sigma_{rms} \sim 28949$ and ~ 42991. 4.13c) 4x4 arcmin close-up of the synthetic map centered on the HUDF (RA,Dec =53.1625°, −27.7836°) with 13 sources marked with $z \sim 5.95$ and SNR > 1000. center . 4.13d) Synthetic map after removing all sources with a faulty $z \sim 5.95$.

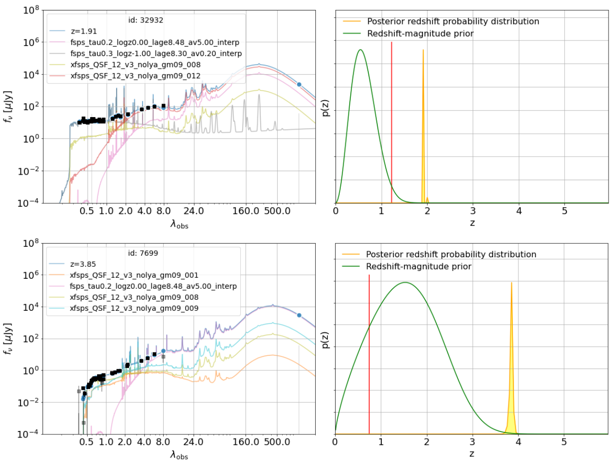

(A)

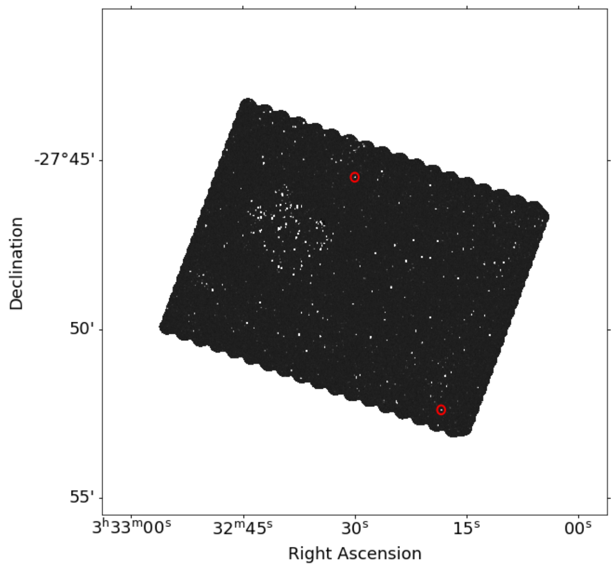

(B)

FIGURE 4.14: *Left*) SEDs of two sources with high SNR and overestimated photo-z compared to the reported spec-z. *Right*) Synthetic map with location of sources marked

Common for all of them are the very broad posterior redshift probability distribution, and for many of these sources the constraints on the UV-optical SED are poor due to the mediocre data with SNR < 2. Removing the 337 false sources with $z \sim 5.95$ does however not solve the problem entirely, as shown on Figure 4.13d. This suggests that there are many intermediary sources where the source redshift may have still been overestimated but not all the way up to the redshift grid limit.

Two such intermediary cases are highlighted on the synthetic map on Figure 4.14b. Their posterior redshift probability distribution are shifted to higher redshifts compared to the spectroscopic redshifts reported as seen on Figure 4.14a. With many faulty redshifts at intermediary values it would be tedious to identify and correct/remove each one among ~ 22000 sources. While the removal of sources placed at the redshift grid limit $z \sim 5.95$ does improve the synthetic map slightly, there is still an abundance of bright spurious sources. From Figure 4.13a and Figure 4.13b we can identify another common trait of these bad fits, namely the large errors on their 1.1mm fluxes. As only the modelled 1.1mm flux value is extracted and multiplied by the PSF to be placed on the map, this value can be highly uncertain as its error may be larger than the actual modelled 1.1mm flux by orders of magnitude. Thus the source may not even be visible on the map if the actual flux value is in the lower end of this range. Instead of clipping the sources at the redshift grid limit, a SNR selection is made to only include sources with $f_{1.1mm}/\sigma_{1.1mm} > 3$, which is slightly below the sample median $(f_{1.1mm}/\sigma_{1.1mm})_{\rm median} \approx 4$, to not unnecessarily reduce the sample too much. As the clipping at the redshift grid limit was insufficient we also allow for more flexibility and extend the redshift grid to

$z = 12$ so we can also compare with the reported photo-zs catalogued in the 3D-HST catalogue with the same redshift grid limit. Extending the redshift grid to $z = 12$ does not affect the redshift estimate of the majority of the AGS sample, only AGS34 and AGS35 are redshifted to respectively $z_{\text{AGS34}} \approx 6.36$ and $z_{\text{AGS35}} \approx 11.82$ (Appendix B Figure B.1).

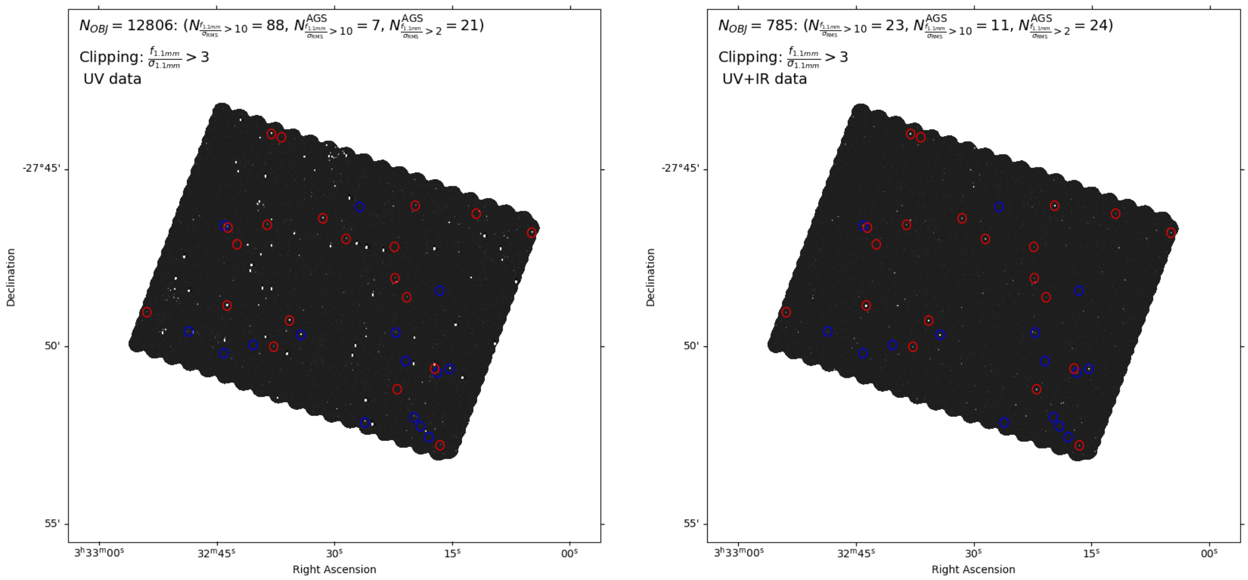

FIGURE 4.15: *Left*) Synthetic map excluding IR data with sources clipped by $f_{1.1mm}/\sigma_{1.1mm} > 3$. *Right*) Synthetic map including IR data with sources clipped by $f_{1.1mm}/\sigma_{1.1mm} > 3$

The SNR clipping, $f_{1.1mm}/\sigma_{1.1mm} > 3$, cuts 9384 objects eliminating a great amount of excess brightness particularly in the HUDF region, improving the synthetic map considerably as illustrated on Figure 4.15. However with 88 sources remaining with SNR > 10 (as indicated by the $N_{\frac{f_{1.1mm}}{\sigma_{\text{RMS}}}>10} = 88$ value) there are still too many false sources compared to the GOODS-ALMA map, where just the AGS sources are detected. Upon SNR clipping 5/33 AGS sources with uncertain modeled 1.1mm fluxes are removed (AGS7, 27, 32, 33, 34) along with the spurious sources. Two of the remaining spurious sources following the clipping are marked on Figure 4.16b and their SEDs (Figure 4.16a) show a lack of constraining data in the optical.

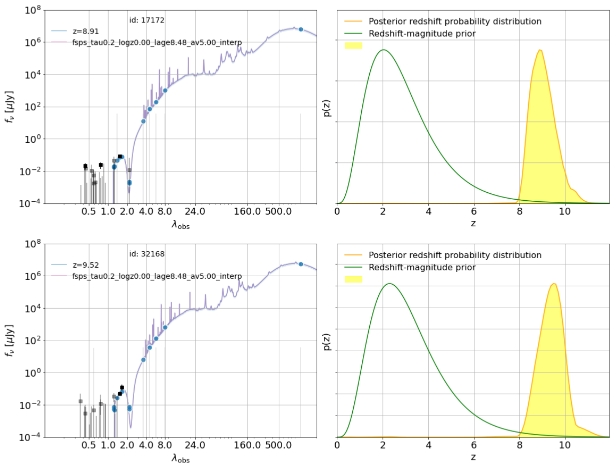

(A)

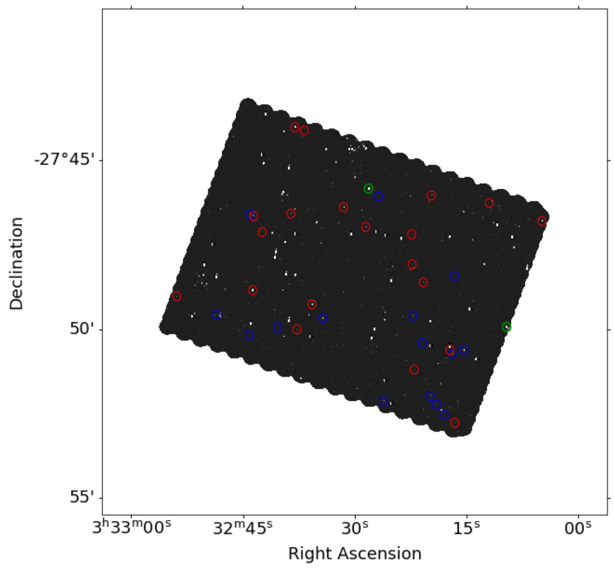

(B)

FIGURE 4.16: *Left*) SEDs of two sources with high SNR and overestimated photo-z. *Right*) Synthetic map with location of sources marked

To improve the map we can add an additional selection criteria requiring the object to have at least 10 data points with SNR > 2 e.g. $N_{\frac{f_{obs}}{\sigma_{obs}}>2} > 10$. This cuts another 2838 sources leaving 9968 objects added to the synthetic map (Figure 4.17a).

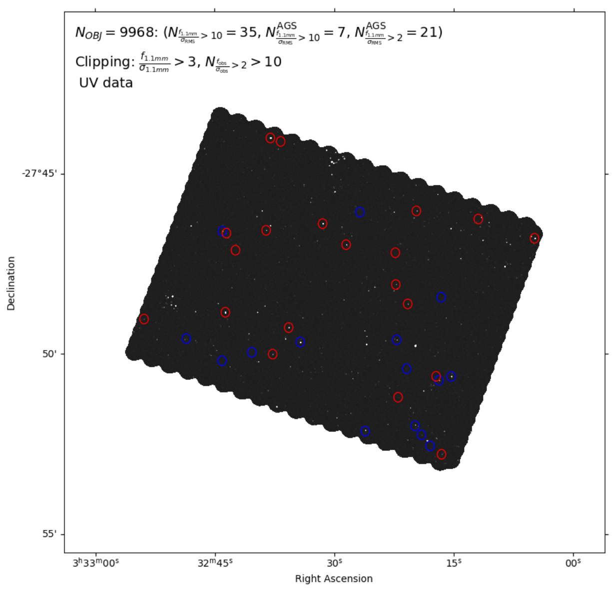

(A)

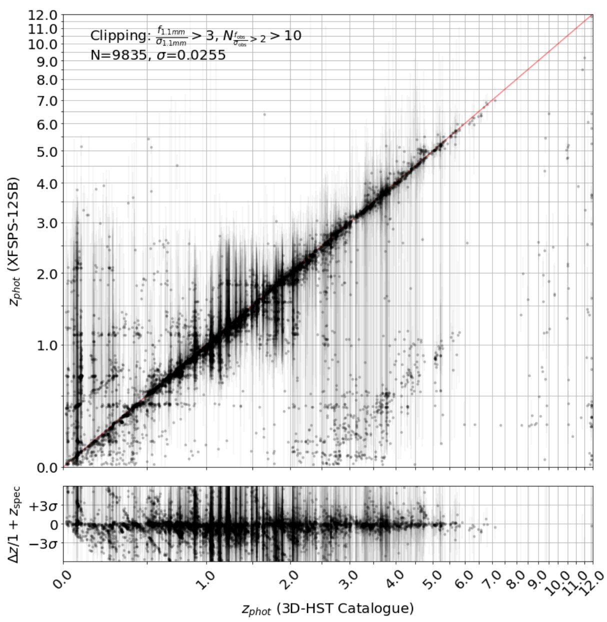

(B)

FIGURE 4.17: 4.17a) Synthetic map excluding IR data clipped by $f_{1.1mm}/\sigma_{1.1mm} > 3$ and $N_{\frac{f_{obs}}{\sigma_{obs}}>2} >$ 10. 4.17b) Comparison of XFSPS-12SB fits output redshift with 3D-HST catalogue redshift with $f_{1.1mm}/\sigma_{1.1mm} > 3$ and $N_{\frac{f_{obs}}{\sigma_{obs}}>2} > 10$ clipping

With this selection $N_{\frac{f_{1.1mm}}{\sigma_{\rm RMS}}>10} = 35$ bright sources with SNR > 10 remain. Unfortunately they are not all 33 AGS sources, as just 21 AGS sources have $f_{1.1mm}/\sigma_{\rm RMS} > 2$ and only 7 of them $f_{1.1mm}/\sigma_{\rm RMS} > 10$. It is also worth noting that imposing this extra selection criteria does not remove any additional AGS sources apart from the 5 already cut from the SNR clipping.

We can examine the sample as a whole by comparing the output photometric redshifts with the reported 3D-HST catalogue photometric redshifts as shown on Figure 4.17b. It appears that some fitted objects have large errors on their redshift estimate as also previously noted. Instead of clipping by $N_{\frac{f_{obs}}{\sigma_{obs}}>2} > 10$ we can try clipping the sample for sources where the photometric redshift error is below 20%, e.g. $\sigma_{z,max} < 20\%$. With SNR clipping $f_{1.1mm}/\sigma_{1.1mm} > 3$ and redshift error clipping $\sigma_{z,max} < 20\%$, we can produce another quality map with 7401 sources remaining, Figure 4.18a.

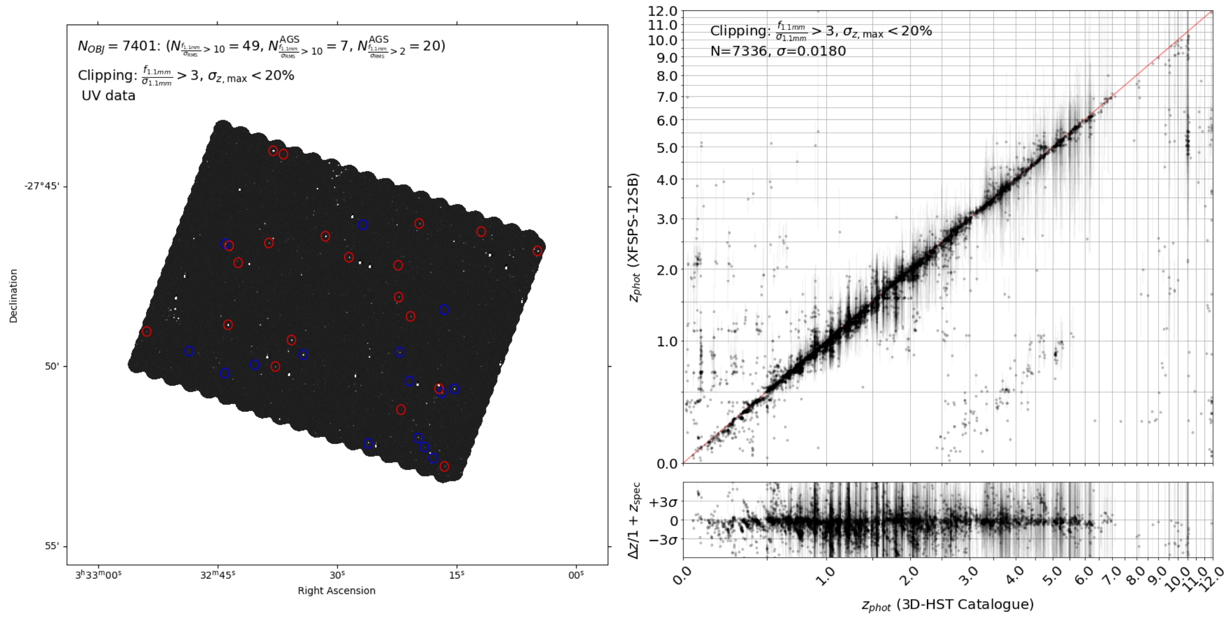

(A) (B)

FIGURE 4.18: 4.18a) Synthetic map excluding IR data clipped by $f_{1.1mm}/\sigma_{1.1mm} > 3$ and $\sigma_{z,max} < 20\%$. 4.18b) Comparison of XFSPS-12SB fits output redshift with 3D-HST catalogue redshift with $f_{1.1mm}/\sigma_{1.1mm} > 3$ and $\sigma_{z,max} < 20\%$ clipping

The photometric redshift comparison, Figure 4.18b, also has a spread, down from $\sigma = 0.0255$ to $\sigma = 0.0180$. The $\sigma_{z,max} < 20\%$ clipping does however remove 2 more AGS sources (AGS18, 24) in addition to the 5 removed by the SNR clipping.

Compared to the $N_{\frac{f_{obs}}{\sigma_{obs}}>2} > 10$ clipping, the $\sigma_{z,max} < 20\%$ increases the number of bright sources to $N_{\frac{f_{1.1mm}}{\sigma_{\rm RMS}}>10} = 49$. To prevent this undesirable increase in bright sources a last attempt was made to also include the selection criteria $N_{\frac{f_{obs}}{\sigma_{obs}}>2} > 10$. Now clipping by SNR, solid data points, and maximum redshift error ($f_{1.1mm}/\sigma_{1.1mm} > 3$, $N_{\frac{f_{obs}}{\sigma_{obs}}>2} > 10$, $\sigma_{z,max} < 20\%$), we can produce a synthetic map with fewer false sources Figure 4.19a.

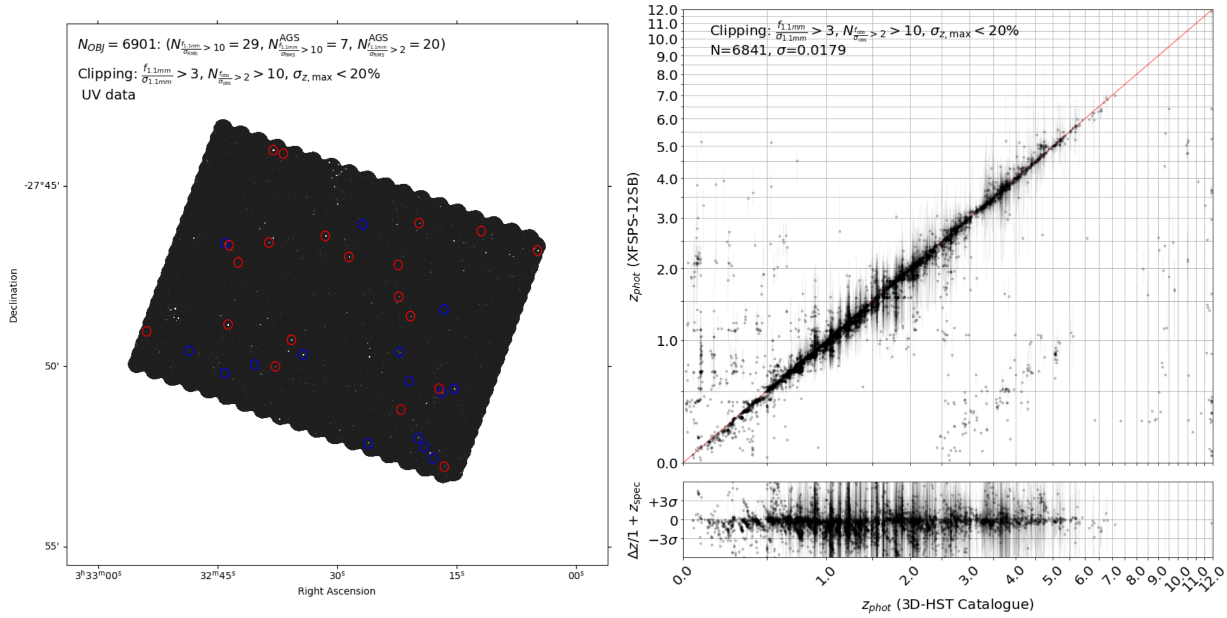

(A) (B)

FIGURE 4.19: 4.19a) Synthetic map excluding IR data clipped by $f_{1.1mm}/\sigma_{1.1mm} > 3$, $N_{\frac{f_{obs}}{\sigma_{obs}}>2} > 10$, and $\sigma_{z,max} < 20\%$. 4.19b) Comparison of XFSPS-12SB fits output redshift with 3D-HST catalogue redshift with $f_{1.1mm}/\sigma_{1.1mm} > 3$, $N_{\frac{f_{obs}}{\sigma_{obs}}>2} > 10$, and $\sigma_{z,max} < 20\%$ clipping

Still 6841 sources remain when comparing the redshifts, and the spread has also been improved to $\sigma = 0.0179$, Figure 4.19b.

The correction of the synthetic map following these three selection methods is clearly seen when comparing the mock map without any selection and with $f_{1.1mm}/\sigma_{1.1mm} > 3$, $N_{\frac{f_{obs}}{\sigma_{obs}}>2} > 10$ and $\sigma_{z,max} < 20\%$ clipping, Figure 4.20.

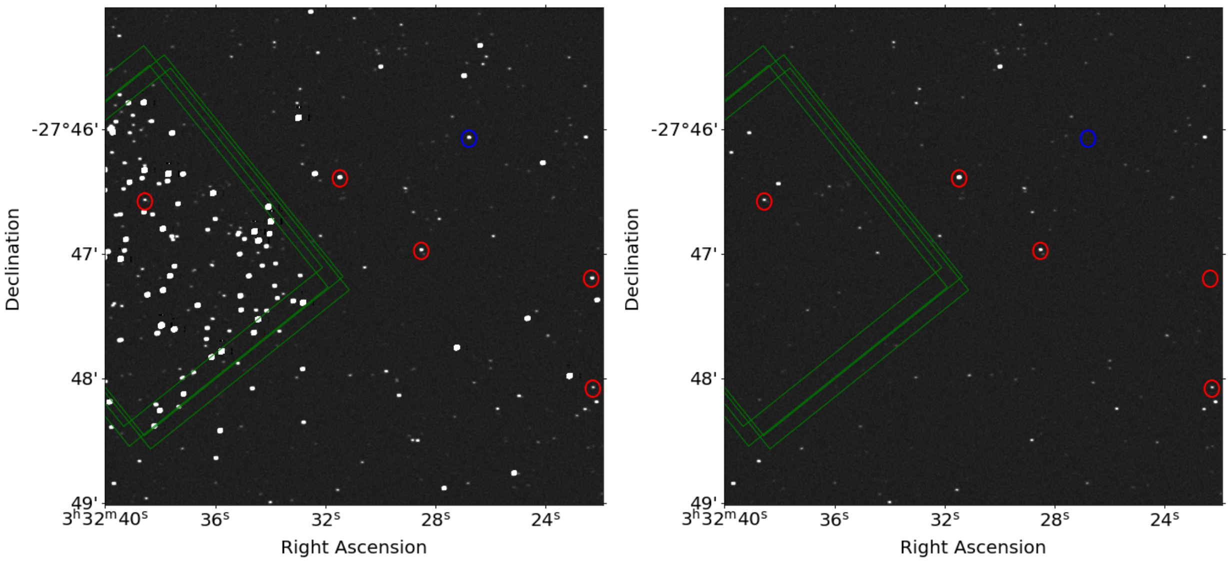

(A) (B)

FIGURE 4.20: 4.20a) A mock map close-up showing part of the HUDF region and along with 6 AGS sources before employing any selection methods. 4.20a) Close-up after employing the three selection criteria $f_{1.1mm}/\sigma_{1.1mm} > 3$, $N_{\frac{f_{obs}}{\sigma_{obs}}>2} > 10$ and $\sigma_{z,max} < 20\%$.

Though some spurious sources like the sources displayed on Figure 4.14a remain even after applying all three selection criteria, the synthetic UV-optical mock map is significantly improved under these selections.

For an easier overview of the AGS sources removed we refer to Table B.1 on Appendix B for a list of sources removed under the different selection schemes for the UV-optical synthetic map. Similarly Table B.2 on Appendix B provides the same information for the synthetic UV-optical-IR map.

A clear overview of the synthetic maps produced and the improvement of the photometric redshift on the redshift comparison plot is displayed on Figure 4.21.

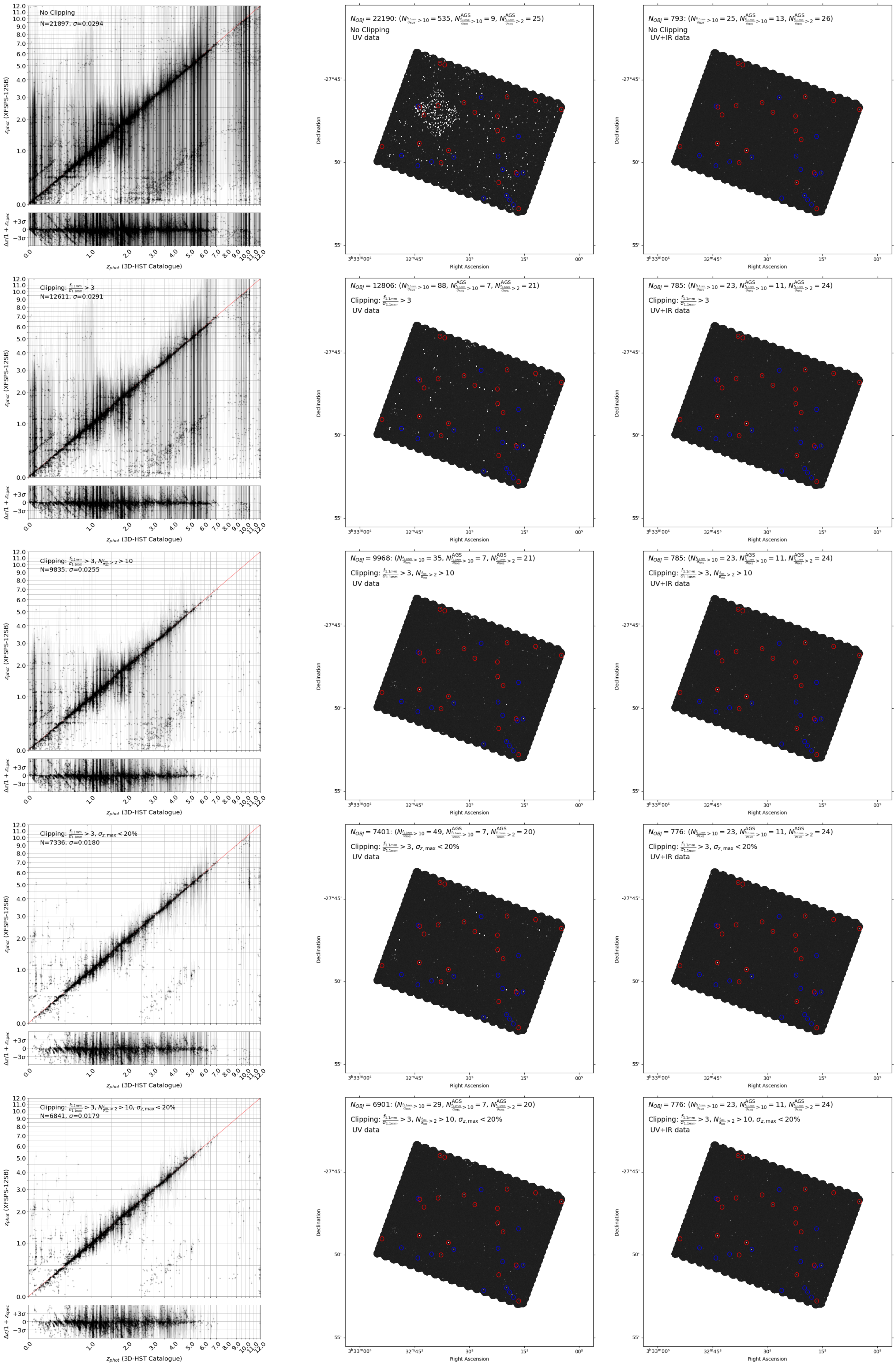

FIGURE 4.21

4.3 Chapter summary

In this chapter we have used the optimized XFSPS-12SB set of SPS models with energy balance to produce synthetic maps excluding and including IR data constraints up to the $500\mu m$ SPIRE. Following clipping criteria to exclude uncertain sources and sources with poor UV-optical data, we were able to produce reasonable maps in agreement with the GOODS-ALMA map by Gómez-Guijarro et al. in prep.

The key take-aways from this chapter is the following.

- Energy balance is able to predict the 1.1mm Universe given UV-optical-IR data up to the $500\mu m$ SPIRE band.
- Energy balance seems to also reasonably predict the FIR of the general population of galaxies in the 1.1mm Universe given only UV-optical data, with the right selection criteria to remove uncertain sources with poor UV-optical data.
- A few spurious sources are still present on the synthetic maps. Presumably due to the lack of an SPS model template with the correct red colors in the UV-optical to fit more regular galaxies rather than extremely DSFGs.

Chapter 5

Discussion

Throughout this study we have seen how imposing energy balance seems to work at reproducing the FIR SED of DSFGs when fitted with IR data (from UV-optical to 1.1mm ALMA data). If only UV-optical data is included the energy balanced fits only work for ALMA sources with compact well-aligned HST H-band counterparts. Generalizing this methodology to fit the entirety of the 69arcmin^2 GOODS-ALMA field, we find that energy balanced fits produce reasonable 1.1mm synthetic maps comparable to the real GOODS-ALMA field regardless of fitting UV-optical data or UV-optical-IR data (up to 500μm SPIRE). In this section a discussion of the strengths, weaknesses and application of this energy balancing technique carried out.

5.1 Underestimating the FIR of DSFGs

We have seen how the energy balanced fits are able to reproduce 1.1mm fluxes within a factor of 2 of the reported ALMA fluxes when given UV-optical data and IR constraints (Super-deblended and 1.1mm ALMA data). When excluding IR constraints energy balance fails at predicting the FIR SED and 1.1mm flux from just UV-optical data. While the spatial offset and morphology was identified as possible factors to this underestimation, an evaluation of the photometric redshifts was conducted to ensure that the underestimation was not due to redshift ambiguities when excluding/including IR data. However, redshift estimates were shown to be almost identical, ruling out the redshift as driver of this underestimating effect. The factor causing this underestimation of the FIR SED is still uncertain. There may be hidden systematic errors in the catalogue data, e.g. from observations in shallow IRAC channels with a large beam size weighing the SED fit down. As the fits are very sensitive to the UV-optical data, when excluding IR constraints, a small deviation or error in the catalogue data may be crucial to the FIR SED fit. It is still uncertain what causes the code to not choose the same best fit template combination regardless of fitting UV-optical or UV-optical-IR data. This leaves room for future investigations into which exact component is causing the underestimation of the FIR SED of DSFGs.

As already alluded to, the UV-optical fits are very sensitive to systematics in the UV-optical data, which poses a challenge for HST-dark sources which can easily be falsely associated contaminating the sample. The GOODS-ALMA DSFG sample catalogue used in this study contains such HST-dark galaxies (AGS4, 11, 15, 17, 24, 25 of the Franco et al. papers) which we have argued may be falsely associated with a bright neighbouring galaxy. A prime example of this is AGS15 which we found had an estimated $z_{AGS15} = 0.82^{+0.06}_{-0.039}$ while Zhou et al. 2020 [91] in a very recent follow-up study found $z^{Zhou}_{AGS15} = 3.472$ by spectral deconfusion (subtracting nearby neighbours etc.) to deblend the real H-band counterpart. Additionally, Zhou et al. were able to obtain spectroscopic redshifts $z^{Zhou}_{AGS4} = 3.556$ and $z^{Zhou}_{AGS17} = 3.467$ by identifying the CO(6-5) line. They also performed 4 million Monte Carlo simulations to determine a slim 0.4% chance of 4/6 HST-dark galaxies randomly falling into the same 5arcmin^2 area. Interestingly, Zhou et al. found 4/6 HST-dark galaxies (AGS11, 15, 17, 24) to be part of a protocluster in virialization previously identified by Franck and McGaugh 2016 [92]. Moreover, AGS24 is the most massive galaxy in the GOODS-ALMA field with no AGN and $z > 3$, suggesting it may be a candidate BCG in formation. Nevertheless, the Zhou et al. study demonstrates how confusion of sources may lead to false associations, emphasizing the need for deep high resolution data to avoid sample contamination. Such extraordinary capabilities are expected to become available with the launch and commencement of new facilities such as the JWST, which will provide high resolution data to more accurately deblend sources and avoid false associations.

5.2 Predicting the 1.1mm GOODS-ALMA map from synthetic photometry

Upon deriving an optimal template set to fit the sample of DSFGs, this set was utilized to construct a synthetic mock map comparable to the GOODS-ALMA map from Franco et al. While the clipping of uncertain sources and sources with poor UV-optical data produces reasonable maps with energy balance, a few spurious sources are still present. These spurious sources presumably arise from EAZY mistaking old optically red low-z sources for high-z dusty sources due to the two-fold dust-age degeneracy, ramping up their FIR emission and sending them to artificially high redshifts. A possible approach to deal with this misidentification would be to optimize the template set by possibly adding a template with the correct red colors in the optical to handle this type of galaxy. Another approach would be to include an additional form of prior to break this degeneracy, however this is not possible in the current version of EAZY.

With software and computational methods being a central aspect of this study, I have also discovered the importance of a cautious approach to numerical results, as hidden coding bugs may falsely alter the output. An example of this was found in EAZY version 0.2.0-48-gf9540fb where a bug with the template error function was affecting the output SED by producing negative fluxes when extrapolated to long infrared wavelengths. This bug was patched, but it remains a reminder of the necessity of a cautious approach, as is required with any other software like EAZY in constant development.

Chapter 6

Conclusion

With the inception of this project, the central question we sought to answer was whether the principle of energy balance was valid for DSFGs, and if it could be applied to predict their FIR SED from UV-optical data. To tackle this issue a test sample of DSFGs from a recent 69arcmin^2 1.1mm GOODS-ALMA survey was utilized to fit SEDs and optimize SPS models to be representative of this galaxy type. The resulting SED fits produced by the optimized XFSPS-12SB set found that energy balance could indeed be imposed to reproduce the FIR SED when fitting UV-optical-IR data. When IR constraints were excluded energy balance showed a systematic underestimation of the FIR SED for the majority of the sample DSFGs. Only a small fraction of sources had their FIR SED successfully predicted by fits with UV-optical data. These successful sources had compact HST H-band counterparts and co-spatial 1.1mm ALMA dust emission.

Using the XFSPS-12SB energy balanced template set a pair of synthetic 1.1mm maps were produced to compare with the observed GOODS-ALMA field. Excluding uncertain catalogue sources with poor UV-optical data, we were able to produce synthetic maps in agreement with the GOODS-ALMA field in both cases when fitting UV-optical data and UV-optical-IR (up to 500μm SPIRE) data. This implied that the energy balance principle works reasonably when also fitting more regular galaxies compared to the extremely DSFGs of the test sample. However a few spurious sources still remained and we argued that another optimization of the template set could be conducted to include a template with the correct red colors in the UV-optical for optically red low-z galaxies such that they are not mistaken for dusty high-z galaxies.

To summarize the key findings of this study.

- Energy balance is not able to predict the FIR SED of DSFGs in the absence of IR constraints, with the exception of sources where the 1.1mm ALMA dust emission and HST H-band counterpart are co-spatial and the morphology of the H-band counterpart is compact.

- In the presence of IR data (Super-deblended and 1.1mm ALMA), energy balance is able to reasonably reproduce the FIR SED.
- The factor causing the underestimation of the FIR SED when comparing fits with only UV-optical data and UV-optical-IR data (Super-deblended and 1.1mm ALMA) is not a redshift degeneracy, but rather a hidden systematic in the data or code.
- Upon generation of synthetic GOODS-ALMA maps it seems that the general population of galaxies is well-fit, successfully reproducing the FIR Universe when imposing the energy balance principle. This implies that it is possibly just the extreme cases of DSFGs that strongly challenge this approach.

Throughout the progression of this study we have effectively optimized the SPS models to make them more representative of the DSFG type, thus assisting the EAZY photometric redshift code and its ability to produce high quality SEDs to infer the properties of DSFGs, and essentially predict the FIR Universe.

Upon future improvements such as optimizing the SPS models to mitigate the underprediction of the FIR SED when fitting UV-optical data, this methodology could have many useful applications. The new procedure presented in this thesis could potentially be used to facilitate the discovery of new dusty star forming galaxies predicted from large-scale cosmological surveys by upcoming facilities. This could essentially be used to infer the properties of DSFGs in bulk to constrain the cosmic star formation history helping us understand the Universe as a whole.

Bibliography

[1] Peter Schneider. *Extragalactic Astronomy and Cosmology: An Introduction*. 2015. DOI: 10.1007/978-3-642-54083-7.

[2] K. G. Noeske et al. "Star Formation in AEGIS Field Galaxies since z=1.1: The Dominance of Gradually Declining Star Formation, and the Main Sequence of Star-forming Galaxies". In: *The Astrophysical Journal, Letters* 660.1 (May 2007), pp. L43–L46. DOI: 10.1086/517926. arXiv: astro-ph/0701924 [astro-ph].

[3] J. S. Speagle et al. "A Highly Consistent Framework for the Evolution of the Star-Forming "Main Sequence" from $z \sim 0 - 6$". In: *The Astrophysical Journal, Supplement* 214.2, 15 (Oct. 2014), p. 15. DOI: 10.1088/0067-0049/214/2/15. arXiv: 1405.2041 [astro-ph.GA].

[4] Romeel Davé, Kristian Finlator, and Benjamin D. Oppenheimer. "An analytic model for the evolution of the stellar, gas and metal content of galaxies". In: *Monthly Notices of the Royal Astronomical Society* 421.1 (Mar. 2012), pp. 98–107. DOI: 10.1111/j.1365-2966.2011.20148.x. arXiv: 1108.0426 [astro-ph.CO].

[5] T. R. Greve et al. "An interferometric CO survey of luminous submillimetre galaxies". In: *Monthly Notices of the Royal Astronomical Society* 359.3 (May 2005), pp. 1165–1183. DOI: 10.1111/j.1365-2966.2005.08979.x. arXiv: astro-ph/0503055 [astro-ph].

[6] N. Scoville et al. "ISM Masses and the Star formation Law at Z = 1 to 6: ALMA Observations of Dust Continuum in 145 Galaxies in the COSMOS Survey Field". In: *The Astrophysical Journal* 820.2, 83 (Apr. 2016), p. 83. DOI: 10.3847/0004-637X/820/2/83. arXiv: 1511.05149 [astro-ph.GA].

[7] Edwin E. Salpeter. "The Luminosity Function and Stellar Evolution." In: *The Astrophysical Journal* 121 (Jan. 1955), p. 161. DOI: 10.1086/145971.

[8] Pavel Kroupa. "On the variation of the initial mass function". In: *Monthly Notices of the Royal Astronomical Society* 322.2 (Apr. 2001), pp. 231–246. DOI: 10.1046/j.1365-8711.2001.04022.x. arXiv: astro-ph/0009005 [astro-ph].

[9] Casey Papovich, Mark Dickinson, and Henry C. Ferguson. "The Stellar Populations and Evolution of Lyman Break Galaxies". In: *The Astrophysical Journal* 559.2 (Oct. 2001), pp. 620–653. DOI: 10.1086/322412. arXiv: astro-ph/0105087 [astro-ph].

[10] Romeel Davé, Kristian Finlator, and Benjamin D. Oppenheimer. "An analytic model for the evolution of the stellar, gas and metal content of galaxies". In: *Monthly Notices of the Royal Astronomical Society* 421.1 (Mar. 2012), pp. 98–107. DOI: 10.1111/j.1365-2966.2011.20148.x. arXiv: 1108.0426 [astro-ph.CO].

[11] Caitlin M. Casey, Desika Narayanan, and Asantha Cooray. "Dusty star-forming galaxies at high redshift". In: *Physics Reports* 541.2 (Aug. 2014), pp. 45–161. DOI: 10.1016/j.physrep.2014.02.009. arXiv: 1402.1456 [astro-ph.CO].

[12] Piero Madau and Mark Dickinson. "Cosmic Star-Formation History". In: *Annual Review of Astronomy & Astrophysics* 52 (Aug. 2014), pp. 415–486. DOI: 10.1146/annurev-astro-081811-125615. arXiv: 1403.0007 [astro-ph.CO].

[13] Peter S. Behroozi, Risa H. Wechsler, and Charlie Conroy. "The Average Star Formation Histories of Galaxies in Dark Matter Halos from z = 0-8". In: *The Astrophysical Journal* 770.1, 57 (June 2013), p. 57. DOI: 10.1088/0004-637X/770/1/57. arXiv: 1207.6105 [astro-ph.CO].

[14] Charles C. Steidel and Donald Hamilton. "Deep Imaging of redshift QSO Fields Below the Lyman Limit. I. The Field of Q0000-263 and galaxies at z= 3.4". In: *The Astronomical Journal* 104 (Sept. 1992), p. 941. DOI: 10.1086/116287.

[15] M. Dickinson. "Color-Selected High Redshift Galaxies and the HDF". In: *The Hubble Deep Field*. Ed. by Mario Livio, S. Michael Fall, and Piero Madau. Oct. 1998, p. 219. arXiv: astro-ph/9802064 [astro-ph].

[16] Gabriel B. Brammer, Pieter G. van Dokkum, and Paolo Coppi. "EAZY: A Fast, Public Photometric Redshift Code". In: *The Astrophysical Journal* 686.2 (Oct. 2008), pp. 1503–1513. DOI: 10.1086/591786. arXiv: 0807.1533 [astro-ph].

[17] M. Negrello et al. "Photometric redshift accuracy in AKARI deep surveys". In: *Monthly Notices of the Royal Astronomical Society* 394.1 (Mar. 2009), pp. 375–397. DOI: 10.1111/j.1365-2966.2008.14293.x. arXiv: 0811.4158 [astro-ph].

[18] Jakob Walcher et al. "Fitting the integrated spectral energy distributions of galaxies". In: *Astrophysics & Space Science* 331 (Jan. 2011), pp. 1–52. DOI: 10.1007/s10509-010-0458-z. arXiv: 1008.0395 [astro-ph.CO].

[19] Andrew W. Blain et al. "Submillimeter galaxies". In: *Physics Reports* 369.2 (Oct. 2002), pp. 111–176. DOI: 10.1016/S0370-1573(02)00134-5. arXiv: astro-ph/0202228 [astro-ph].

[20] Ian Smail, R. J. Ivison, and A. W. Blain. "A Deep Sub-millimeter Survey of Lensing Clusters: A New Window on Galaxy Formation and Evolution". In: *The Astrophysical Journal, Letters* 490.1 (Nov. 1997), pp. L5–L8. DOI: 10.1086/311017. arXiv: astro-ph/9708135 [astro-ph].

[21] David H. Hughes et al. "High-redshift star formation in the Hubble Deep Field revealed by a submillimetre-wavelength survey". In: *Nature* 394.6690 (July 1998), pp. 241–247. DOI: 10.1038/28328. arXiv: astro-ph/9806297 [astro-ph].

[22] W. S. Holland et al. "SCUBA: a common-user submillimetre camera operating on the James Clerk Maxwell Telescope". In: *Monthly Notices of the Royal Astronomical Society* 303.4 (Mar. 1999), pp. 659–672. DOI: 10.1046/j.1365-8711.1999.02111.x. arXiv: astro-ph/9809122 [astro-ph].

[23] Hai Fu et al. "The rapid assembly of an elliptical galaxy of 400 billion solar masses at a redshift of 2.3". In: *Nature* 498.7454 (June 2013), pp. 338–341. DOI: 10.1038/nature12184. arXiv: 1305.4930 [astro-ph.CO].

[24] J. A. Hodge et al. "Kiloparsec-scale Dust Disks in High-redshift Luminous Submillimeter Galaxies". In: *The Astrophysical Journal* 833.1, 103 (Dec. 2016), p. 103. DOI: 10.3847/1538-4357/833/1/103. arXiv: 1609.09649 [astro-ph.GA].

[25] C. Gómez-Guijarro et al. "Starburst to Quiescent from HST/ALMA: Stars and Dust Unveil Minor Mergers in Submillimeter Galaxies at $z \sim 4.5$". In: *The Astrophysical Journal* 856.2, 121 (Apr. 2018), p. 121. DOI: 10.3847/1538-4357/aab206. arXiv: 1802.07751 [astro-ph.GA].

[26] Daniela Calzetti et al. "The Dust Content and Opacity of Actively Star-forming Galaxies". In: *The Astrophysical Journal* 533.2 (Apr. 2000), pp. 682–695. DOI: 10.1086/308692. arXiv: astro-ph/9911459 [astro-ph].

[27] R. J. McLure et al. "Dust attenuation in $2 < z < 3$ star-forming galaxies from deep ALMA observations of the Hubble Ultra Deep Field". In: *Monthly Notices of the Royal Astronomical Society* 476.3 (May 2018), pp. 3991–4006. DOI: 10.1093/mnras/sty522. arXiv: 1709.06102 [astro-ph.GA].

[28] E. da Cunha et al. "An ALMA Survey of Sub-millimeter Galaxies in the Extended Chandra Deep Field South: Physical Properties Derived from Ultraviolet-to-radio Modeling". In: *The Astrophysical Journal* 806.1, 110 (June 2015), p. 110. DOI: 10.1088/0004-637X/806/1/110. arXiv: 1504.04376 [astro-ph.GA].

[29] D. Elbaz et al. "Starbursts in and out of the star-formation main sequence". In: *Astronomy & Astrophysics* 616, A110 (Aug. 2018), A110. DOI: 10.1051/0004-6361/201732370. arXiv: 1711.10047 [astro-ph.GA].

[30] Jr. Kennicutt Robert C. "The Global Schmidt Law in Star-forming Galaxies". In: *The Astrophysical Journal* 498.2 (May 1998), pp. 541–552. DOI: 10.1086/305588. arXiv: astro-ph/9712213 [astro-ph].

[31] E. Daddi et al. "A New Photometric Technique for the Joint Selection of Star-forming and Passive Galaxies at 1.4 $\lesssim z \lesssim$ 2.5". In: *The Astrophysical Journal* 617.2 (Dec. 2004), pp. 746–764. DOI: 10.1086/425569. arXiv: astro-ph/0409041 [astro-ph].

[32] W. Rujopakarn et al. "ALMA 200 pc Resolution Imaging of Smooth Cold Dusty Disks in Typical $z \sim 3$ Star-forming Galaxies". In: *The Astrophysical Journal* 882.2, 107 (Sept. 2019), p. 107. DOI: 10.3847/1538-4357/ab3791. arXiv: 1904.04507 [astro-ph.GA].

[33] D. B. Sanders et al. "Ultraluminous Infrared Galaxies and the Origin of Quasars". In: *The Astrophysical Journal* 325 (Feb. 1988), p. 74. DOI: 10.1086/165983.

[34] Philip F. Hopkins et al. "A Cosmological Framework for the Co-Evolution of Quasars, Supermassive Black Holes, and Elliptical Galaxies. I. Galaxy Mergers and Quasar Activity". In: *The Astrophysical Journal, Supplement* 175.2 (Apr. 2008), pp. 356–389. DOI: 10.1086/524362. arXiv: 0706.1243 [astro-ph].

[35] S. Toft et al. "Submillimeter Galaxies as Progenitors of Compact Quiescent Galaxies". In: *The Astrophysical Journal* 782.2, 68 (Feb. 2014), p. 68. DOI: 10.1088/0004-637X/782/2/68. arXiv: 1401.1510 [astro-ph.GA].

[36] Andrew W. Blain et al. "WISE Detections of Known QSOs at Redshifts Greater than Six". In: *The Astrophysical Journal* 778.2, 113 (Dec. 2013), p. 113. DOI: 10.1088/0004-637X/778/2/113. arXiv: 1310.2301 [astro-ph.CO].

[37] E. Daddi et al. "Multiwavelength Study of Massive Galaxies at $z \sim 2$. II. Widespread Compton-thick Active Galactic Nuclei and the Concurrent Growth of Black Holes and Bulges". In: *The Astrophysical Journal* 670.1 (Nov. 2007), pp. 173–189. DOI: 10.1086/521820. arXiv: 0705.2832 [astro-ph].

[38] M. Franco et al. "GOODS-ALMA: 1.1 mm galaxy survey. I. Source catalog and optically dark galaxies". In: *Astronomy & Astrophysics* 620, A152 (Dec. 2018), A152. DOI: 10.1051/0004-6361/201832928. arXiv: 1803.00157 [astro-ph.GA].

[39] M. Franco et al. "GOODS-ALMA: Using IRAC and VLA to probe fainter millimeter galaxies". In: *arXiv e-prints*, arXiv:2005.03040 (May 2020), arXiv:2005.03040. arXiv: 2005.03040 [astro-ph.GA].

[40] M. Franco et al. "GOODS-ALMA: The slow downfall of star-formation in z = 2-3 massive galaxies". In: *arXiv e-prints*, arXiv:2005.03043 (May 2020), arXiv:2005.03043. arXiv: 2005.03043 [astro-ph.GA].

[41] Edwin Hubble. "A Relation between Distance and Radial Velocity among Extra-Galactic Nebulae". In: *Proceedings of the National Academy of Science* 15.3 (Mar. 1929), pp. 168–173. DOI: 10.1073/pnas.15.3.168.

[42] Daniel W. Weedman. *Quasar astronomy*. 1986.

[43] Subrahmanyan Chandrasekhar. *Radiative transfer.* 1950.

[44] Samir Salim and Desika Narayanan. "The Dust Attenuation Law in Galaxies". In: *arXiv e-prints*, arXiv:2001.03181 (Jan. 2020), arXiv:2001.03181. arXiv: 2001.03181 [astro-ph.GA].

[45] Theodore P. Stecher. "Interstellar Extinction in the Ultraviolet." In: *The Astrophysical Journal* 142 (Nov. 1965), p. 1683. DOI: 10.1086/148462.

[46] Karl D. Gordon, Daniela Calzetti, and Adolf N. Witt. "Dust in Starburst Galaxies". In: *The Astrophysical Journal* 487.2 (Oct. 1997), pp. 625–635. DOI: 10.1086/304654. arXiv: astro-ph/9705043 [astro-ph].

[47] Adolf N. Witt and Karl D. Gordon. "Multiple Scattering in Clumpy Media. II. Galactic Environments". In: *The Astrophysical Journal* 528.2 (Jan. 2000), pp. 799–816. DOI: 10.1086/308197. arXiv: astro-ph/9907342 [astro-ph].

[48] Naveen A. Reddy et al. "The MOSDEF Survey: Measurements of Balmer Decrements and the Dust Attenuation Curve at Redshifts z = 1.4-2.6". In: *The Astrophysical Journal* 806.2, 259 (June 2015), p. 259. DOI: 10.1088/0004-637X/806/2/259. arXiv: 1504.02782 [astro-ph.GA].

[49] V. Buat et al. "GOODS-Herschel: dust attenuation properties of UV selected high redshift galaxies". In: *Astronomy & Astrophysics* 545, A141 (Sept. 2012), A141. DOI: 10.1051/0004-6361/201219405. arXiv: 1207.3528 [astro-ph.CO].

[50] Mariska Kriek and Charlie Conroy. "The Dust Attenuation Law in Distant Galaxies: Evidence for Variation with Spectral Type". In: *The Astrophysical Journal, Letters* 775.1, L16 (Sept. 2013), p. L16. DOI: 10.1088/2041-8205/775/1/L16. arXiv: 1308.1099 [astro-ph.CO].

[51] Rik J. Williams et al. "Detection of Quiescent Galaxies in a Bicolor Sequence from z = 0-2". In: *The Astrophysical Journal* 691.2 (Feb. 2009), pp. 1879–1895. DOI: 10.1088/0004-637X/691/2/1879. arXiv: 0806.0625 [astro-ph].

[52] B. Luo et al. "The Chandra Deep Field-South Survey: 7 Ms Source Catalogs". In: *The Astrophysical Journal, Supplement* 228.1, 2 (Jan. 2017), p. 2. DOI: 10.3847/1538-4365/228/1/2. arXiv: 1611.03501 [astro-ph.GA].

[53] Charlie Conroy. "Modeling the Panchromatic Spectral Energy Distributions of Galaxies". In: *Annual Review of Astronomy & Astrophysics* 51.1 (Aug. 2013), pp. 393–455. DOI: 10.1146/annurev-astro-082812-141017. arXiv: 1301.7095 [astro-ph.CO].

[54] Charlie Conroy, James E. Gunn, and Martin White. "The Propagation of Uncertainties in Stellar Population Synthesis Modeling. I. The Relevance of Uncertain Aspects of Stellar Evolution and the Initial Mass Function to the Derived Physical Properties of Galaxies". In: *The Astrophysical Journal* 699.1 (July 2009), pp. 486–506. DOI: 10.1088/0004-637X/699/1/486. arXiv: 0809.4261 [astro-ph].

[55] Charlie Conroy and James E. Gunn. "The Propagation of Uncertainties in Stellar Population Synthesis Modeling. III. Model Calibration, Comparison, and Evaluation". In: *The Astrophysical Journal* 712.2 (Apr. 2010), pp. 833–857. DOI: 10.1088/0004-637X/712/2/833. arXiv: 0911.3151 [astro-ph.CO].

[56] D. Burgarella, V. Buat, and J. Iglesias-Páramo. "Star formation and dust attenuation properties in galaxies from a statistical ultraviolet-to-far-infrared analysis". In: *Monthly Notices of the Royal Astronomical Society* 360.4 (July 2005), pp. 1413–1425. DOI: 10.1111/j.1365-2966.2005.09131.x. arXiv: astro-ph/0504434 [astro-ph].

[57] S. Noll et al. "Analysis of galaxy spectral energy distributions from far-UV to far-IR with CIGALE: studying a SINGS test sample". In: *Astronomy & Astrophysics* 507.3 (Dec. 2009), pp. 1793–1813. DOI: 10.1051/0004-6361/200912497. arXiv: 0909.5439 [astro-ph.CO].

[58] M. Boquien et al. "CIGALE: a python Code Investigating GALaxy Emission". In: *Astronomy & Astrophysics* 622, A103 (Feb. 2019), A103. DOI: 10.1051/0004-6361/201834156. arXiv: 1811.03094 [astro-ph.GA].

[59] G. Bruzual and S. Charlot. "Stellar population synthesis at the resolution of 2003". In: *Monthly Notices of the Royal Astronomical Society* 344.4 (Oct. 2003), pp. 1000–1028. DOI: 10.1046/j.1365-8711.2003.06897.x. arXiv: astro-ph/0309134 [astro-ph].

[60] B. T. Draine et al. "Andromeda's Dust". In: *The Astrophysical Journal* 780.2, 172 (Jan. 2014), p. 172. DOI: 10.1088/0004-637X/780/2/172. arXiv: 1306.2304 [astro-ph.CO].

[61] Min S. Yun, Naveen A. Reddy, and J. J. Condon. "Radio Properties of Infrared-selected Galaxies in the IRAS 2 Jy Sample". In: *The Astrophysical Journal* 554.2 (June 2001), pp. 803–822. DOI: 10.1086/323145. arXiv: astro-ph/0102154 [astro-ph].

[62] C. Schreiber et al. "Dust temperature and mid-to-total infrared color distributions for star-forming galaxies at $0 < z < 4$". In: *Astronomy & Astrophysics* 609, A30 (Jan. 2018), A30. DOI: 10.1051/0004-6361/201731506. arXiv: 1710.10276 [astro-ph.GA].

[63] J. R. Mullaney et al. "Defining the intrinsic AGN infrared spectral energy distribution and measuring its contribution to the infrared output of composite galaxies". In: *Monthly Notices of the Royal Astronomical Society* 414.2 (June 2011), pp. 1082–1110. DOI: 10.1111/j.1365-2966.2011.18448.x. arXiv: 1102.1425 [astro-ph.CO].

[64] Allison Kirkpatrick et al. "The Role of Star Formation and an AGN in Dust Heating of z = 0.3-2.8 Galaxies. I. Evolution with Redshift and Luminosity". In: *The Astrophysical Journal* 814.1, 9 (Nov. 2015), p. 9. DOI: 10.1088/0004-637X/814/1/9. arXiv: 1510.02806 [astro-ph.GA].

[65] C. M. Casey et al. "A Population of $z > 2$ Far-infrared Herschel-SPIRE-selected Starbursts". In: *The Astrophysical Journal* 761.2, 139 (Dec. 2012), p. 139. DOI: 10.1088/0004-637X/761/2/139. arXiv: 1210.4932 [astro-ph.CO].

[66] David A. Neufeld. "The Escape of Lyman-Alpha Radiation from a Multiphase Interstellar Medium". In: *The Astrophysical Journal, Letters* 370 (Apr. 1991), p. L85. DOI: 10.1086/185983.

[67] Gregory Rudnick et al. "A K-band-Selected Photometric Redshift Catalog in the Hubble Deep Field South: Sampling the Rest-Frame V Band to z =3". In: *The Astronomical Journal* 122.5 (Nov. 2001), pp. 2205–2221. DOI: 10.1086/323542. arXiv: astro-ph/0106074 [astro-ph].

[68] Fei Sha et al. "Multiplicative Updates for Nonnegative Quadratic Programming". In: *Neural Computation* 19.8 (2007), pp. 2004–2031. DOI: 10.1162/neco.2007.19.8.2004. eprint: https://doi.org/10.1162/neco.2007.19.8.2004. URL: https://doi.org/10.1162/neco.2007.19.8.2004.

[69] M. Nonino et al. "Deep U Band and R Imaging of Goods-South: Observations, Data Reduction and First Results". In: *The Astrophysical Journal, Supplement* 183.2 (Aug. 2009), pp. 244–260. DOI: 10.1088/0067-0049/183/2/244. arXiv: 0906.4250 [astro-ph.CO].

[70] H. Hildebrandt et al. "GaBoDS: The Garching-Bonn Deep Survey. V. Data release of the ESO Deep-Public-Survey". In: *Astronomy & Astrophysics* 452.3 (June 2006), pp. 1121–1128. DOI: 10.1051/0004-6361:20054278. arXiv: astro-ph/0509882 [astro-ph].

[71] T. Erben et al. "GaBoDS: The Garching-Bonn Deep Survey. IV. Methods for the image reduction of multi-chip cameras demonstrated on data from the ESO Wide-Field Imager". In: *Astronomische Nachrichten* 326.6 (July 2005), pp. 432–464. DOI: 10.1002/asna.200510396. arXiv: astro-ph/0501144 [astro-ph].

[72] Carolin N. Cardamone et al. "The Multiwavelength Survey by Yale-Chile (MUSYC): Deep Medium-band Optical Imaging and High-quality 32-band Photometric Redshifts in the ECDF-S". In: *The Astrophysical Journal, Supplement* 189.2 (Aug. 2010), pp. 270–285. DOI: 10.1088/0067-0049/189/2/270. arXiv: 1008.2974 [astro-ph.CO].

[73] M. Giavalisco et al. "The Great Observatories Origins Deep Survey: Initial Results from Optical and Near-Infrared Imaging". In: *The Astrophysical Journal, Letters* 600.2 (Jan. 2004), pp. L93–L98. DOI: 10.1086/379232. arXiv: astro-ph/0309105 [astro-ph].

[74] Anton M. Koekemoer et al. "CANDELS: The Cosmic Assembly Near-infrared Deep Extragalactic Legacy Survey—The Hubble Space Telescope Observations, Imaging Data Products, and Mosaics". In: *The Astrophysical Journal, Supplement* 197.2, 36 (Dec. 2011), p. 36. DOI: 10.1088/0067-0049/197/2/36. arXiv: 1105.3754 [astro-ph.CO].

[75] J. Retzlaff et al. "The Great Observatories Origins Deep Survey. VLT/ISAAC near-infrared imaging of the GOODS-South field". In: *Astronomy & Astrophysics* 511, A50 (Feb. 2010), A50. DOI: 10.1051/0004-6361/200912940. arXiv: 0912.1306 [astro-ph.CO].

[76] Stijn Wuyts et al. "FIREWORKS U_{38}-to-24 μm Photometry of the GOODS Chandra Deep Field-South: Multiwavelength Catalog and Total Infrared Properties of Distant K_s-selected Galaxies". In: *The Astrophysical Journal* 682.2 (Aug. 2008), pp. 985–1003. DOI: 10.1086/588749.

[77] Bau-Ching Hsieh et al. "The Taiwan ECDFS Near-Infrared Survey: Ultra-deep J and K_S Imaging in the Extended Chandra Deep Field-South". In: *The Astrophysical Journal, Supplement* 203.2, 23 (Dec. 2012), p. 23. DOI: 10.1088/0067-0049/203/2/23. arXiv: 1210.4519 [astro-ph.CO].

[78] Gabriel B. Brammer et al. "3D-HST: A Wide-field Grism Spectroscopic Survey with the Hubble Space Telescope". In: *The Astrophysical Journal, Supplement* 200.2, 13 (June 2012), p. 13. DOI: 10.1088/0067-0049/200/2/13. arXiv: 1204.2829 [astro-ph.CO].

[79] Norman A. Grogin et al. "CANDELS: The Cosmic Assembly Near-infrared Deep Extragalactic Legacy Survey". In: *The Astrophysical Journal, Supplement* 197.2, 35 (Dec. 2011), p. 35. DOI: 10.1088/0067-0049/197/2/35. arXiv: 1105.3753 [astro-ph.CO].

[80] M. L. N. Ashby et al. "SEDS: The Spitzer Extended Deep Survey. Survey Design, Photometry, and Deep IRAC Source Counts". In: *The Astrophysical Journal* 769.1, 80 (May 2013), p. 80. DOI: 10.1088/0004-637X/769/1/80.

[81] M. B. Taylor. "TOPCAT & STIL: Starlink Table/VOTable Processing Software". In: *Astronomical Data Analysis Software and Systems XIV*. Ed. by P. Shopbell, M. Britton, and R. Ebert. Vol. 347. Astronomical Society of the Pacific Conference Series. Dec. 2005, p. 29.

[82] Piero Madau. "Radiative Transfer in a Clumpy Universe: The Colors of High-Redshift Galaxies". In: *The Astrophysical Journal* 441 (Mar. 1995), p. 18. DOI: 10.1086/175332.

[83] Michael R. Blanton and Sam Roweis. "K-Corrections and Filter Transformations in the Ultraviolet, Optical, and Near-Infrared". In: *The Astronomical Journal* 133.2 (Feb. 2007), pp. 734–754. DOI: 10.1086/510127. arXiv: astro-ph/0606170 [astro-ph].

[84] Rosalind E. Skelton et al. "3D-HST WFC3-selected Photometric Catalogs in the Five CANDELS/3D-HST Fields: Photometry, Photometric Redshifts, and Stellar Masses". In: *The Astrophysical Journal, Supplement* 214.2, 24 (Oct. 2014), p. 24. DOI: 10.1088/0067-0049/214/2/24. arXiv: 1403.3689 [astro-ph.GA].

[85] Shuowen Jin et al. ""Super-deblended" Dust Emission in Galaxies. II. Far-IR to (Sub)millimeter Photometry and High-redshift Galaxy Candidates in the Full COSMOS Field". In: *The Astrophysical Journal* 864.1, 56 (Sept. 2018), p. 56. DOI: 10.3847/1538-4357/aad4af. arXiv: 1807.04697 [astro-ph.GA].

[86] Nell Byler et al. "Nebular Continuum and Line Emission in Stellar Population Synthesis Models". In: *The Astrophysical Journal* 840.1, 44 (May 2017), p. 44. DOI: 10.3847/1538-4357/aa6c66. arXiv: 1611.08305 [astro-ph.GA].

[87] J. Maíz Apellániz. "A Recalibration of Optical Photometry: Tycho-2, Strömgren, and Johnson Systems". In: *The Astronomical Journal* 131.2 (Feb. 2006), pp. 1184–1199. DOI: 10.1086/499158. URL: https://doi.org/10.1086%2F499158.

[88] Georgios E. Magdis et al. "The Evolving Interstellar Medium of Star-forming Galaxies since z = 2 as Probed by Their Infrared Spectral Energy Distributions". In: *The Astrophysical Journal* 760.1, 6 (Nov. 2012), p. 6. DOI: 10.1088/0004-637X/760/1/6. arXiv: 1210.1035 [astro-ph.CO].

[89] B. T. Draine and Aigen Li. "Infrared Emission from Interstellar Dust. IV. The Silicate-Graphite-PAH Model in the Post-Spitzer Era". In: *The Astrophysical Journal* 657.2 (Mar. 2007), pp. 810–837. DOI: 10.1086/511055. arXiv: astro-ph/0608003 [astro-ph].

[90] H. A. Flewelling et al. "The Pan-STARRS1 Database and Data Products". In: *arXiv e-prints*, arXiv:1612.05243 (Dec. 2016), arXiv:1612.05243. arXiv: 1612.05243 [astro-ph.IM].

[91] L. Zhou et al. "GOODS-ALMA: Optically dark ALMA galaxies shed light on a cluster in formation at z = 3.5". In: *arXiv e-prints*, arXiv:2008.08518 (Aug. 2020), arXiv:2008.08518. arXiv: 2008.08518 [astro-ph.GA].

[92] J. R. Franck and S. S. McGaugh. "The Candidate Cluster and Protocluster Catalog (CCPC) of Spectroscopically Identified Structures Spanning 2.74 < z < 3.71". In: *The Astrophysical Journal* 817.2, 158 (Feb. 2016), p. 158. DOI: 10.3847/0004-637X/817/2/158. arXiv: 1512.04956 [astro-ph.GA].

[93] M. Compiègne et al. "The global dust SED: tracing the nature and evolution of dust with DustEM". In: *Astronomy & Astrophysics* 525, A103 (Jan. 2011), A103. DOI: 10.1051/0004-6361/201015292. arXiv: 1010.2769 [astro-ph.GA].

Appendix A

SED quality control

A.1 XFSPS-12O

The quality of the SED fitting improves when including additional infrared Super-deblended and ALMA 1.1mm data to the fit. However, a slight shift and a gap between model and observations is still present when fitting with the default XFSPS-12O.

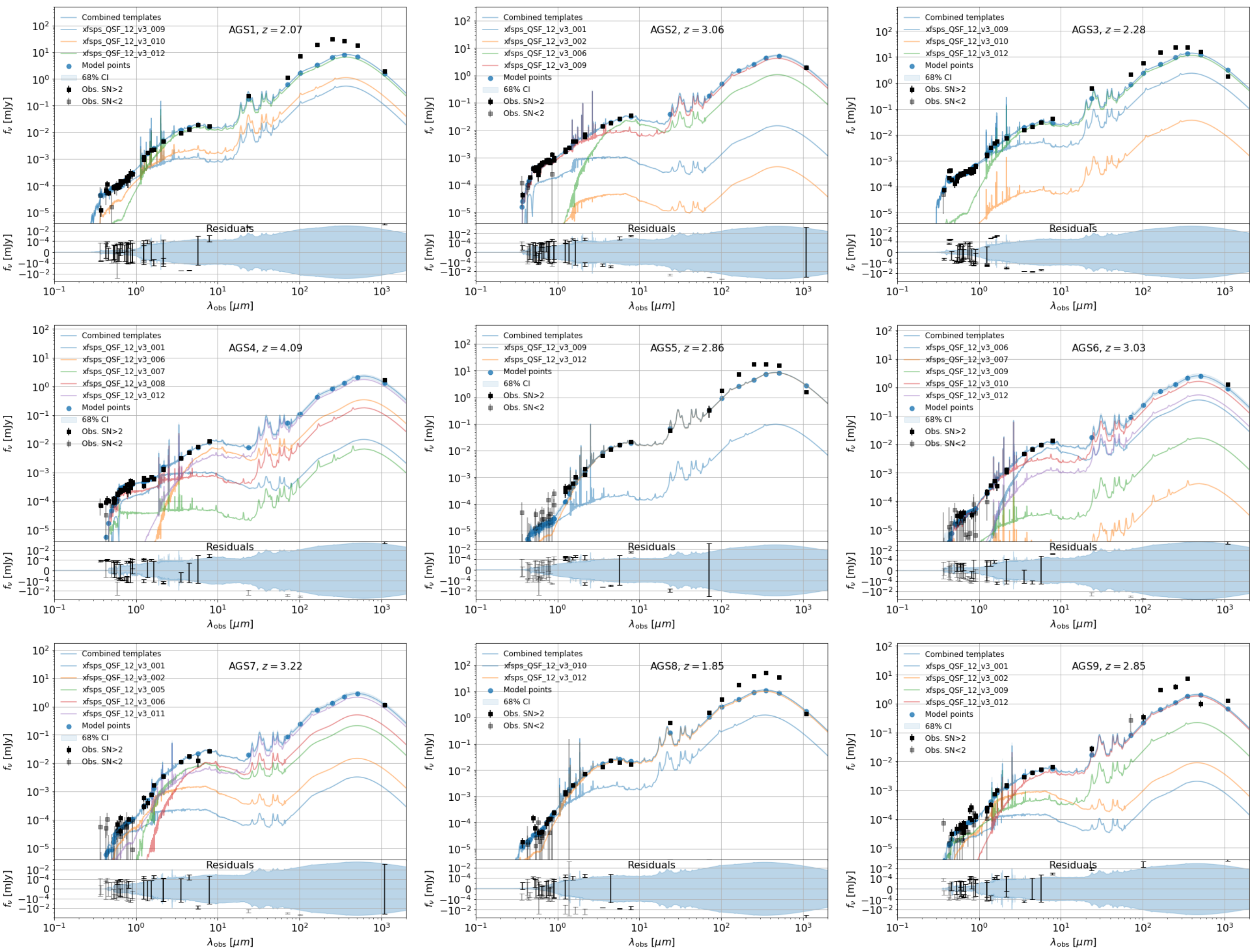

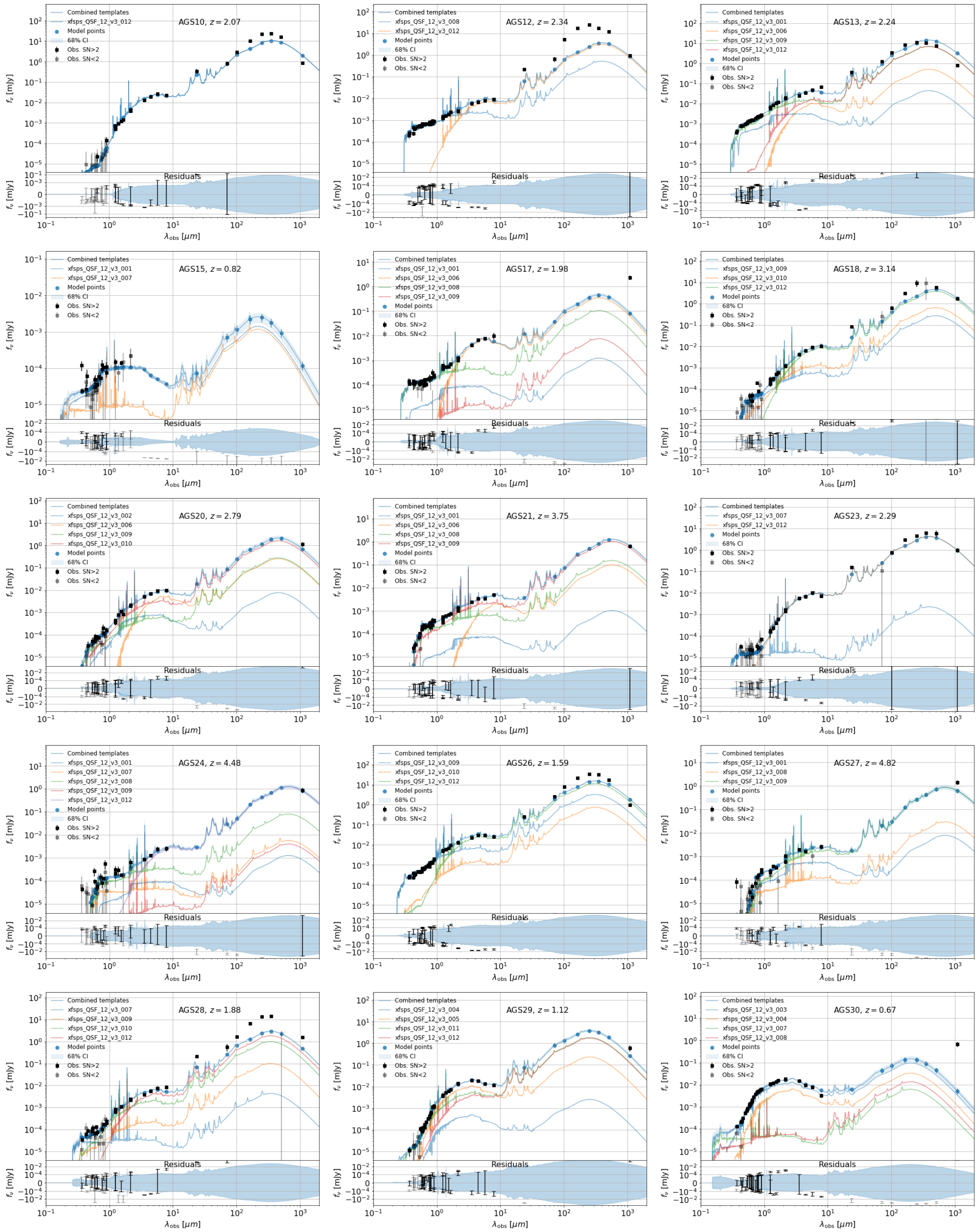
AGS10, z = 2.07
AGS12, z = 2.34
AGS13, z = 2.24
AGS15, z = 0.82
AGS17, z = 1.98
AGS18, z = 3.14
AGS20, z = 2.79
AGS21, z = 3.75
AGS23, z = 2.29
AGS24, z = 4.48
AGS26, z = 1.59
AGS27, z = 4.82
AGS28, z = 1.88
AGS29, z = 1.12
AGS30, z = 0.67
Combined templates
Model points
68% CI
Obs. SN>2
Obs. SN<2
Residuals
fν [mJy]
λobs [μm]

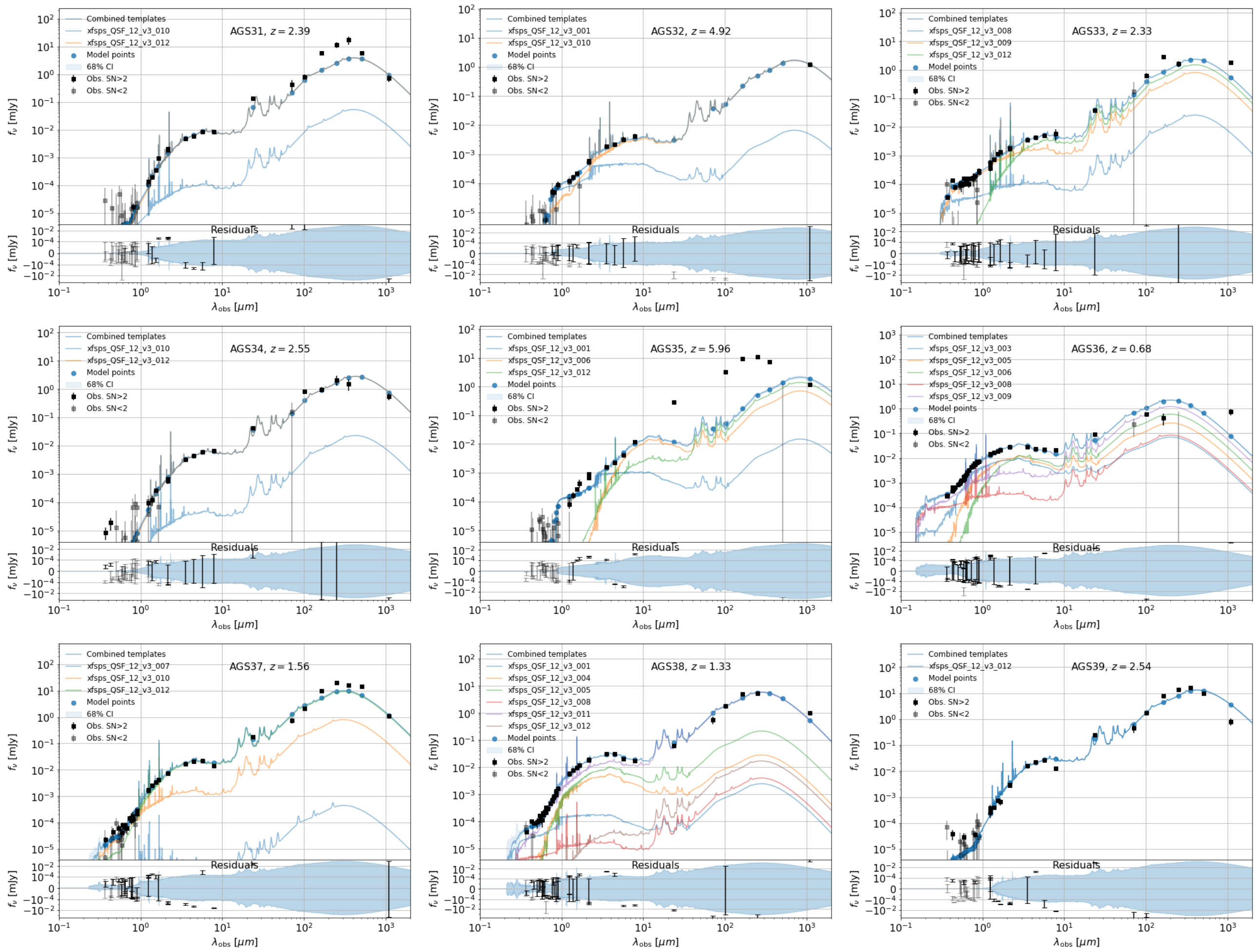

FIGURE A.1: SEDs fit with the XFSPS-12O template set including Super-deblended and 1.1mm ALMA infrared data.

A.2 XFSPS-12M

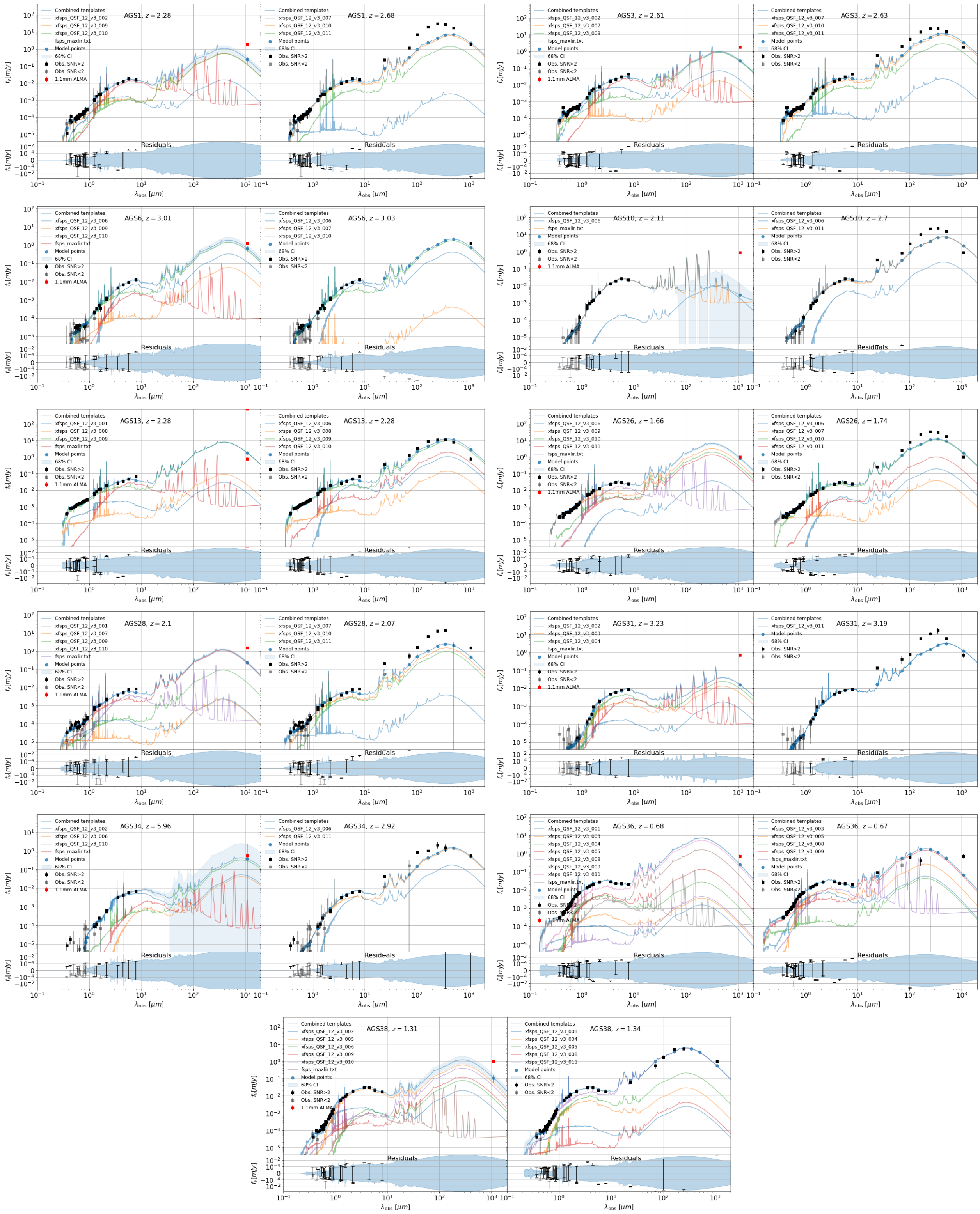

FIGURE A.2: SEDs fit with the XFSPS-12M template set including Super-deblended and 1.1mm ALMA infrared data. Only fits using template #12 replacement are shown.

A.3 Extrapolation and truncation schemes

The first method adopted for the truncation of the IR templates was a simple truncation directly to 0 below $1\mu m$ and to $9.1nm$ (Figure A.3) which is the starting point of the XFSPS-12O. The fits with this new set with IR templates truncated to 0, dubbed the XFSPS-1210Z, is shown on the right plot of Figure A.4a, and it is clearly evident that the fitting using this truncation to zero eliminated the extrapolation error at shorter wavelengths and improved the fit in the FIR by closing the gap between observations and fit.

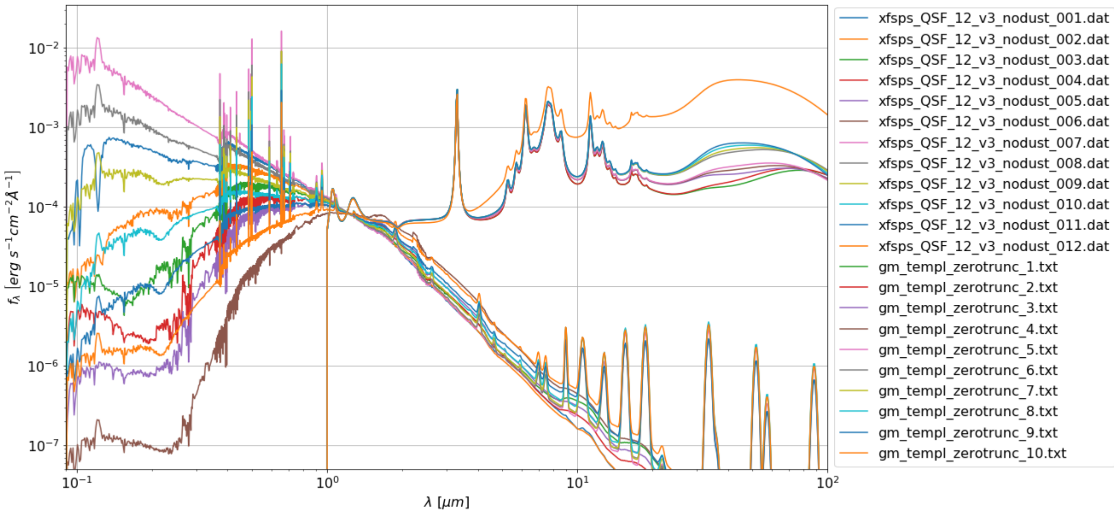

FIGURE A.3: XFSPS-1210Z templates the Magdis et al. 2012 [88] templates extrapolated to wavelengths below $1\mu m$ by direct truncation to zero.

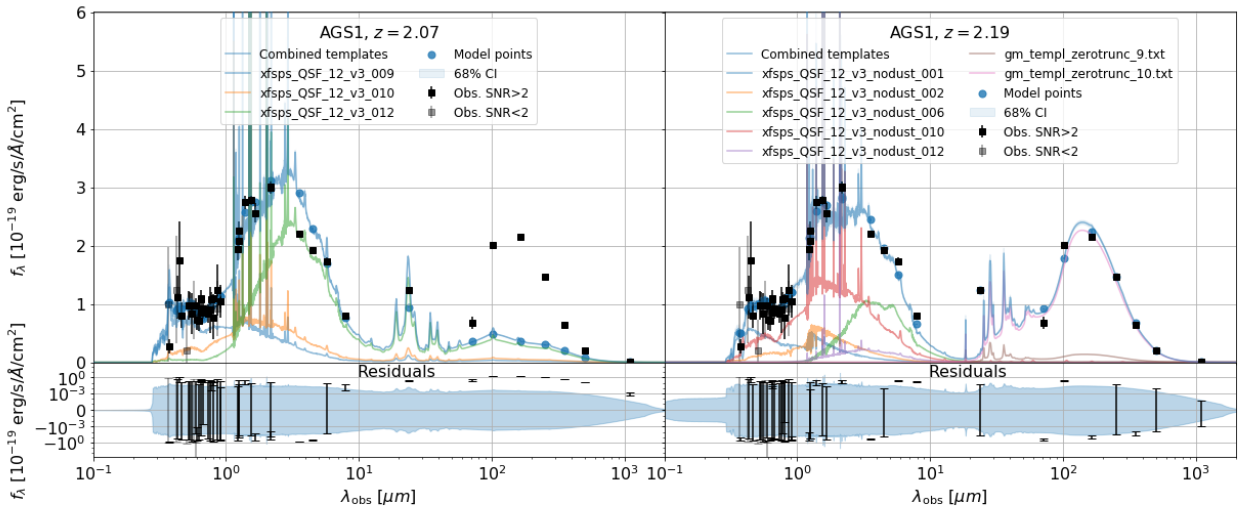

(A) SED fits including IR data with *(Left)* the XFSPS-12O template set and *(Right)* the XFSPS-1210Z template set

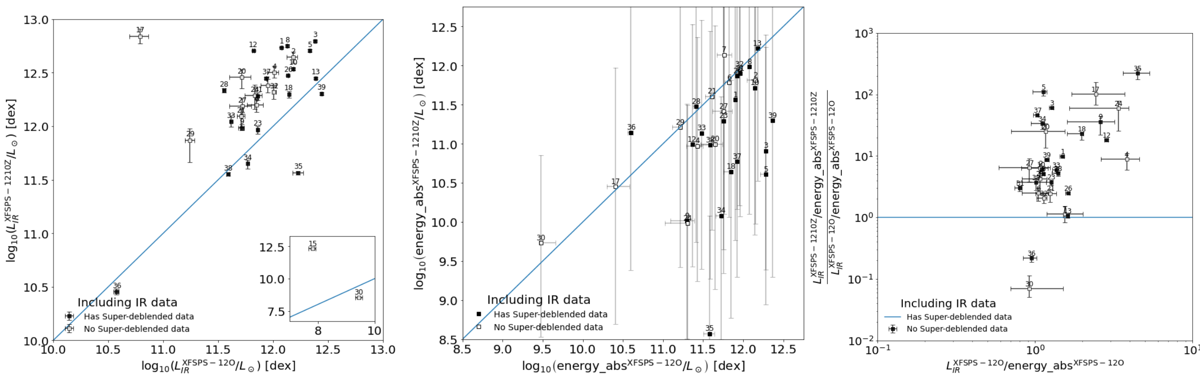

(B) (C) (D)

FIGURE A.4

An important quantity of interest is the infrared luminosity. For the SED fits the infrared luminosity was determined by first determining the rest frame luminosity, Equation 2.10, and then integrating the rest frame luminosity from $8\mu m$ to $1000\mu m$, as in Equation 2.11. Along with energy absorbed these two quantities should ideally be close to equal or within a small factor, as the output infrared luminosity should be closely related to the stellar radiation absorbed in the optical. The right plot of Figure A.4 illustrates this close relationship when fitting with the XFSPS-12O set as the infrared luminosity to energy absorbed values range from $L_{IR}^{XFSPS-12O}/energy\_abs_{XFSPS-12O} \sim 1-4$. However, when fitting with the XFSPS-1210Z the $L_{IR}^{XFSPS-1210Z}/energy\_abs_{XFSPS1210Z}$ becomes larger than the XFSPS-12O values, $L_{IR}^{XFSPS-12O}/energy\_abs_{XFSPS-12O}$, by up to 3 orders of magnitude. The left Figure A.4 tells us that this is partly due to the increase in $L_{XFSPS-1210Z}$, which is expected when we close the gap between data and model compared to fits with XFSPS-12O. But the increase in $L_{XFSPS-1210Z}$ is not close to the factor of e.g. 3-4 we would expect from the left fit to the right fit of Figure A.4a. Thus to explain an increase in $L_{XFSPS-1210Z}/energy\_abs_{XFSPS-1210Z}$ the energy absorbed must decrease. This is surely unexpected as the energy absorbed is dominated by stellar light absorbed in the UV-optical where EAZY should be using the same XFSPS-12O templates, when fitting with XFSPS-1210Z.

When adding the IR templates to the template set, what might lower the energy absorbed and cause this discrepancy between infrared luminosity and energy absorbed? To answer this question we redo the fits without the infrared Spitzer, Herschel and ALMA data constraints. By doing so we expect EAZY to use the same templates for the XFSPS-1210Z and XFSPS-12O template fits as only the optical region has data to be fit, and the additional IR templates are truncated to 0 at short wavelengths.

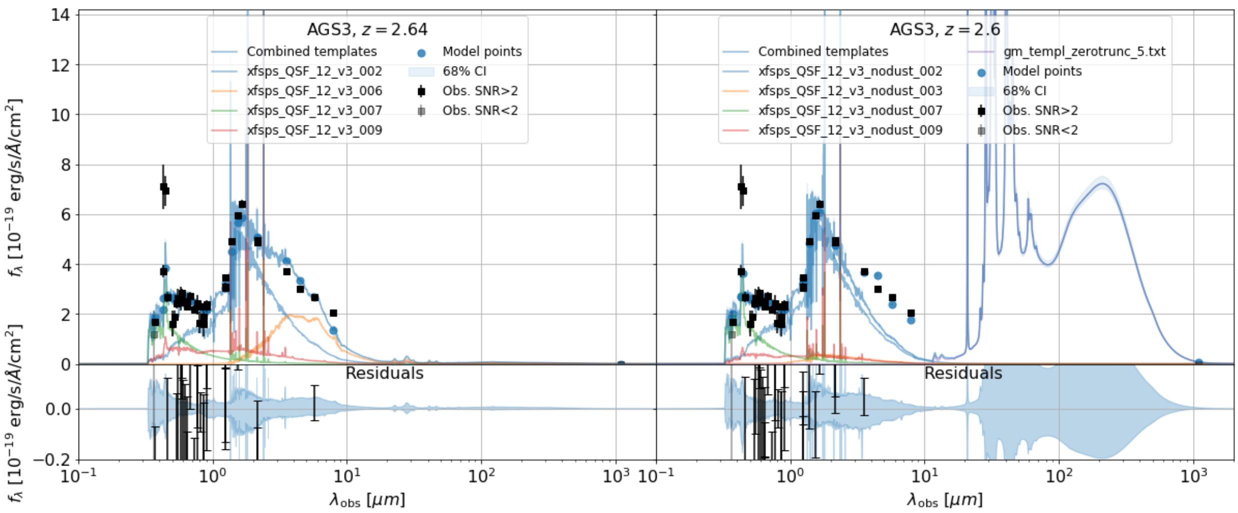

FIGURE A.5: Fits excluding far infrared data. *(Left)* SED fit using the XFSPS-12O. *(Right)* SED fit using the XFSPS-1210Z.

When excluding the infrared data we see that the fits with XFSPS-1210Z and XFSPS-12O pick more or less the same FSPS templates to fit the optical data. But two additional issues appear - 1) the truncated IR templates are still used, and 2) there is now a distinct deviation in the IRAC bands between observations and fit (Figure A.5).

The solution to this issue is not immediately obvious, but as with the XFSPS-1210R we presume that the problem might originate from a coding extrapolation error, presumably due to the drastic extrapolation to shorter wavelengths by directly truncating the IR templates to zero. The first attempt at solving this deviation from the observations was tried by employing a different method for extrapolating and truncating the IR templates. Figure A.6a shows the first attempt at truncating the templates using a polynomial extension to the 9.1nm starting point of the FSPS templates. The polynomial truncation of this XFSPS-1210P template set corrects the IRAC band deviation significantly as shown on the right of Figure A.6b compared to the direct truncation to 0 on the left of Figure A.5.

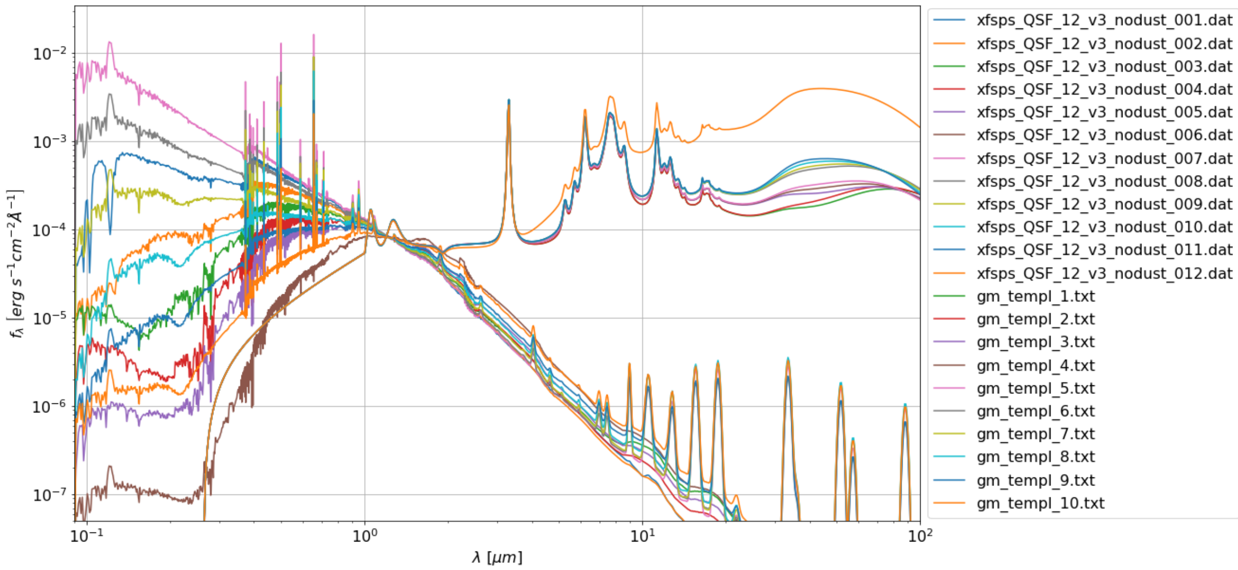

(A) XFSPS-1210P set with the Magdis et al. 2012 [88] templates extrapolated to wavelengths below $1\mu m$ using a polynomial.

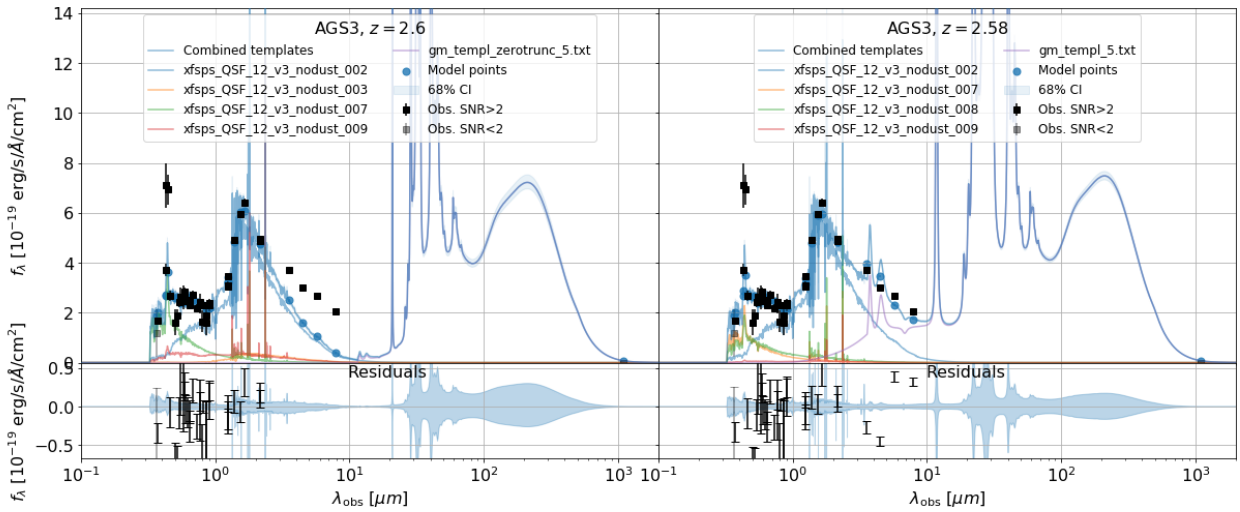

(B) SED fits excluding IR data (*Left*) with the XFSPS-1210Z set with infrared templates truncated to zero and (*Right*) the XFSPS-1210P set with infrared templates extrapolated to shorter wavelengths using a polynomial.

FIGURE A.6

Even though the XFSPS-1210P corrects the IRAC band deviation to some extent, one might worry that the sudden change to a polynomial drop off below $1\mu m$ might still cause problems. To tackle this problem an attempt was made to smoothen the IR templates by starting the extrapolation earlier, such that they would drop off rapidly below $\sim 3\mu m$. Instead of polynomially truncating the templates below $1\mu m$, Gabriel Brammer smoothened and extrapolated the 10 IR templates to shorter wavelengths by attaching the PAH component from the Compiègne et al. 2011 [93] dust model, which drop off rapidly at short wavelengths. Additionally the infrared bump of the IR templates was fit by a range of modified blackbodies.

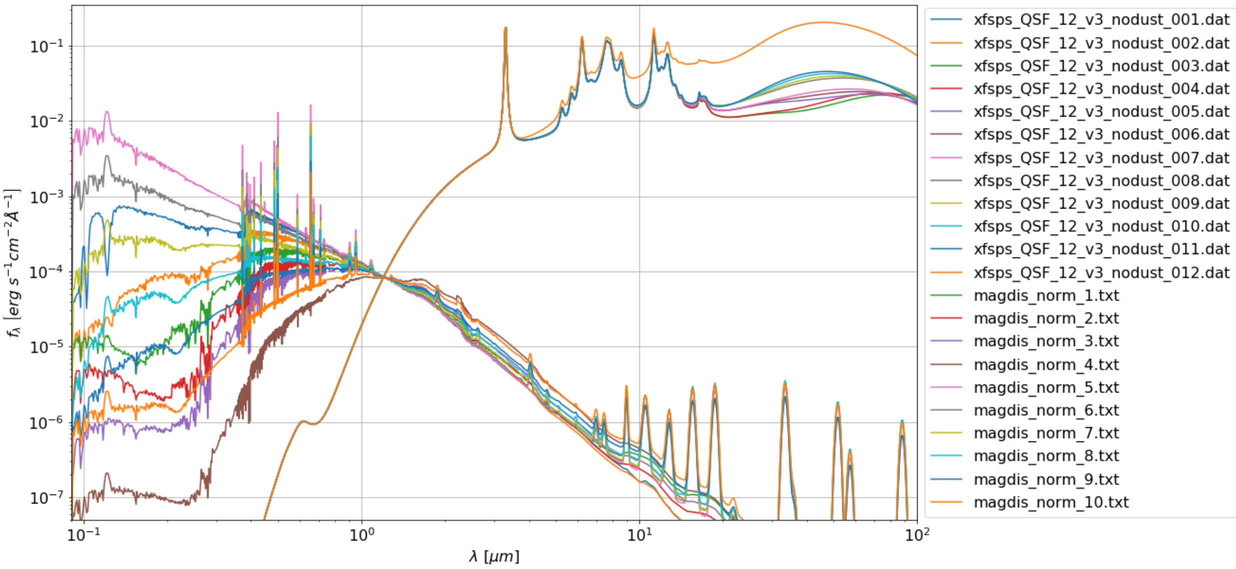

(A) XFSPS-1210PAH templates

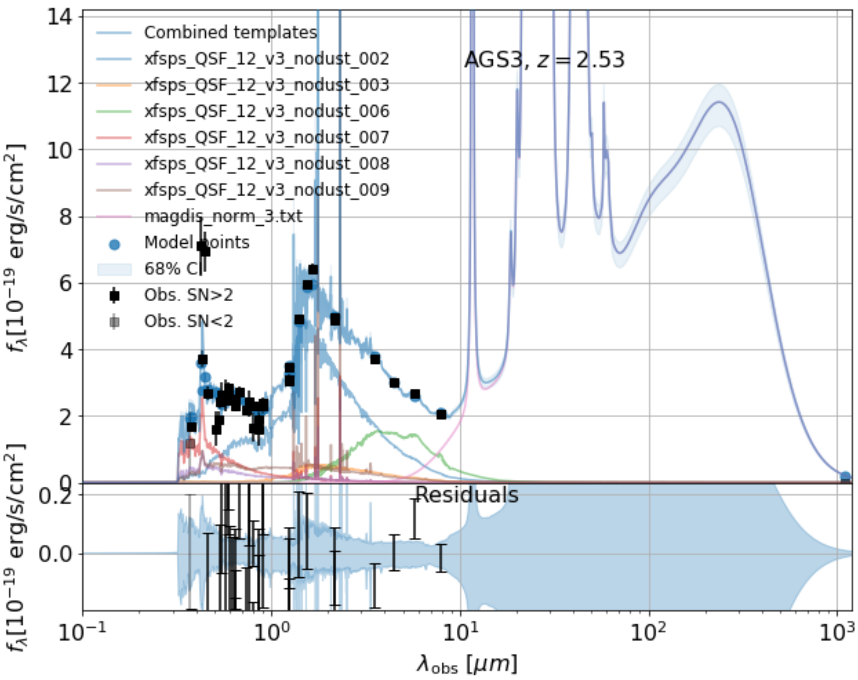

(B) SED fit with the XFSPS-1210PAH excluding IR data

FIGURE A.7

These XFSPS-1210PAH IR templates (Figure A.7a) drop off more rapidly and provide a better fit in the IRAC bands (Figure A.7b) where IRAC measurements now fall within the 68% confidence interval, as opposed to previous truncation attempts of the IR templates.

A.4 XFSPS-1210R

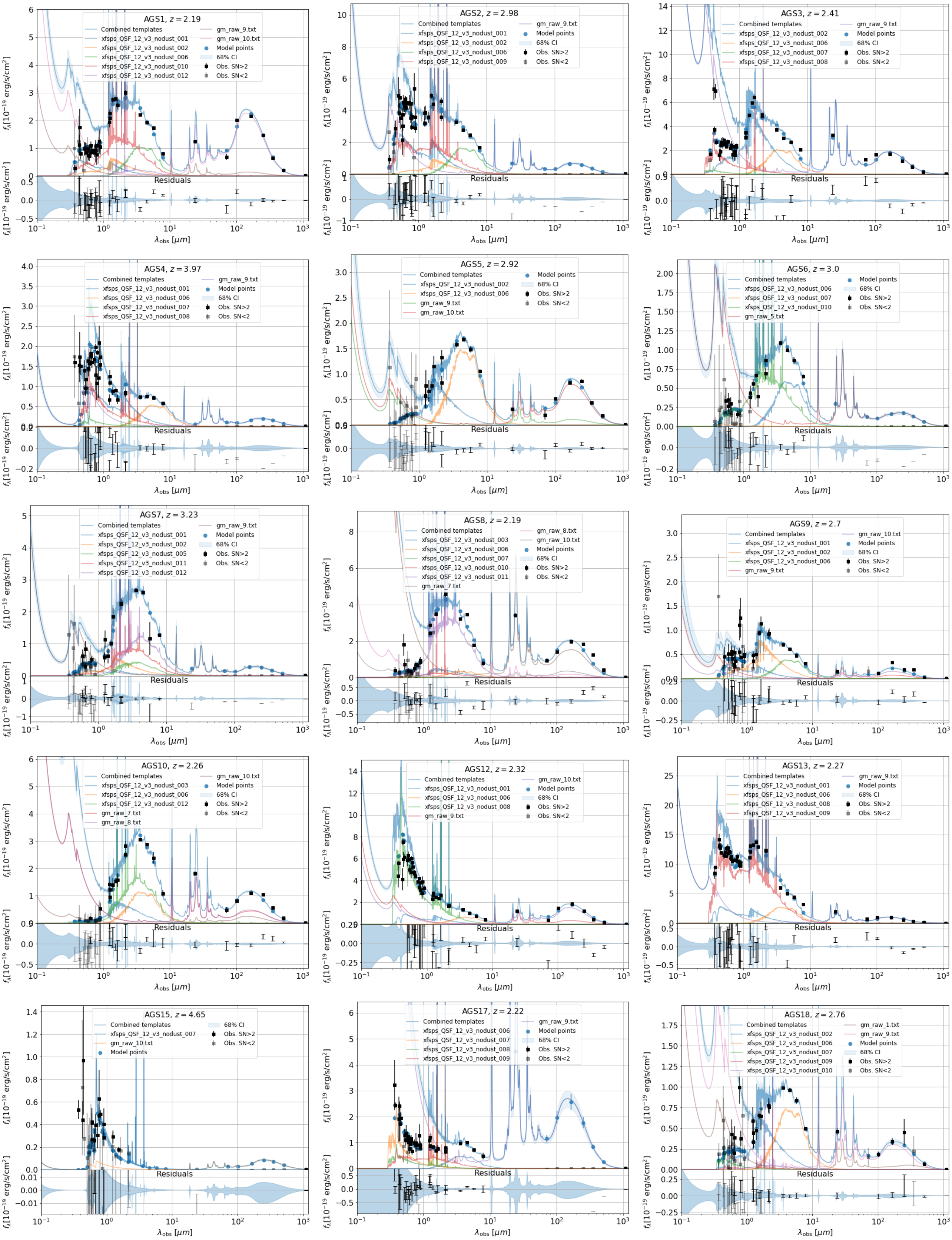

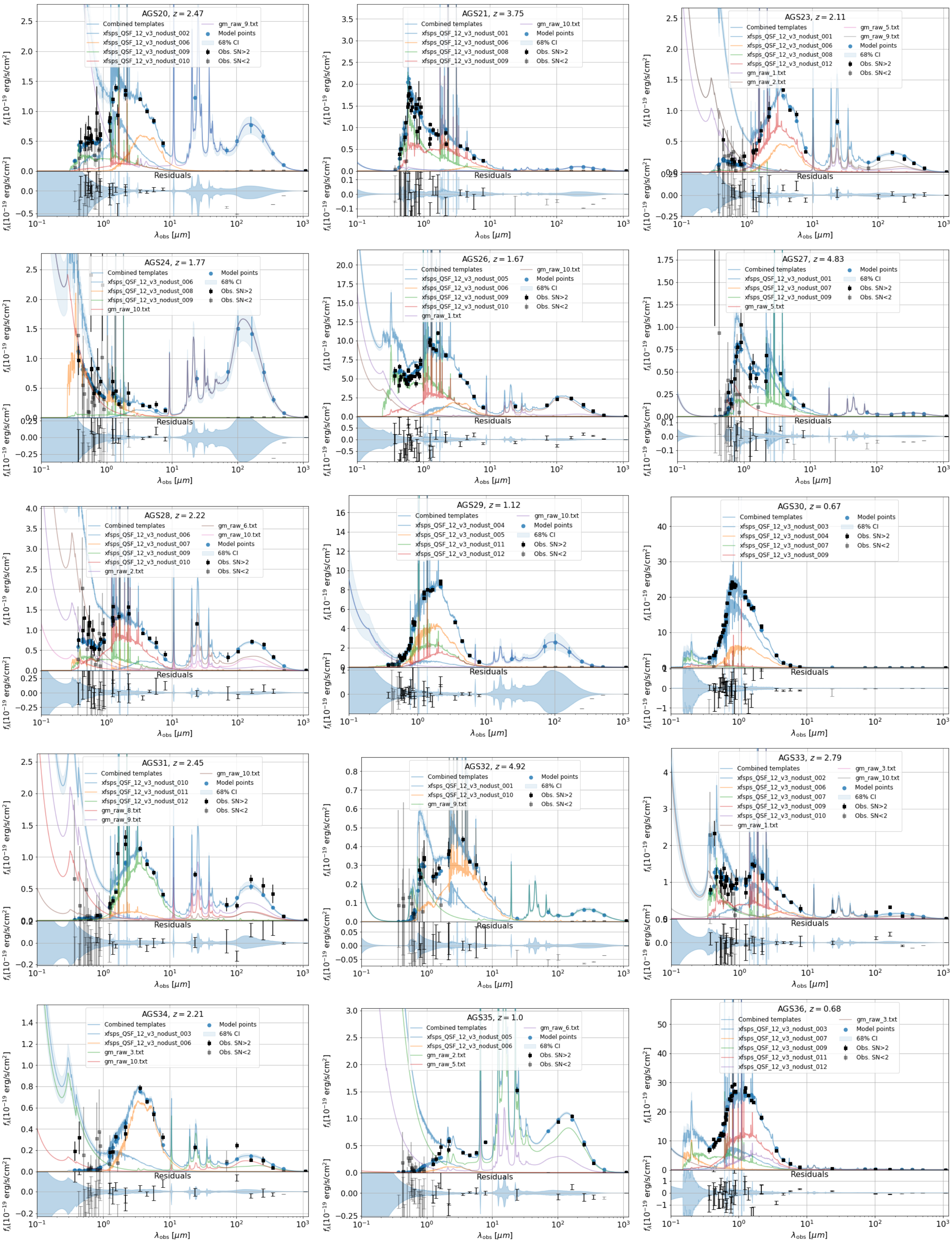
AGS20, $z = 2.47$
AGS21, $z = 3.75$
AGS23, $z = 2.11$
AGS24, $z = 1.77$
AGS26, $z = 1.67$
AGS27, $z = 4.83$
AGS28, $z = 2.22$
AGS29, $z = 1.12$
AGS30, $z = 0.67$
AGS31, $z = 2.45$
AGS32, $z = 4.92$
AGS33, $z = 2.79$
AGS34, $z = 2.21$
AGS35, $z = 1.0$
AGS36, $z = 0.68$

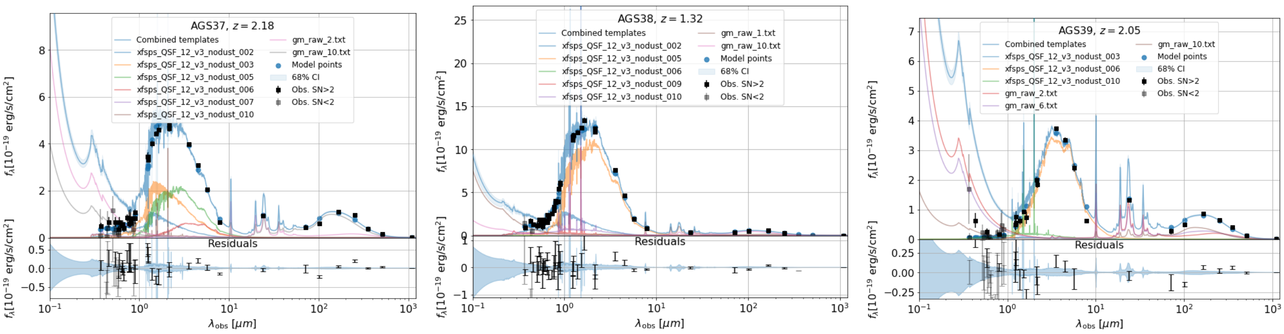

FIGURE A.8: SEDs fit with the XFSPS-1210R template set including Super-deblended and 1.1mm ALMA infrared data.

Appendix B

Predicting the 1.1mm Universe

When changing the EAZY upper redshift grid limit from $z_{\mathrm{upper}} = 6$ to $z_{\mathrm{upper}} = 12$, the redshifts of the AGS DSFGs remain mostly the same, with the exception of two sources: AGS34 and AGS35.

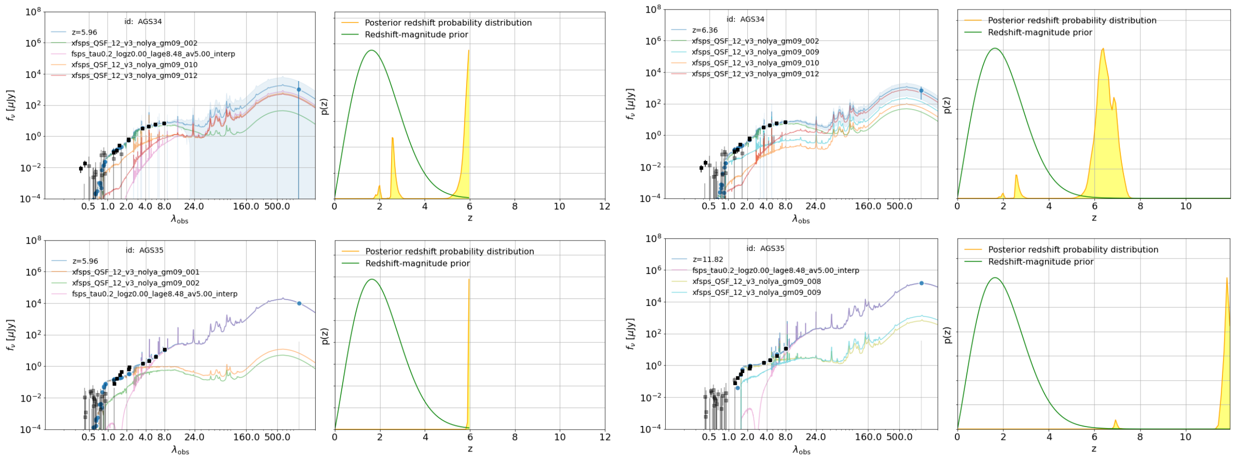

FIGURE B.1: (*Left*) EAZY SED fits of AGS34 and AGS35 with a redshift grid limit of $z_{\mathrm{upper}} = 6$ compared to (*Right*) with a redshift grid limit of $z_{\mathrm{upper}} = 12$

These two sources are sent to artifically high redshifts, as the EAZY code seems extend the posterior redshift probability distribution to even higher redshifts.

ID	None	SNR3	SNR3&N10	SNR3&Z20	SNR3&N10&Z20	$\frac{f_{1.1mm}}{\sigma_{1.1mm}}$	$\frac{f_{1.1mm}}{\sigma_{\rm RMS}}$
AGS1	✓	✓	✓	✓	✓	17.08	9.90
AGS2	✓	✓	✓	✓	✓	37.92	32.63
AGS3	✓	✓	✓	✓	✓	64.20	25.53
AGS4	✓	✓	✓	✓	✓	17.24	28.67
AGS5	✓	✓	✓	✓	✓	12.57	87.15
AGS6	✓	✓	✓	✓	✓	18.67	12.13
AGS7	✓	✗	✗	✗	✗	2.85	18.90
AGS8	✓	✓	✓	✓	✓	21.69	4.02
AGS9	✓	✓	✓	✓	✓	8.18	5.15
AGS10	✓	✓	✓	✓	✓	19.88	8.29
AGS12	✓	✓	✓	✓	✓	11.16	6.39
AGS13	✓	✓	✓	✓	✓	48.48	29.61
AGS15	✓	✓	✓	✓	✓	21.69	0.00
AGS17	✓	✓	✓	✓	✓	45.53	2.82
AGS18	✓	✓	✓	✗	✗	18.26	3.29
AGS20	✓	✓	✓	✓	✓	13.63	6.31
AGS21	✓	✓	✓	✓	✓	4.65	6.96
AGS23	✓	✓	✓	✓	✓	8.43	4.21
AGS24	✓	✓	✓	✗	✗	14.45	0.63
AGS26	✓	✓	✓	✓	✓	18.64	5.87
AGS27	✓	✗	✗	✗	✗	0.15	0.37
AGS28	✓	✓	✓	✓	✓	12.70	3.62
AGS29	✓	✓	✓	✓	✓	6.05	0.83
AGS30	✓	✓	✓	✓	✓	3.19	0.02
AGS31	✓	✓	✓	✓	✓	3.26	2.71
AGS32	✓	✗	✗	✗	✗	2.80	12.86
AGS33	✓	✗	✗	✗	✗	2.81	3.64
AGS34	✓	✗	✗	✗	✗	1.10	8.20
AGS35	✓	✓	✓	✓	✓	12.64	1830.29
AGS36	✓	✓	✓	✓	✓	17.52	0.82
AGS37	✓	✓	✓	✓	✓	3.84	2.20
AGS38	✓	✓	✓	✓	✓	5.19	0.61
AGS39	✓	✓	✓	✓	✓	66.34	1.23
#Clipped	0	5	5	7	7		

TABLE B.1: Clipped sources for the synthetic map without IR

ID	None	SNR3	SNR3&N10	SNR3&Z20	SNR3&N10&Z20	$\frac{f_{1.1mm}}{\sigma_{1.1mm}}$	$\frac{f_{1.1mm}}{\sigma_{\mathrm{RMS}}}$
AGS1	✓	✓	✓	✓	✓	100.37	13.74
AGS2	✓	✓	✓	✓	✓	44.13	32.63
AGS3	✓	✓	✓	✓	✓	87.79	30.67
AGS4	✓	✓	✓	✓	✓	23.72	28.67
AGS5	✓	✓	✓	✓	✓	70.55	36.30
AGS6	✓	✓	✓	✓	✓	20.52	12.13
AGS7	✓	✗	✗	✗	✗	2.58	18.90
AGS8	✓	✓	✓	✓	✓	64.82	11.43
AGS9	✓	✓	✓	✓	✓	14.39	4.97
AGS10	✓	✓	✓	✓	✓	54.55	23.48
AGS12	✓	✓	✓	✓	✓	64.61	8.35
AGS13	✓	✓	✓	✓	✓	71.11	16.04
AGS15	✓	✓	✓	✓	✓	21.78	0.00
AGS17	✓	✓	✓	✓	✓	54.66	2.82
AGS18	✓	✓	✓	✓	✓	21.94	7.25
AGS20	✓	✓	✓	✓	✓	14.86	6.31
AGS21	✓	✓	✓	✓	✓	4.49	6.96
AGS23	✓	✓	✓	✓	✓	30.97	3.94
AGS24	✓	✓	✓	✗	✗	15.03	0.63
AGS26	✓	✓	✓	✓	✓	97.03	8.18
AGS27	✓	✗	✗	✗	✗	0.15	0.37
AGS28	✓	✓	✓	✓	✓	37.56	5.87
AGS29	✓	✓	✓	✓	✓	5.70	0.83
AGS30	✓	✓	✓	✓	✓	3.85	0.02
AGS31	✓	✓	✓	✓	✓	20.65	4.52
AGS32	✓	✗	✗	✗	✗	2.65	12.86
AGS33	✓	✓	✓	✓	✓	10.87	3.77
AGS34	✓	✓	✓	✓	✓	13.10	3.69
AGS35	✓	✓	✓	✓	✓	35.50	1017.99
AGS36	✓	✓	✓	✓	✓	23.81	0.21
AGS37	✓	✓	✓	✓	✓	59.84	9.23
AGS38	✓	✓	✓	✓	✓	30.64	1.56
AGS39	✓	✓	✓	✓	✓	51.38	19.40
#Clipped	0	3	3	4	4		

TABLE B.2: Clipped sources for the synthetic map including IR. Colored rows do not have FIR Super-deblended data.